Growth and Characterization of the Quasi-Binary Ga_2Te_3-Ga_2Se_3 Semiconductor Alloy

by

Najeb Mohammed Abdul-Jabbar

A dissertation submitted in partial satisfaction of the
requirements for the degree of
Doctor of Philosophy

in

Engineering - Nuclear Engineering

in the

Graduate Division

of the

University of California, Berkeley

Committee in charge:

Professor Brian Wirth, Co-chair
Professor Edward Morse, Co-chair
Professor Eric Norman
Professor Ronald Gronsky

Spring 2014

Growth and Characterization of the Quasi-Binary Ga_2Te_3-Ga_2Se_3 Semiconductor Alloy

Abstract

Growth and Characterization of the Quasi-Binary Ga_2Te_3-Ga_2Se_3 Semiconductor Alloy

by

Najeb Mohammed Abdul-Jabbar

Doctor of Philosophy in Engineering - Nuclear Engineering

University of California, Berkeley

Professor Brian Wirth, Co-chair

Professor Edward Morse, Co-chair

This dissertation presents an experimental investigation on the growth and characterization of the quasi-binary Ga_2Te_3-Ga_2Se_3 semiconductor alloy. Single crystal $Ga_2(Se_{1-x}Te_x)_3$ specimens were grown via modified Bridgman methods for $x = 0.60$, 0.67, 0.8, 0.9, and 1.0. Preliminary structural characterization via powder x-ray diffraction showed a cubic zincblende structure. Satellite reflections discovered in the powder diffraction patterns alluded to the presence of secondary superstructures. High-resolution x-ray diffraction and x-ray absorption experiments conducted at the Advanced Photon Source, the Stanford Synchrotron Radiation Lightsource, and the Advanced Light Source confirmed the presence of ordered mesoscopic two-dimensional vacancy structures that can influence the pressure-induced amorphization behavior of Ga_2SeTe_2. More specifically, vacancy ordered and semi-ordered Ga_2SeTe_2 specimens amorphized at around 10-11 GPa as opposed to vacancy disordered specimens, which amorphized at around 8-9 GPa. X-ray absorption fine structure experiments indicated these vacancy based superstructures locally distort the lattice. However, the symmetry associated the face-centered cubic Bravais lattice is preserved. Local atomic distortions were directly observed via aberration-corrected scanning transmission electron microscopy conducted at the National Center for Electron Microscopy, where an inversion in the cation-anion orientation vector across the boundaries of the two-dimensional vacancy structures was observed. The effect of vacancy ordering on the physical properties of $Ga_2(Se_{1-x}Te_x)_3$ was also studied. Positron annihilation spectroscopy revealed that positron lifetimes in Ga_2SeTe_2 are similar to that of large open-volume defects. As vacancies order, their role in positron trapping diminishes. Band gap measurements via optical absorption demonstrated that vacancy ordering in Ga_2SeTe_2 drives down band gap energy by approximately 0.05 eV. This observation was accompanied by Hall effect experiments, where the resistivity of vacancy ordered samples decreased by two orders of magnitude with moderate gains in charge carrier mobility.

To my family.

Contents

List of Figures

List of Tables

Acknowledgments

I would first like to acknowledge my family for their support during my graduate studies at Berkeley. I would specifically like to express gratitude to my mother. Her unwavering commitment to her children's education is a constant source of inspiration for me.

I want thank my advisor, Brian Wirth, for his dedication to my research topic and his support throughout my years as a graduate student. This dissertation would not have been possible without his guidance. I would also like to thank Edith Bourret-Courchesne at Lawrence Berkeley National Laboratory for allowing me access to her crystal growth facility. All of the experimental work I carried out would not have been possible without her support. I would also like to thank Ronald Gronsky for the fruitful discussions we had pertaining to my research. Taking his classes on materials characterization motivated my interest to incorporate advanced diffraction methods and electron microscopy into my research.

Finally, I would like to acknowledge all of my colleagues during my time in graduate school. At Berkeley, I would like to thank Tom Forrest, who taught me a great deal on conducting experiments at synchrotrons; a sizable portion of the data presented in this dissertation were collected with his help. Patrick Valdivia, for useful discussions related and unrelated to research, and Karen Bustillo for her assistance during optical absorption measurements. At the Advanced Light Source, I would like to acknowledge Bora Kalkan and Alastair MacDowell for their help in setting up high-pressure and high-temperature diffraction experiments. At the National Center for Electron Microscopy, I would like to thank Peter Ercius, Markus Boese, and Marissa Libbee for their help in getting me acquainted with all of the electron microscopes available there. At Lawrence Berkeley National Laboratory, I would like to thank Chris Ramsey for his tremendous assistance in the design and construction of all of my experiments. His passion for engineering was truly inspiring and I will miss him dearly. I also thank Gautam Gundiah, Eric Samulon, Zewu Yan, Seng Choong, Martín Gascón, Ivan Khodyuk, and Gregory Bizarri for all of the enlightening and often lively discussions at the lab.

Chapter 1

Introduction

1.1 Basic Semiconductor Physics

As its name implies, a semiconductor is material whose electrical conductivity is between that of a conductor (e.g. metals) and that of an insulator (e.g. glass). Unlike metals and insulators, which have been known since antiquity, engineering of semiconducting materials became prevalent early in the twentieth century. Indeed, a crucial turning point in modern semiconductor materials science was the invention of the transistor by John Bardeen, Walter Brattain, and William Shockley in the late 1940s. After this milestone, the development of semiconductors grew at a rapid pace and lead to cheaper and more compact circuitry, which served as a harbinger to the modern industries including microelectronics, light emitting diodes (LEDs), and solar cells. For this reason, semiconductor processing has become an immensely exact endeavor. Processing techniques like crystal pulling, zone-refining, and epitaxy have allowed for the preparation of silicon and germanium with impurity levels on the order of 10^{10} cm^{-3}.[1] Consequently, defect and impurity characterization in semiconductors has led to the use of sophisticated probes that include powerful electron microscopes, particle accelerators, and radiation sources. With that, the interplay of processing and characterization becomes the backbone of future advances in semiconductor technology.

1.1.1 Electronic Structure

The classification of metals, insulator, and semiconductors arises out of the band theory of solids.[1–4] From a theoretical standpoint, the free electron model allows for adequate insight into the physical properties of metals. Not surprisingly, the model fails for semiconductors and insulators as electrons in these materials are not free to roam and hence these materials have low conductivity. A model describing an insulator is easy to comprehend if one images an electrons in an insulating material tightly bound to its lattice. A difficulty arises when trying to describe semiconductors, which have intermediate electrical conductivity. To circumvent this obstacle, one can construct a simple model based on a nearly free electron. First, consider a free electron gas in one dimension. It is associated with an electron mass m that is confined to a length L bounded by infinite barriers. The wavefunction that represent the electron, $\psi_n(x)$, is a solution of the time independent Schrödinger equation $\mathcal{H}\psi{=}E\psi$. By neglecting potential energy, the hamiltonian $\mathcal{H}$, becomes $p^2/2m$, where p is electron momentum. In quantum mechanics, momentum is represented by the operator $\imath\ \hbar d/dx$, so that

$$\mathcal{H}\psi_n = -\frac{\hbar^2}{2m}\frac{d^2\psi_n}{dx^2} = E_n\psi_n \tag{1.1}$$

where E_n is the energy of the electron in an energy level, or orbital. If the system is projected to three dimensions, where the electrons are confined to a cube with edge L, the free electron Schrödinger equation becomes

$$-\frac{\hbar^2}{2m}\left(\frac{\partial^2}{\partial x^2}+\frac{\partial^2}{\partial y^2}+\frac{\partial^2}{\partial z^2}\right)\psi_{\mathbf{k}}(\mathbf{r})=E_{\mathbf{k}}\psi_{\mathbf{k}}(\mathbf{r}). \tag{1.2}$$

The wavefunction of the electron confined in the cube is a standing wave, which can be written as

$$\psi_n(\mathbf{r})=A\sin(\pi n_x x/L)\sin(\pi n_y y/L)\sin(\pi n_z z/L). \tag{1.3}$$

Periodic boundary condition are imposed to further simplify the model, and the wave functions that satisfy the free electron Schrödinger equation become traveling plane waves

$$\psi_{\mathbf{k}}(\mathbf{r})=\exp(\imath\mathbf{k}\cdot\mathbf{r}) \tag{1.4}$$

which carry momentum $\mathbf{p}=\hbar\mathbf{k}$. The components of the wavevector $\mathbf{k}$ are then given by

$$k_x,k_y,k_z=0;\pm\frac{2\pi}{L};\pm\frac{4\pi}{L};\text{etc.} \tag{1.5}$$

Substituting equation 1.4 into equation 1.2 gives the energy, $E_{\mathbf{k}}$ of the orbital associated with wavevector $\mathbf{k}$ can then be written as

$$E_{\mathbf{k}}=-\frac{\hbar^2}{2m}(k_x^2+k_y^2+k_z^2). \tag{1.6}$$

Figure 1a qualitatively shows the distribution of electron energy E as a function of wavevector $\mathbf{k}$.

The free electron model can be extrapolated to a crystal system where electrons are weakly perturbed by the periodic potential of the atom cores. In a manner analogous to x-ray diffraction in crystals, electron waves diffract in lattice giving rise to energy gaps. The origin of the energy gaps can be explained by taking a one dimensional crystal of lattice constant a. By applying the Bragg conditions for crystal diffraction, $(\mathbf{k}+\mathbf{G})^2=k^2$, for the one dimensional lattice one can write the wavevector as

$$k=\pm\frac{G}{2}=\pm\frac{n\pi}{a}, \tag{1.7}$$

where $G=2\pi n/a$ (also known as the reciprocal lattice vector) and n is an integer. If only first-order diffracted waves are accounted for, an energy gap at $k=\pm\pi/a$ is obtained. This is qualitatively shown in Figure 2b. The magnitude of the energy gaps are the key deciding factor in determining whether a material is a semiconductor or an insulator. Moreover, based on the crystal system the gap between energy bands can be direct or indirect. The momentum of electrons in the energy gaps are the same in a direct band gap and differ in an indirect band gap. This difference has a crucial influence on semiconductor properties with the most important being charge transport and optical absorption.

The simple energy band model presented here serves to illustrate the origin of energy bands in materials. Systems that model actual materials are drastically more complex.

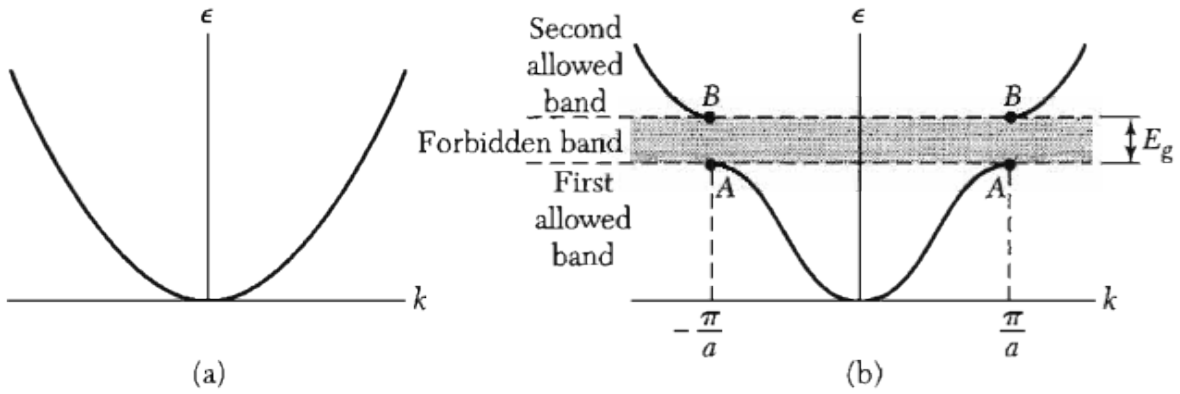

Figure 1.1: (a) Energy E versus wavevector k of a free electron. (b) Energy E versus wavevector k of one dimensional monoatomic lattice, where electrons are weakly perturbed by a periodic potential that gives rise to energy gaps at discrete k values as reproduced from Kittel.[3]

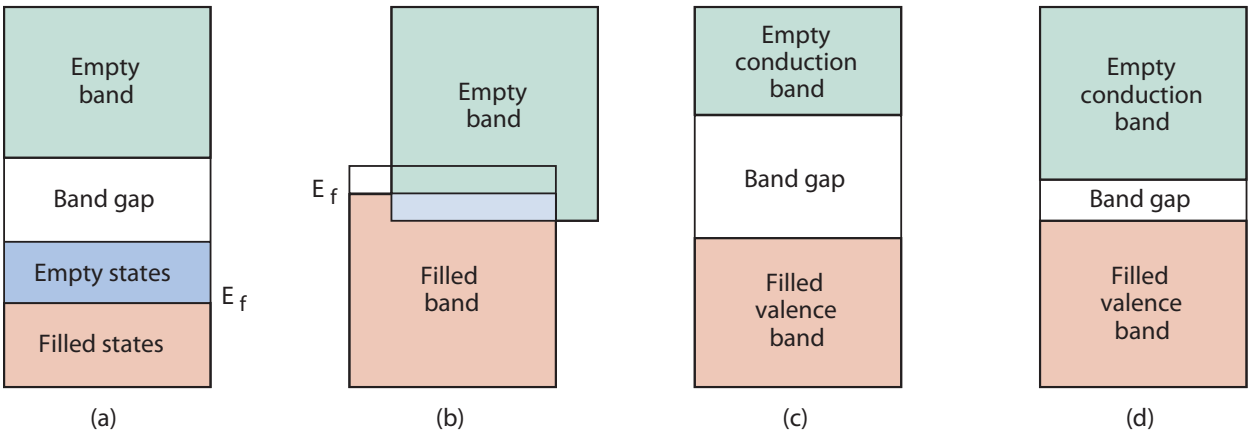

Figure 1.2: General band structure of (a) metals, (b) semimetals, (c) insulators, and (d) semiconductors as reproduced from Callister.[5]

Nevertheless, the concept of solving the Schrödinger equations for a given crystal system to determine its energy band structure remains the same. Indeed, an entire field in condensed matter physics is devoted to such problems, with density functional theory (DFT) being the canonical example.[6] What band theory achieves, is an elegant representation of the electronic structure of metals, insulators, and semiconductors. In its most basic form and assuming no temperature effects (i.e. 0 K), it consists of a valence band (energy band completely filled with electrons) and a conduction band (energy band with no electrons) with an energy gap separating them. This is illustrated in Figure 1.2: where (a) represents the band structure found in metals such as copper, with available electron states adjacent to filled states, (b) represents the structure of semimetals such as bismuth where there is an overlap between the valence and conduction band, (c) represent the band structure of an insulator where a filled valence band is separated from the conduction band by a large energy gap (generally >2 eV), and (d) represents the band structure of a semiconductor with the filled valence band is separated from the conduction band by a relatively band gap (generally < 2 eV).

1.1.2 Crystal Structure

Most technologically important semiconductor materials exhibit a diamond ($Fd\bar{3}m$ space group) or zincblende ($F\bar{4}3m$ space group) cubic crystal structures as depicted in Figure 1.3. The structures consist of two interpenetrating face centered cubic (FCC) sublattices that are displaced by one quarter of the distance along the diagonal of the cube. In a diamond cubic lattice, the atoms are identical; Si and Ge have this structure. The zincblende lattice has alternating types of atoms at the lattice site; compound semiconductors such as GaAS and CdTe have this structure. Diamond and zincblende structures have tetrahedral coordination. Each atom in the diamond and zincblende structures has four nearest neighbors arranged in a tetrahedral configuration. The atoms are covalently bonded to their neighbors by sharing the ring valence (i.e. outer) electrons.

Other structures exhibited by semiconductor materials include wurtzite (hexagonal), rocksalt (NaCl), and rutile (tetragonal). Table 1.1 shows some of the properties of important semiconductors. Generally, crystal structure plays a key role in determine a semiconductor's physical properties. These can include difficulty of growth, optical characteristics, electrical behavior, and processing characteristics. Hence, in carry out research on any semiconductor system, one must always have a firm understanding of the crystal structure.

1.1.3 Charge Carriers

Consider a semiconductor crystal in an environment with a nonzero temperature. With enough thermal energy, it is possible to excite an electron located in the valence band across the energy gap to the conduction band. This can bee seen as the release of a covalently bonded electron that proceeds to drift throughout the crystal. The excited electron in the conduction band leaves an electron vacancy in the valance band otherwise known as a hole (having an opposite charge). The combination of the two charge carriers is known as an

electron-hole pair (analogous to an ion pair in gases). The probability per unit time that an electron-hole pair is thermally generated can be formulated as,

$$p(T) = CT^{2/3} \exp\left(-\frac{E_g}{2kT}\right), \tag{1.8}$$

where T is the absolute temperature, E_g is the energy of the band gap, k is the Boltzmann constant, and C is a material dependent proportionality constant.[8] One notices that the probability of thermally exciting an electron is highly dependent on the ratio of band gap energy to temperature. As a result, materials with large band gaps (insulators) will have low probabilities from thermal charge carrier generation, which results in their low electrical conductivity. Conversely, in materials with a small band gap energy (semiconductors), thermally generated electron-hole pairs recombine overtime establishing an equilibrium where the concentration of electron-hole pairs at any given time is proportional to the rate of formation.

Electrons in the conduction band and holes in the valence band can move under the influence of an applied electric field. Positively charged holes will move with the electric field, while negatively charged electrons will move in the opposite direction. The charge carrier movement contributes to the conductivity of the material. To gain a better understanding of charge transport parameters in a semiconductor, a simple but effective classical first-principles analysis is presented.[1] Assume an electric potential U is applied between two points in a solid with length L. The electric field created,

$$\mathcal{E} = \frac{U}{L} \tag{1.9}$$

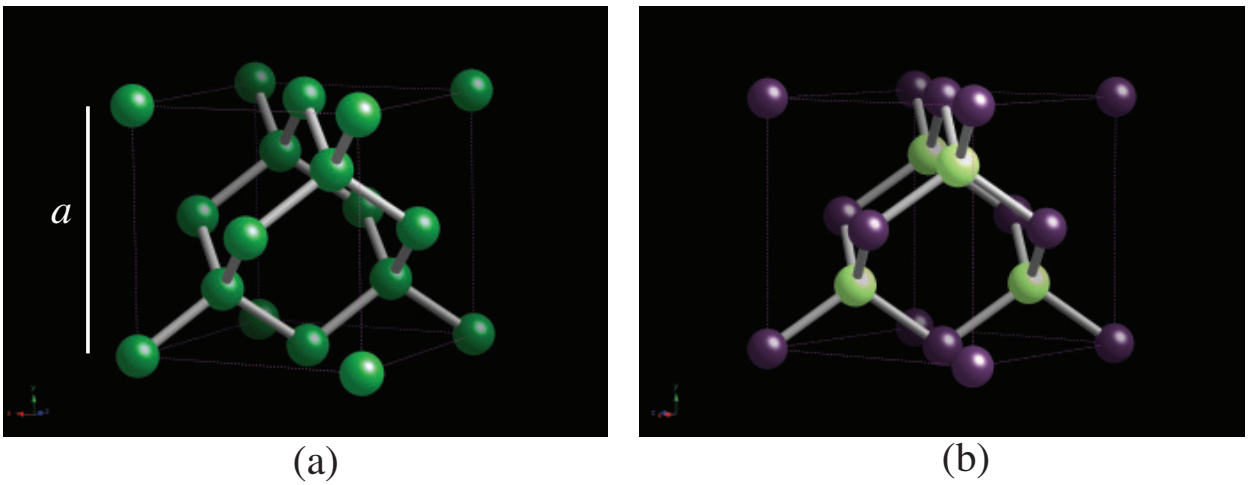

Figure 1.3: Diamond cubic lattice (a) and zincblende cubic lattice (b) with lattice constance a.

is present at all points in the solid, triggering an acceleration

$$a = \frac{e}{m}\mathcal{E}, \tag{1.10}$$

where e is the electron charge and m is the electron mass. As a result, electron will acquire a velocity in the direction of the electric field in addition to their random velocities. It is safe to assume that the direct velocity is completely lost as an electron is significantly lighter than its host atom. Hence, the actual velocity is the one that is picked up between collisions. If an average of the actual times between collisions is known one can write the average velocity as

$$v_{\text{average}} = a\tau, \tag{1.11}$$

where τ is the collision time (also known as the mean free time or relaxation time). Sources that contribute to the collision include the lattice, lattice defects, and elemental impurities. The overall collision time can then be approximate using "Matthiessen's Rule",

$$\frac{1}{\tau} = \frac{1}{\tau_{\text{lattice}}} + \frac{1}{\tau_{\text{defects}}} + \frac{1}{\tau_{\text{impurities}}} + \text{etc.} \tag{1.12}$$

Substituting equation (1.10) into (1.12) yields the electron drift velocity,

$$v_{\text{D}} = \left(\frac{e}{m}\tau\right)\mathcal{E}. \tag{1.13}$$

The quantity in parentheses is known as the mobility, denoted by μ. It follows that the higher the mobility, the more mobile the electrons are in the solid. The analysis is similar for any charge carrier, so one can then write the drift velocity for electrons and holes as

$$v_e = \mu_e\mathcal{E} \tag{1.14}$$

Table 1.1: Properties of Important Semiconductors as reproduced from McCluskey and Haller.[7]

TYPE	NAME		Crystal	Lattice Constant [Å]	Band Gap (at 300 K)
Elemental	C	Carbon	diamond	3.57	5.47 (indirect)
	Si	Silicon	diamond	5.43	1.12 (indirect)
	Ge	Germanium	diamond	5.67	0.66 (indirect)
III-V	GaAs	Gallium arsenide	zincblende	5.65	1.42 (direct)
	AlSb	Aluminum antimonide	zincblende	6.14	1.58 (indirect)
	GaN	Gallium nitride	wurtzite	3.19 (a), 5.19 (c)	3.43 (direct)
II-VI	CdTe	Cadmium telluride	zincblende	6.49	1.43 (direct)
	ZnO	Zinc oxide	wurtzite	3.24 (a), 5.21 (c)	3.4 (direct)
	InAs	Indium arsenide	zincblende	6.06	0.36 (direct)
IV-VI	PbS	Lead sulfide	rocksalt	5.94	0.41 (direct)
	PbTe	Lead telluride	rocksalt	6.46	0.31 (direct)

$$v_h = \mu_h \mathcal{E} \tag{1.15}$$

In a crystalline system, the effective mass of an electron is lower than that of a hole (this can seen by building upon the band theory of solids presented earlier[2–4]). As a result, electrons in semiconductors tend to be more mobile than holes.

Supposing all charge carrier move with their drift velocities, the total number of carriers crossing a plane of unit area per second can be deduced by multiplying the drift velocity by the charge on the carrier (q) and the carrier density (N_c). The gives the carrier current density,

$$J = N_\mathrm{c} q v_\mathrm{D}. \tag{1.16}$$

Substituting equation (1.13) into equation (1.16) gives,

$$J = \left(\frac{N_\mathrm{c} q^2 \tau}{m} \right) \mathcal{E}. \tag{1.17}$$

This linear relationship is all too familiar Ohm's law. The expression in the parentheses is conductivity (its inverse is resistivity ρ), which can also be written as,

$$\sigma = \left(\frac{q}{m} \tau \right) (N_\mathrm{c} q) = \mu (N_\mathrm{c} q). \tag{1.18}$$

Charge carrier conductivity can then be seen as a product of charge density and mobility. Therefore large conductivities can be achieved by high concentrations of charge carriers (as in the case for metals), or large drift velocities giving rise to high charge carrier mobilities (as in the case for semiconductors).

Finally, it is useful to discuss charge carrier scattering from a quantum mechanical approach. Recall the example in section 1.1.1 with an electron in a crystal lattice under a weakly perturbing periodic potential. In a more general sense, solutions of the Schrödinger equation of a periodic potential in real space $\mathbf{r}$ must have the form:

$$\psi_\mathbf{k} = u_\mathbf{k}(\mathbf{k}) \exp(\imath \mathbf{k} \cdot \mathbf{r}), \tag{1.19}$$

where $u_\mathbf{k}(\mathbf{r})$ has the periodicity of the crystal lattice or $u_\mathbf{k}(\mathbf{r}) = u_\mathbf{k}(\mathbf{r}+\mathbf{T})$ with $\mathbf{T}$ being the translation vector of the lattice.[3] This is known as Bloch's theorem and it is true for any particle propagating in a lattice and under a periodic potential of any strength.[4] It is important to note that Bloch wavefunctions represent states that are stationary solutions to the Schrödinger equation. Therefore, these would persist forever in a completely periodic infinite crystal.[4] Hence, in the absence of disorder or boundaries charge carriers will not scatter. The Bloch approach to charge carrier scattering highlights their wavelike nature, where scattering only takes places due to a lack of periodicity in $\mathbf{r}$ space.

1.1.4 Intrinsic Semiconductors

A semiconductor completely free of impurities and defects is known as an intrinsic semiconductor. In the absence of ionizing radiation, all of the electrons in the conduction band and all the holes in the valence band are caused by thermal excitation. Therefore, the number of electrons in the conduction band equals the number of holes in the valence band. It follows that that electrons and holes in intrinsic semiconductors give equal contribution to material conductivity. Based on the formulation of equation (1.18), the theoretical limit for resistivity of a semiconductor is given by,

$$\rho = \frac{1}{en_i(\mu_e + \mu_h)}, \tag{1.20}$$

where e is the electron charge, n_i is the intrinsic carrier density, and μ_h and μ_e are the mobilities of electrons and holes respectively. Currently, silicon or germanium of even the highest purity falls short of this theoretical limit. For this reason, the electrical properties of real semiconductors are dominated by impurities.

1.1.5 Extrinsic Semiconductors

In a real semiconductor crystal, the constituent atoms in the lattice can be replaced with a wide range of defects that include substitutional impurities, interstitial impurities, vacancies, interstitial defects, and dislocations. Such crystal defects lead to electron states within the forbidden energy gap that in turn can strongly influence electrical properties. Such materials are known as extrinsic semiconductors and they are the lifeblood of modern semiconductor device technology. In modern solid-state applications, high purity semiconductors are doped with small concentrations of electrically active impurities that alter conductivity. To illustrate the effect of doping, single crystal silicon is used as an example.

Suppose a penta-valent (i.e. group V) impurity is introduced into silicon crystal lattice. At small concentrations (less than a few parts per million), impurity atoms will tend to occupy substitutional sites within the lattice by taking the place of the constituent silicon atoms. Here the group V impurity is surrounded by tetra-valent silicon (as shown in Figure 1.4a). This leaves the impurity's fifth electron lightly bound to the atom site. Therefore, only a small amount of energy is needed to excite it to form a conduction electron; which is not associated with a hole. For this reason, impurities of this type are called donors (since they donate electrons to the conduction band). As shown in Figure 1.5a, electrons of donor impurities occupy energy levels close to the top of the energy gap ensuring that large quantities of donor impurities are thermally ionized, meaning that the overall number of conduction electrons increases and is dominated by those coming from the impurity (i.e. donor electrons). The net effect then is a material which has a larger concentration of conduction electrons and a smaller concentration of holes than in a pure intrinsic material and is labeled as n-type. In n-type materials, electrical conductivity is mostly governed by the flow of electrons (the majority carriers) and the contribution from the flow of holes (the minority carriers) is minimal.

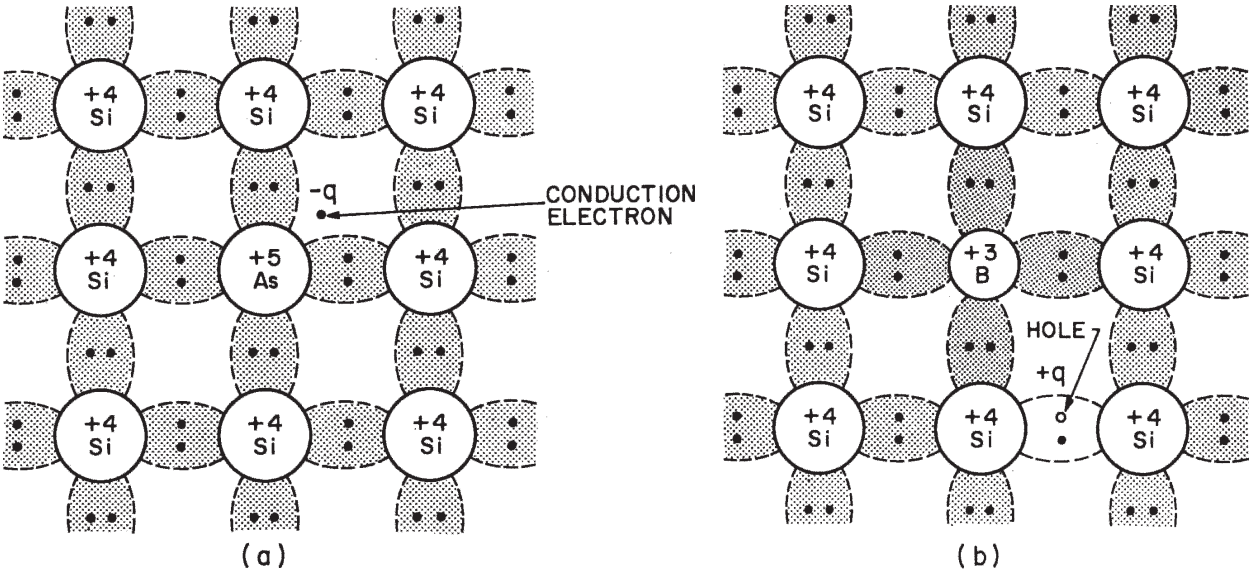

Figure 1.4: (a) Schematic of a donor impurity, where arsenic (group V element) occupies a substitutional site in silicon. (b) Schematic of an acceptor impurity, where boron (group II element) occupies a substitutional site in a silicon crystal as reproduced from Lutz.[9]

Now suppose that the group V impurity is replaced with a tri-valent (i.e. group III) impurity. Here, the impurity atom has one fewer valence electron than the surrounding silicon atoms. This leaves one covalent bond unfilled, which allows for the impurity atom to readily accept an electron to saturate the bond (Figure 1.4b). Not surprisingly, these impurities are known as acceptors. The energy levels created by the acceptor impurity are located in the forbidden energy gap close to the valence band (Figure 1.5b). Thus, the probability to thermally excite valence electrons to the acceptor energy levels becomes high. This process forms a hole in the valence band without a corresponding electron in the conduction band. The net effect here is a material that has a larger concentration of holes and a smaller concentration of electrons than in a pure intrinsic material and this is labeled as p-type. The flow of holes (as the majority carriers) contributes to the overall conductivity in a p-type semiconductor. Semiconductors can also be heavily doped to create materials with high conductivity for use in electrical contacts.

Both n-type and p-type semiconductors have larger concentrations of charge carriers than an intrinsic material. Therefore minimum conductivity occurs in completely pure materials. An excess of donor or acceptor impurities results in high conductivity (this is summarized in Figure 1. 6). If a semiconductor has equal concentrations of donor and acceptor impurities they can electrically cancel out and leaves an electronic structure similar to that of an intrinsic material.

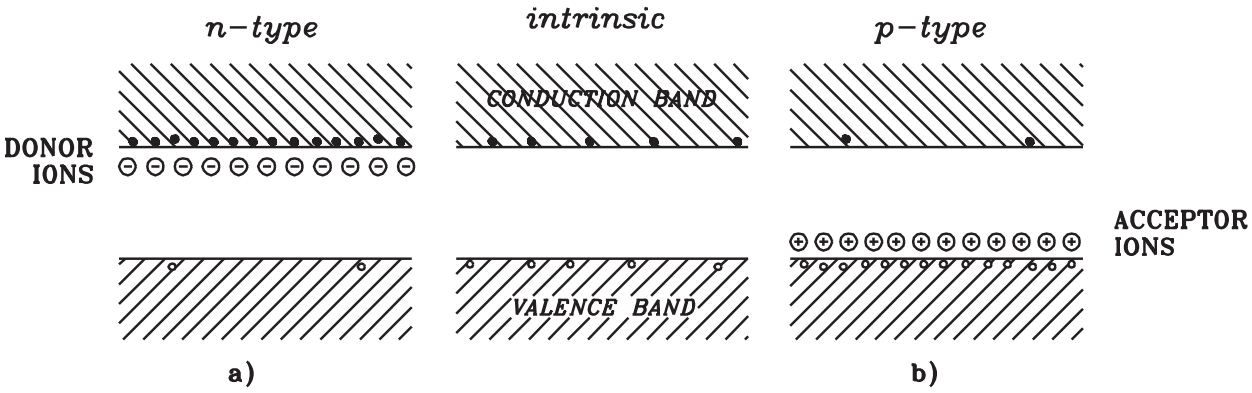

Figure 1.5: Band diagram representation of extrinsic n-type (a) and p-type (b) semiconductors compared with an intrinsic semiconductor as reproduced from Lutz.[9]

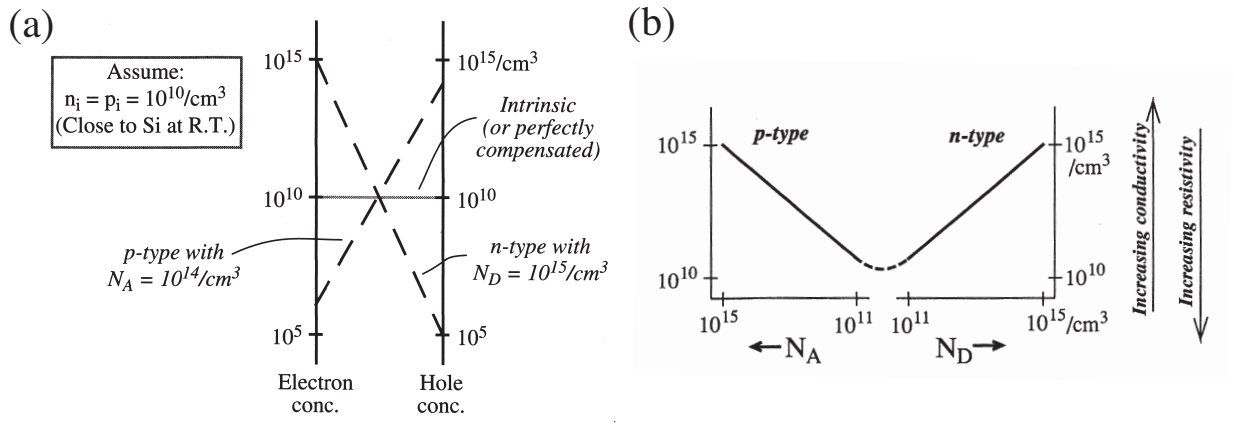

Figure 1.6: (a) Schematic illustration of the interplay between electron and hole concentrations in a silicon semiconductor at room temperature and (b) semiconductor conductivity as a function of the net concentration of donors (N_D) and acceptors (N_A) as reproduced from Knoll.[8]

1.2 Semiconductors as a Medium for Radiation Detection

The use of semiconductors as an ionization radiation detector has been readily explored since the 1940s when Van Heerden successfully detected gamma rays using AgCl crystals.[10] Traditionally, high-energy radiation was detected using scintillators and gases. In the former, radiation is detected by emitting light that is converted into an electric signal by a photomultiplier tube and can be read on an oscilloscope. In gases, the electric signal is related to the flow of ion pairs created by incident radiation. The unique properties of semiconductors have allowed for the fabrication of detectors with energy resolution that exceeds the optimal value

for standard scintillation and gas detectors. Nevertheless, there remains pressing challenges regarding crystal growth, control of impurities, and fabrication that limits the widespread use of semiconductor detectors.

1.2.1 Mechanisms of Semiconductor Radiation Detectors

The core principle behind all radiation detectors is the conversion of incident nuclear radiation into electronic signals that can be output on conventional display instruments. In the case of semiconductor devices, electron-hole pairs within semiconductor crystals are excited by ionizing radiation. Voltage applied across the detection medium creates an electric field that accelerates the charge carriers. The motion of the charge induces a corresponding current to flow in the external circuit. The current pulse can be integrated to measure the induced charge. This in turn allows one to determine the energy deposited by the incident radiation. The ionization energy required for electron-hole pair production is one order of magnitude less than that of gases.[8] As a result, incident radiation on semiconductors produces large amount of charge carriers (compared with gases and scintillators). This means large concentrations of information carriers that lead to drastically improved detector energy resolution.

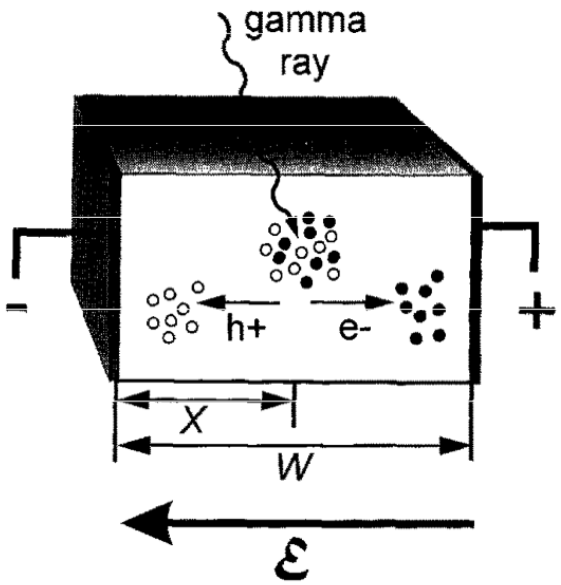

Figure 1.7: Representation of a semiconductor detector operating in a planar configuration as reproduced from McGregor and Hermon.[10] Incident radiation creates electron-hole pairs that are swept via an internal electric field created by an externally applied voltage.

To illustrate this process, consider a semiconductor slab of length W with two planar electrodes attached to each side (Figure 1.7). An internal electric field $\mathcal{E}$ is created by apply-

ing voltage across the device. Incident ionization radiation on the device excites electron-hole pairs in the semiconductor. The electric field in the semiconductor sweeps the electrons to the anode electrode and the holes to the cathode. A variation of the induced charge Q^* on the electrodes is generated by the moving carriers. The change of Q^* is converted to a voltage pulse using a charge sensing amplifier. Ideally, the amplitude of the voltage pulse is proportional to the energy deposited by the incident radiation. The induced charge dQ^* due to the motion of dx of charge carriers can be obtained from the Shockley-Ramo Theorem:[8,11–13]

$$dQ^* = \frac{-eN_0}{W}\left(dx|_e + dx|_h\right), \tag{1.21}$$

where N_0 is the initial number of electron-hole pairs and e is the electronic charge. Therefore, in a defect free intrinsic semiconductor full charge collection ($Q* = eN_0$) is possible.

In real semiconductors, full charge collection is not realized, as the presence of impurities and defects cause significant charge carrier trapping losses. As a result, the induced charge becomes a function of the distance over which the electron-hole pairs travel, which causes the outputted electric signal to be sensitive to the interaction position. This phenomenon is described by the Hecht relation:[8,14]

$$Q^* = eN_0\left\{\frac{v_h\tau_h^*}{W}\left(1-\exp\left[\frac{-x}{v_h\tau_h}\right]\right)+\frac{v_e\tau_h^*}{W}\left(1-\exp\left[\frac{x-W}{v_e\tau_e}\right]\right)\right\}, \tag{1.22}$$

where v is the charge carrier velocity, τ is the charge carrier mean lifetime, and x is location of the radiation interaction measured from the cathode (with the e and h subscripts denoting electrons and holes respectively). Thus, the induced charge caused by a single ionizing event become a function of the interaction location and the quantity $v\tau/W$ is known as the carrier extraction factor.[15] Recalling equations (1.14) and (1.15) the carrier extraction factor can also be written as $\mu\tau\mathcal{E}/W$. Hence, interaction location, charge mobility of a semiconductor, and the mean carrier lifetime are the major driving forces for good energy resolution. Since carrier mobilities and lifetimes are bulk constants for any given material, the size of the device becomes the only tunable parameter to improve detector performance.

Figure 1.8 illustrates the position dependence of the induced charge in a semiconductor device of various widths. For a device in which electrons and holes have similar transport properties (Figure 1.8a), interactions at the center of the detector will give the highest induced charge as both carriers have equivalent scattering obstacles. As the width of the device is reduced effects of position dependence diminish. In many semiconducting materials, however, the mobility of holes is significantly less than that of electrons. Consequently, the induced net charge becomes biased towards interaction positions near the cathode. It seems, then, that the easiest way to improve semiconductor radiation detector performance is to reduce the size of the device. Yet, devices thin enough that allow for position independence of the induced charge would be impractical as their detection efficiency would be severely reduced. Thus, the two remaining options are to apply single-polarity charge sensing techniques to remove eliminate the deleterious effects of slow charge carriers, or to improve detector material transport properties either through improved processing techniques (e.g.

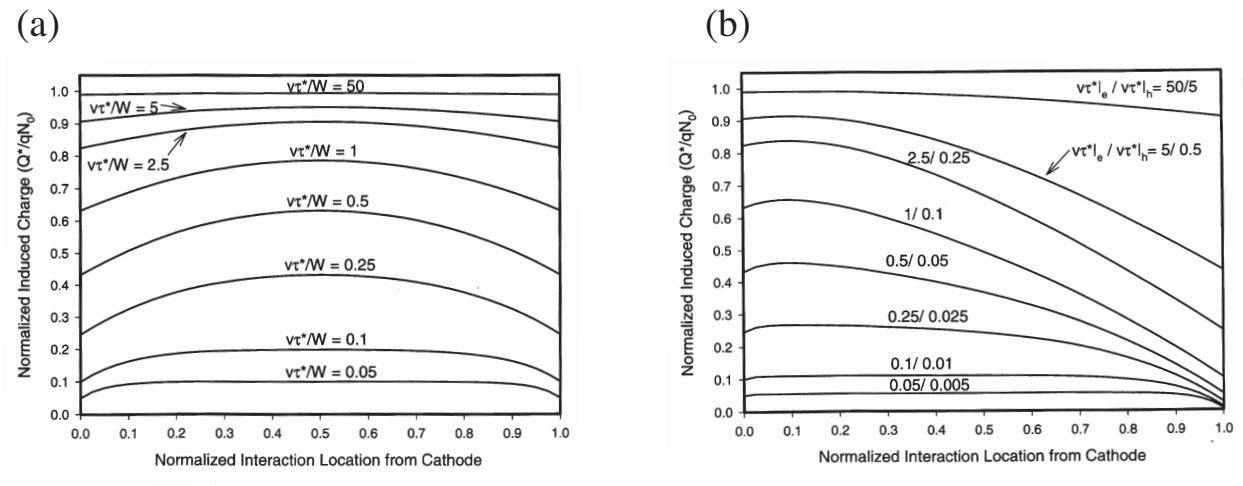

Figure 1.8: (a) Position dependence of induced charge in a semiconductor where electrons and holes have equivalent transport properties and (b) Position dependence of induced charge in a semiconductor where the carrier extraction factor for electrons is ten times that of holes as reproduced from Knoll.[8]

growth, purification), or searching for new materials. The latter, with an emphasis on novel semiconductor materials for radiation detectors, is the defining topic of this dissertation.

1.2.2 Properties of Semiconductor Materials for Radiation Detectors

Since the driving mechanism of semiconductor detector operation is the flow of charge carriers it follows that charge transport properties are paramount for the success of any given material as a radiation detection device. Accordingly, semiconductors of high purity, free of defects, and with high charge carrier mobility and lifetimes would make the ideal device. It is no surprise then that silicon and germanium are the reference standard solid-state devices. Silicon diode detectors are extensively used in charged particle spectroscopy research, while germanium, due to its relatively high atomic number (gamma-ray interaction cross sections increase with atomic number) is used in gamma-ray spectroscopy applications. There has been interest, however, for semiconductor devices suitable from room-temperature gamma-ray detection. In safeguards applications, for example, semiconductors are the only material capable of achieving energy resolutions that allow for isotopic identification of special nuclear material (e.g. ^{235}U). Due its low band gap (0.67 eV), germanium must be cooled to liquid nitrogen temperature to reduce electronic noise generated by thermally excited charge carriers. Moreover, bulk cooling apparatuses are not practical for use in harsh environments encountered in the safeguards field. As a result, considerable research has been taken on various compound semiconductors to achieve devices capable of room-temperature gamma-ray

spectroscopy with energy resolution comparable to that achieved using germanium.

Ideal semiconductors for room-temperature gamma-ray detectors must exhibit a diverse set of material properties. Of note are a high atomic number [Z≥40] for adequate radiation stopping power, a ≈1.5-2.0 eV band gap to minimize thermal charge carrier generation, carrier mobility-lifetime products exceeding 10^{-2} cm^2/V for electrons and 10^{-2} cm^2/V for holes, charge trapping center concentrations <1 part per billion.[16,17] Compound semiconductors commonly used as radiation detectors are listed in Table 1.2 Not surprisingly, no present single semiconductor strictly meets all these demands. Historically, cadmium zinc telluride (CdZnTe) has proven to be a viable semiconductor detector material for room-temperature gamma-ray detection. However, growth defects such as tellurium inclusions and crystal yield (which increases processing cost) has limited its use.[18,19] Thallium bromide (TlBr), with its higher atomic number can be an efficient detector, but polarization phenomena (where trapped charge carriers create a field that opposes the electric field externally applied to the detector), has been a major impediment for more widespread use.[20,21] Investigations that build upon and improve the properties of well known compound semiconductors (like CdZnTe and TlBr) are actively being pursued[22,23] . Consequentially, this has left a paucity of research on new classes of semiconductors that may be effective radiation detectors.

Table 1.2: Properties of semiconductors commonly used in radiation detectors as reproduced from Owens et al.[16]

Parameter	Si	Ge	CdZnTe	HgI_2	TlBr
Density [g/cm^3]	2.33	5.33	5.78	6.4	7.56
Average atomic number	14	32	49.1	62	58
Band gap (at 300 K) [eV]	1.12	0.67	1.57	2.15	2.68
Electron mobility [cm^2/Vs]	1400	3900	1000	100	30
Hole mobility [cm^2/Vs]	1900	1900	120	4	4
Electron lifetime [s]	$> 10^{-3}$	$> 10^{-3}$	3×10^{-6}	3×10^{-6}	2.5×10^{-6}
Hole lifetime [s]	10^{-3}	2×10^{-3}	1×10^{-6}	1×10^{-5}	3.7×10^{-5}
Electron $\mu\tau$ [cm^2/V]	>1	>1	4×10^{-3}	3×10^{-4}	5×10^{-4}
Hole $\mu\tau$ [cm^2/V]	≈1	>1	1.2×10^{-4}	4×10^{-5}	2×10^{-6}
Crystal Structure	diamond	diamond	zincblende	tetragonal	cubic (CsCl)

1.3 Dissertation Overview

In this dissertation, the quasi-binary Ga_2Te_3-Ga_2Se_3 semiconductor alloy is experimentally investigated. The ensuing chapters are organized as follows: Chapter 2 provides an overview of $Ga_2(Se_{1-x}Te_x)_3$ and its related compounds. Chapter 3 is concerned with synthesis and crystal growth. Chapter 4 highlights x-ray diffraction studies. Chapter 5 deals with x-ray absorption studies. Chapter 6 details electron microscopy investigations. Chapter 7

is concerned with positron annihilation studies. Chapter 8 highlights measuring physical properties and finally Chapter 9 discusses conclusions and future work.

Chapter 2

Semiconductors with Defect Zincblende Structure

2.1 Structure

$Ga_2(Se_{1-x}Te_x)_3$ is a semiconductor belonging to a class of III-VI materials that exhibit a cubic zincblende crystal structure ($F\bar{4}3m$ space group) dominated by stoichiometric or "structural" vacancies–otherwise known as defect zincblende. The structural vacancies in these materials arise due to the valence mismatch between the anion and cation forcing 1/3 of the cation sites to be vacant. These defects are an intrinsic feature in the structure, hence, their effects on material properties would differ compared to that of extrinsic defects or impurities seen in conventional semiconductors. For this reason, there has been considerable interest in these types of a materials because there is a potential for engineering material properties by only tailoring the intrinsic structure of the material. In this chapter, an overview of early and recent research on bulk properties of this class of materials is presented.

2.1.1 Crystallography

Some of the earliest structural investigations on III-VI chalcogenide semiconductors date back to the 1940s, when Hahn and Klingler reported the crystal structure of Ga_2Se_3, Ga_2Te_3, and In_2Te_3.[24,25] They observed a cubic zincblende structures (with 1/3 of cation vacancies) with lattice constants of $a = 5.41$ Å, $a = 5.87$ Å, and $a = 6.13$ Å for Ga_2Se_3, Ga_2Te_3, and In_2Te_3 respectively. Hahn later observed that annealing In_2Te_3 gave rise to additional superlattice reflections in the diffraction patterns.[26] Vacancy ordering was suspected, though the nature of the ordering was not discussed. Later work by Wolley et al attempted to determine a structure that represents the superlattice reflections.[27] Based on their analysis two structures were posited: the first assumes only zincblende atomic sites are available for vacancy ordering, which gives a body-centered orthorhombic structure (Imm2 space group); and the second allows for the possibility that cations may reside in a CaF_2 lattice in alternate positions, which gives a tetragonal structure (space group of either P42mcm or P42nm). These are shown in Figures 2.1 and 2.2. It was noted, however, that experimental work did not provide ample evidence to justify a choice of either structure.

The structure of Ga_2Se_3 was carefully studied by Lübbers and Leute.[28] In their powder diffraction work, they reported an ordered vacancy superstructure, originating from the defect zincblende lattice (denoted as denoted as α-Ga_2Se_3). It was observed to be monoclinic (denoted as β-Ga_2Se_3) with lattice parameters $a = 6.66$ Å, $b = 11.65$ Å, $c = 6.50$ Å, and β=108.84°. The space group was seen to be C4sCC. In α-Ga_2Se_3 the vacancies are disordered. A schematic of β-Ga_2Se_3 is shown in Figure 2.3. In β-Ga_2Se_3, it was deduced that the vacancies form continuous unbranched chains that propagate in the [001] direction in the crystal.

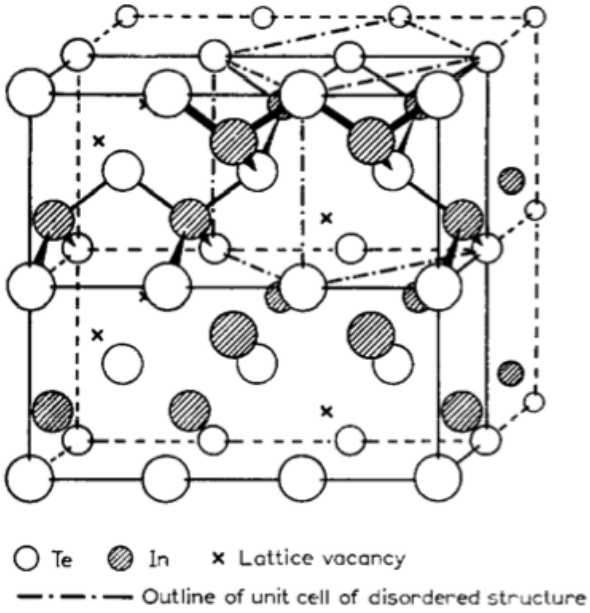

Figure 2.1: Representation of In_2Te_3 orthorhombic superstructure by proposed Woolley et al.[27]

A superlattice structure in Ga_2Te_3 was first observed by Newman and Cundall.[29] In their powder diffraction patterns, the expected cubic zincblende reflections were observed in addition to seven reflections that could not be index to the cubic cell. One reflection was attributed to Te and the others were indexed to an orthorhombic cell with seven possible space groups. More recently, Singh et al were able to posit an additional superlattice based on a hexagonal crystal structure.[30] Moreover, they posited that the zincblende form of Ga_2Te_3 is metastable and gradually transforms to the hexagonal phase at room temperature.

Detailed single-crystal diffraction experiments investigating superstructures in Ga_2Te_3 have been carried out by Otaki et al.[31,32] As-grown and quenched Ga_2Te_3 crystals were analyzed. The single crystal diffraction maps for both crystals showed a cubic zincblende structure, but with prominent superstructure reflections around the Bragg reflections, which were attributed to modulated vacancy structures. It was argued that the modulations consisted of two components: an amplitude modulation caused by Ga vacancies and a displacive modulation of the surrounding Te atoms, which has a polarization vector along [001] in the zincblende cubic lattice. These are highlighted in Figure 2.4. Depending on the thermal history of the Ga_2Te_3 crystal, the position of satellite reflections with respect to the Bragg peaks differ. This means that one can drive the orientation of vacancy structures in through thermal means in Ga_2Te_3.

Otaki et al and Kashida et al argued that the origin of they observed structural modulations in Ga_2Te_3 were electronic in nature.[31–33] They hypothesized that the Ga vacancy in Ga_2Te_3 leaves four unattached orbitals (via Ga-Te tetrahedra). The dangling orbitals

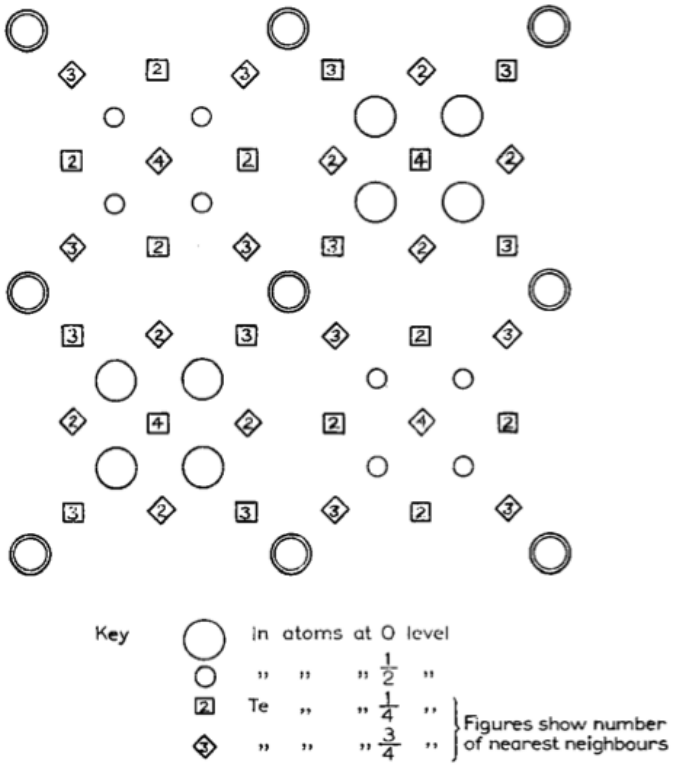

Figure 2.2: Representation of In_2Te_3 tetragonal superstructure proposed by Woolley et al.[27]

combine to form singlet and triplet states. If one assumes the vacancy is neutral, then four electrons would be distributed across these states. In a cubic arrangement, this causes an orbital degeneracy that raises the overall energy of the system with respect to Jahn-Teller distortions (illustrated in Figure 2.5). Hence, the system distorts to a tetragonal configuration to lower its energy, and the third and fourth electrons pair up and occupy a single state.

2.1.2 Electron Microscopy

Electron microscopy studies on bulk Ga_2Te_3 and Ga_2Se_3 have helped serve as direct probes to the structural vacancy dynamics in materials with defect zincblende cubic structure. One of the earliest detailed electron microscopy investigations was carried out by Guymont et al.[34] In the collected electron diffraction patterns they observed Bragg reflections associated with a zincblende structure, but with additional streaks along <111> directions that connect the Bragg spots (shown in Figure 2.6). It was noted that such diffraction features indicate disorder in the stacking of {111}. Imaging revealed two dimensional vacancy structures of width no more than one Ga_2Te_3 motif (shown in Figure 2.6). Based on these results, a preliminary structure was proposed composed of a mosaic of ordered zincblende do-

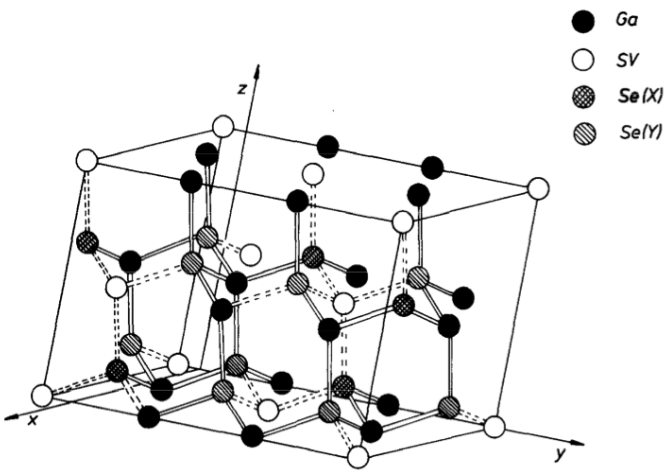

Figure 2.3: Representation of β-Ga_2Se_3 monoclinic superstructure proposed by Lübbers and Leute.[28]

mains bounded by plane defect boundaries. Additional information on the defect boundaries could not be ascertained due to the low intensity of the streaks in the electron microscope images.

More recent work by Kienle et al and Kurosaki et al showed that annealing bulk Ga_2Te_3 produces a 10-fold superstructure composed of two-dimensional vacancy structures along <111>.[35,36] Here, the ordered superstructure produced rhomboid domains with a length of 3.5 nm (Figure 2.7). The local environment around the structure around the ordered vacancy structure was not discussed. However, Kim et al showed that if Ga_2Te_3 is slowly cooled after annealing, the two-dimensional vacancy structures go back to their disordered configuration.[37]More recent work by Kienle et al and Kurosaki et al showed that annealing bulk Ga_2Te_3 produces a 10-fold superstructure composed of two-dimensional vacancy structures along <111>.[35,36] Here, the ordered superstructure produced rhomboid domains with length 3.5 nm (Figure 2.7). The local environment around the structure around the ordered vacancy structure was not discussed. However, Kim et al showed that if Ga_2Te_3 is slowly cooled after annealing, the two-dimensional vacancy structures go back to their disordered configuration.[37] Kim et al also investigated the structure of bulk Ga_2Se_3. It was seen that Ga_2Se_3 annealed at temperatures close to melting ($\approx$ 900 °C) produces two dimensional vacancy structures. Annealing at lower temperatures ($\approx$ 600 °C) produced point-type defects. This is illustrated in Figure 2.8.

2.2 Physical Properties

The structural work highlighted in the previous section shows that vacancies in defect zincblende crystals have a tremendous influence on the overall structural dynamics. Conse-

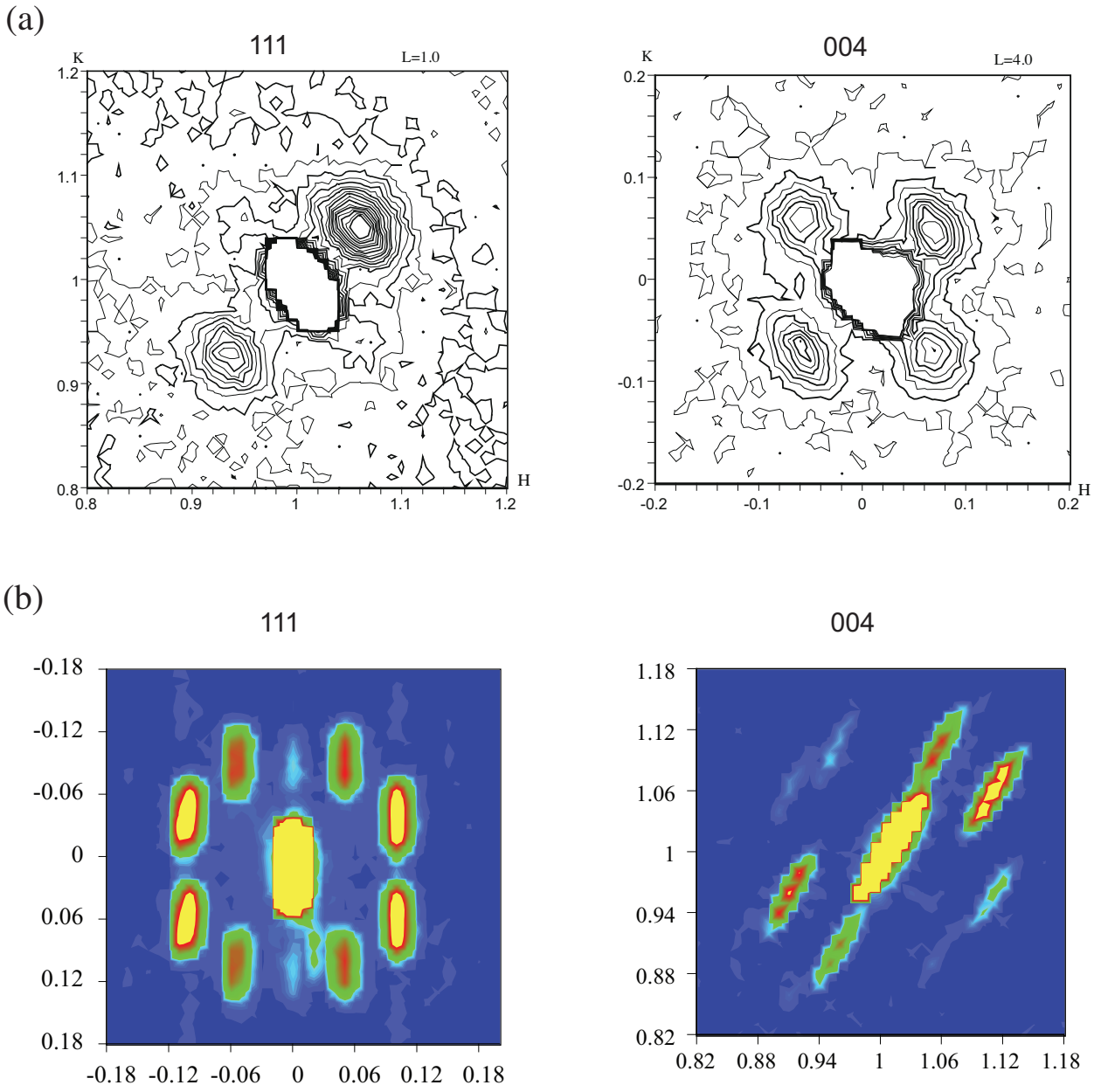

Figure 2.4: (a) Single crystal diffraction maps of quenched Ga_2Te_3 at the 111 and 004 Bragg reflections and (b) single crystal diffraction maps of as-grown Ga_2Te_3 at the 111 and 004 Bragg reflections as reproduced from Otaki et al.[31,32]

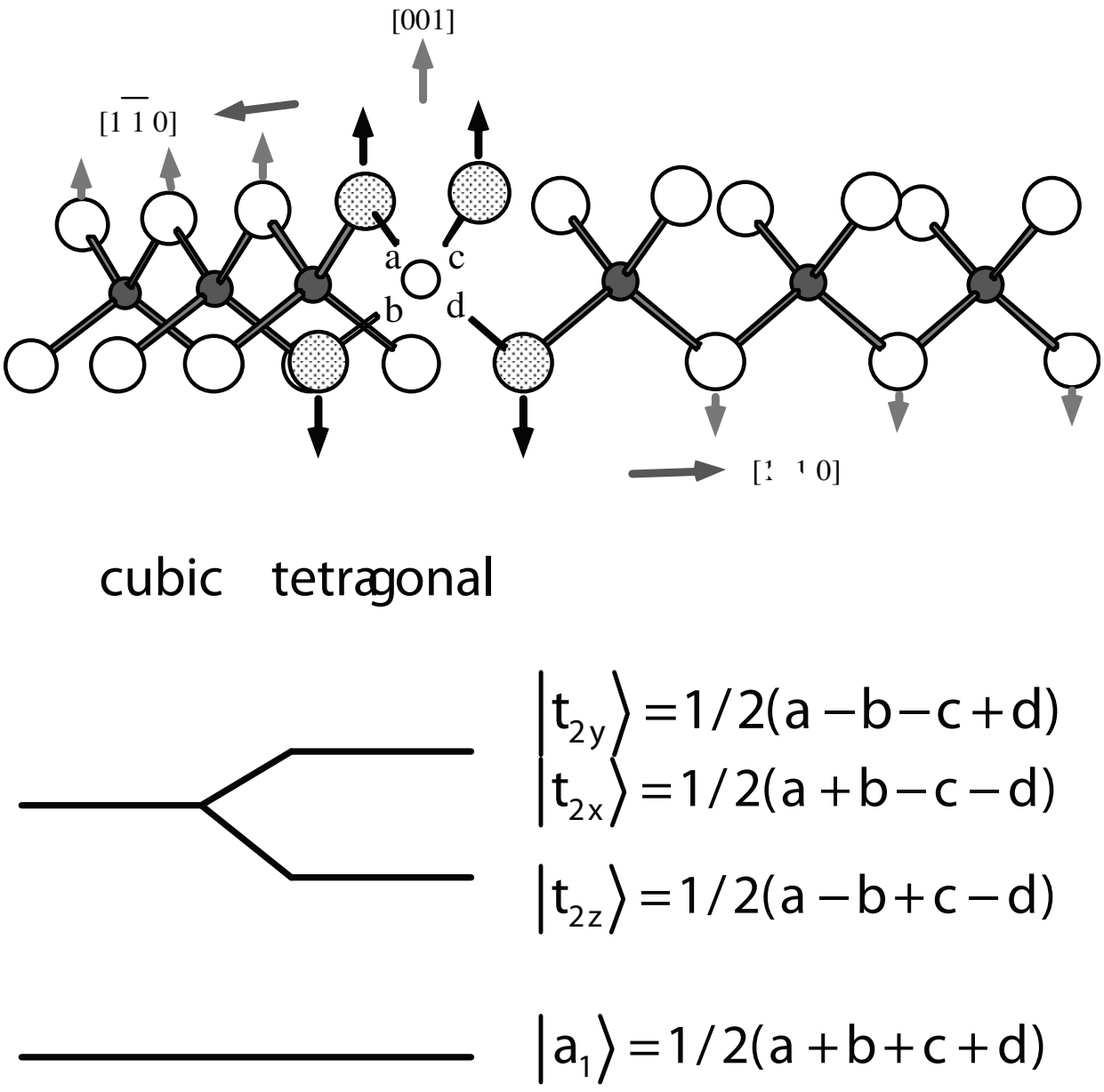

Figure 2.5: Illustration of hypothesized Jahn-Teller distortion of the cubic zincblende structure caused by Ga vacancies reproduced from Kashida et al.[33] The structure distorts to a tetragonal configuration through energy splitting.

quently, the effect of structural vacancies on the physical properties of this class of material has been of great interest. This section highlights experimental work on the bulk properties of Ga_2Te_3, Ga_2Se_3, and related compounds.

2.2.1 Electrical Properties

Some of the earliest comprehensive studies on the electrical properties of defect zincblende semiconductors were carried out by Bose et al.[38,39] They reported that they synthesized In_2Te_3 as p-type semiconductor and Ga_2Te_3 as n-type.[39] Hole mobility in In_2Te_3 reached a maximum of 210 cm^2/Vs at 77 °C. Electron mobility in Ga_2Te_3 showed a weak maximum value of 28 cm^2/Vs at 77 °C. It was posited that carrier mobility decreases after a critical temperature due to creation of ionized defects that drive down mobility. More recent measurements on Ga_2Te_3 single crystals by Julien et al also reported n-type conductivity, but the observed electron mobility (at room-temperature) was 0.31 cm^2/Vs.[40] The low carrier mobility was attributed to tellurium oxide (TeO_2) formation from air exposure during conductivity measurements.

Gamal and Elshaik, and Belal et al have investigated the electron conductivity properties of bulk Ga_2Se_3.[41,42] Conductivity in Ga_2Se_3 was reported to be p-type. Based on temperature dependent Hall effect measurements the hole mobility at room temperature was deduced to be 1995 cm^2/Vs.[41] From a technological standpoint this appeared to be very promising. However, a phase transition does occur in Ga_2Se_3 (β-Ga_2Se_3 to α-Ga_2Se_3). This makes reproducible crystal growth difficult and not practical for use in devices.

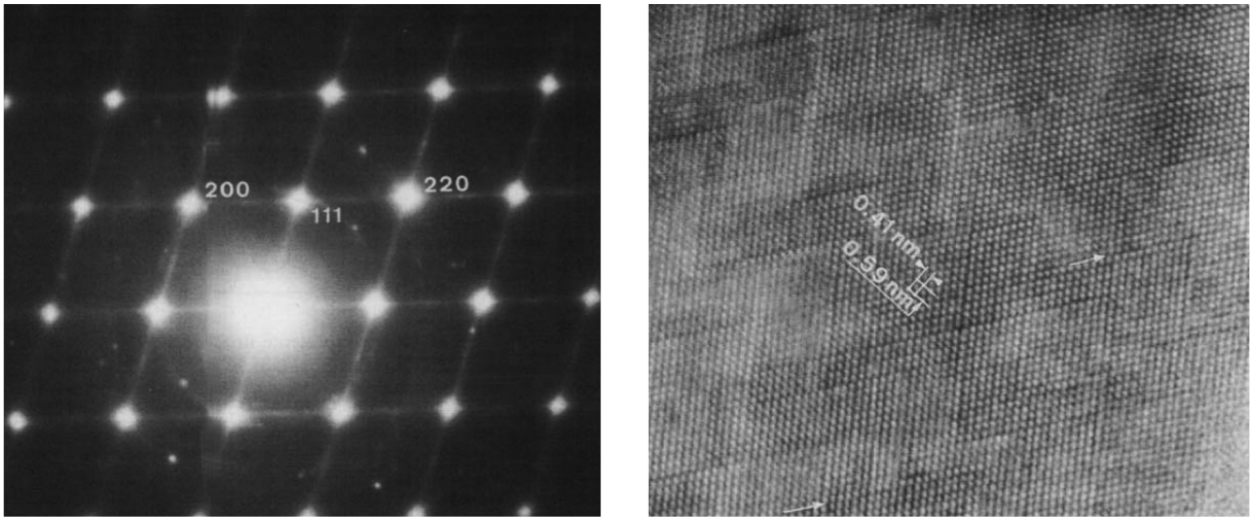

Figure 2.6: Electron diffraction pattern and image of Ga_2Te_3 (incident electron beam along [110]) as reproduced from Guymont et al.[34]

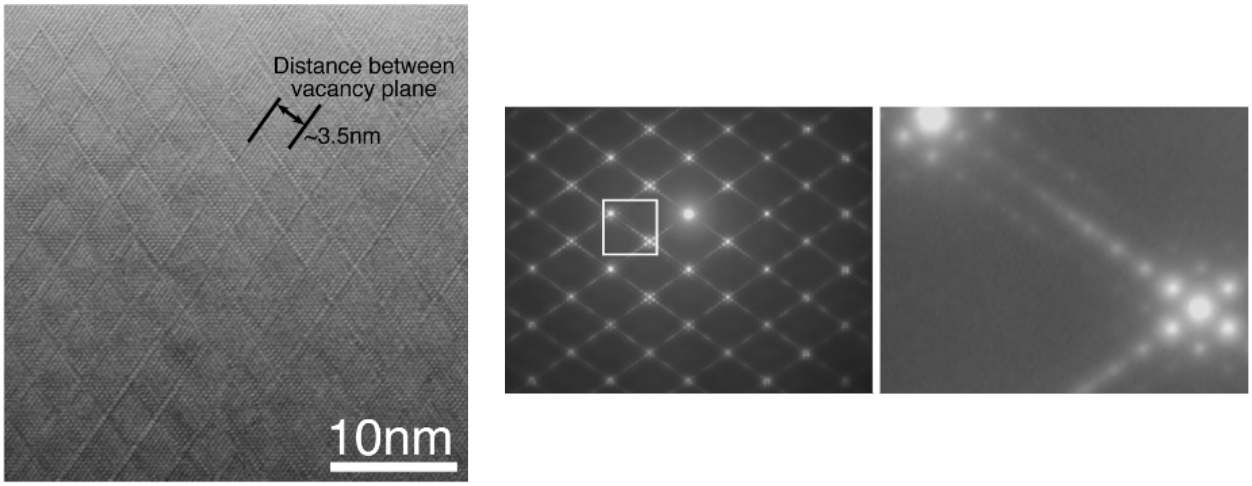

Figure 2.7: Electron diffraction pattern and image of Ga_2Te_3 with ordered two dimensional vacancy structures re (incident electron beam along [110]) reproduced from Kurosaki et al.[36]

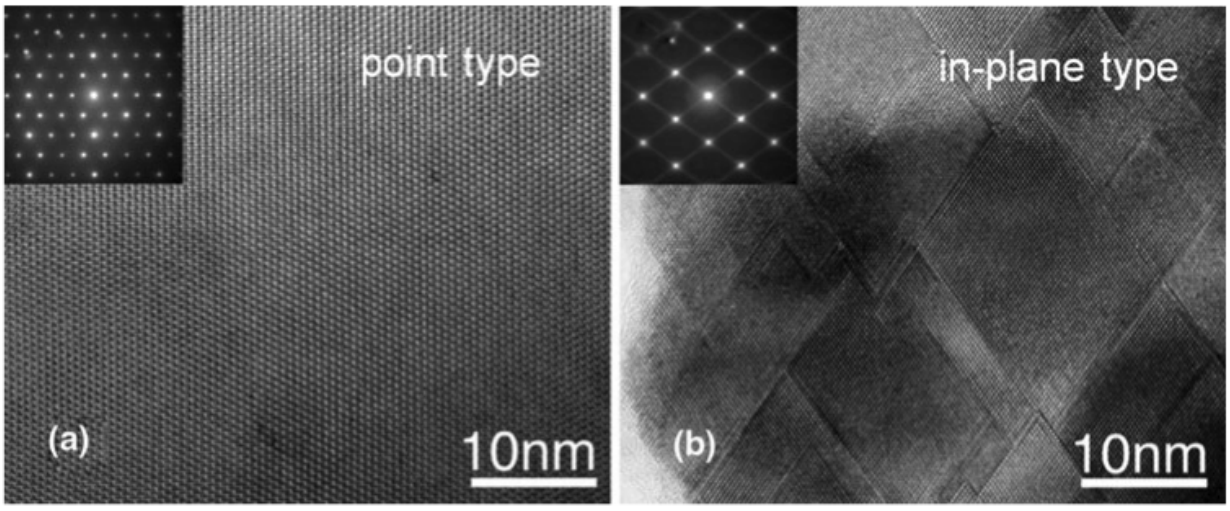

Figure 2.8: (a) Ga_2Se_3 with point-type vacancies produced by low-temperature (600 °C) annealing and (b) Ga_2Se_3 with two dimensional vacancies created by annealing close to the melting temperature (900 °C) reproduced from Kim et al.[37]

2.2.2 Optical Properties

Sen and Bose reported a direct band gap of 1.01 eV for In_2Te_3[39] via optical absorption measurements. Annealing In_2Te_3 at 77° C increased its band gap to 1.04 eV. The band gap of bulk Ga_2Te_3 is also direct with values reported ranging from 1.0 to 1.2 eV.[39,43–45] A direct band gap was observed for Ga_2Se_3 and values ranged from 2.0 to 2.5 eV.[46–48] Additional optical measurements on Ga_2Se_3 revealed that the ordered-vacancy phase (β-Ga_2Se_3) can act as a light polarizer.[49–51]

2.3 Technological Applications

There has been renewed interest in semiconductors with structural vacancies for use in thermoelectric and phase-change random access memory applications. Ga_2Te_3 as a phase-change material, for example, shows better data retention ability, lower power consumption, and higher dynamic electric switching ratios when compared to the better-known $Ge_2Sb_2Te_5$ [52]. Moreover, naturally occurring two-dimensional ordered vacancy planes in Ga_2Te_3 have been observed to be effective phonon scattering centers resulting in very low thermal conductivity, showing great potential as a thermoelectric material [36]. More recently, it was seen that vacancy ordering serves as the mechanism for metal-insulator transitions observed in $GeSb_2Te_4$ and the unexpectedly low thermal conductivity in Ga_2Te_3 [36, 53, 54].

III-VI defect zincblende semiconductors have also displayed anomalously high radiation stability.[55–58] Single crystal and polycrystalline specimens of In_2Te_3, Ga_2Te_3, and Ga_2Se_3 were exposed to a flux of 1.2 MeV γ-quanta up to a dose of 3×10^{22} m^{-2}, a flux of fast electrons (with energies up 100 MeV) up to a dose of 3×10^{23} m^{-2}, and a flux of mixed γ-neutron radiation from stationary and pulsed nuclear reactors up to a dose of 10^{23} m^{-2}.[55] Parameters such as charge carrier concentration, charge carrier mobility, and microhardness measured before and after irradiation show little or no change.[55] Such observations can be explained by the presence of structural vacancies which minimize Frenkel pair production from incident radiation (as opposed to elemental and III-V cubic semiconductors with no fractional cation occupancies).[55,58] As a result, these class of materials may be applicable for nuclear particle detection or for semiconductor devices operating in high radiation environments.

2.4 Motivation for Studying $Ga_2(Se_{1-x}Te_x)_3$

$Ga_2(Se_{1-x}Te_x)_3$ is a quasi-binary Ga_2Te_3-Ga_2Se_3 solid solution. Similar to the binary III-VI compounds, $Ga_2(Se_{1-x}Te_x)_3$ semiconductors may also have potential for thermoelectric, phase-change, and radiation detection applications applications. The calculated average number of covalence electrons per single atom (N_{sp}) is 4.8, which meets a key criterion for successful phase-change materials [59]. Moreover, since the structure would be similar to that of Ga_2Te_3 and Ga_2Se_3, low thermal conductivity and radiation stability are also expected. Unlike the binaries, however, the ternary system provides the possible advantage of band-

gap engineering. This allows for the production of $Ga_2(Se_{1-x}Te_x)_3$ semiconductors with band gaps suitable for room-temperature gamma-ray detection. It is with this mindset that the research in this dissertation began, but during the process, a variety of interesting physical properties were uncovered.

Chapter 3

Synthesis and Crystal Growth

3.1 Synthesis

In this section, an overview of $Ga_2(Se_{1-x}Te_x)_3$ synthesis is presented.

3.1.1 Phase Diagrams

$Ga_2(Se_{1-x}Te_x)_3$ is a Ga_2Te_3-Ga_2Se_3 alloy. Hence, in the initial stages of synthesis it useful to first consult the Ga-Te and Ga-Se binary phase diagrams (shown in Figure 3.1). Two features that differentiate Ga_2Te_3 and Ga_2Se_3 are noticed. First, Ga_2Se_3 melts at a higher temperature ($\approx$ 1000 °C) when compared with Ga_2Te_3 ($\approx$ 800 °C). Second, Ga_2Se_3 undergoes a phase transition from β-Ga_2Se_3 to α-Ga_2Se_3 at $\approx$ 730 °C. Recall from chapter 2 that the β phase is a vacancy-ordered monoclinic structure and the α phase is a cubic zincblende structure with disordered vacancies. This high temperature phase transition renders growth of Ga_2Se_3 single crystals difficult as this material will likely to crack as the melt is solidified. Ga_2Te_3, on the other hand, shows no such phase transition. In addition its lower melting temperature makes it more practical for growth as partial pressure in chalcogenide compounds are relatively high, and evaporation of constituents becomes more prominent at higher temperatures. For this reason, Ga_2Te_3 is taken as a starting point for $Ga_2(Se_{1-x}Te_x)_3$ synthesis. Recall that the band gap of Ga_2Te_3 ($\approx$ 1 eV) is too low for room temperature gamma ray detectors, hence selenium is added to the mixture to tune the semiconductor band gap.

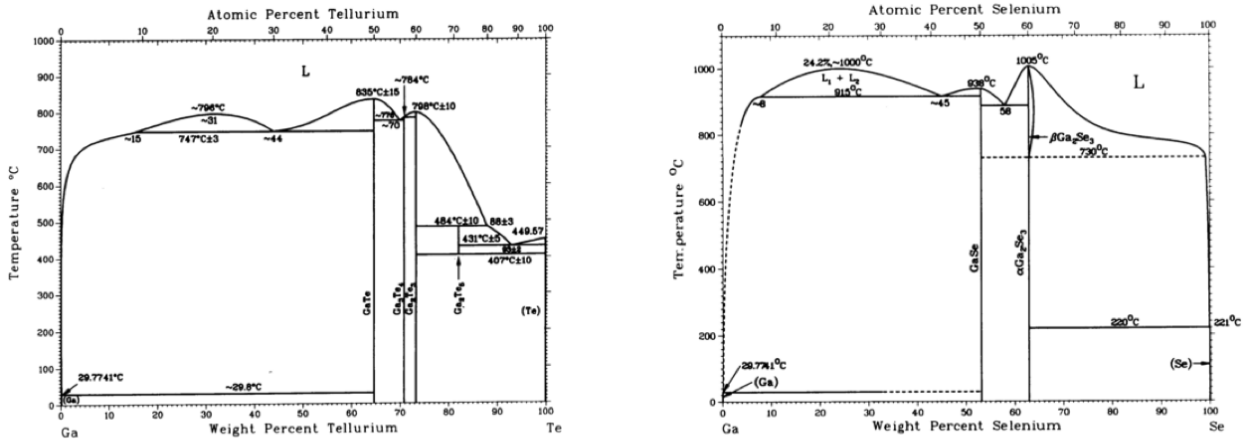

(a) (b)

Figure 3.1: (a) Ga-Te phase diagram and (b) Ga-Se phase diagram.[60]

The phase diagram of the quasi binary Ga_2Te_3-Ga_2Se_3 alloy system has been studied by Warren et al and Kerkhoff and Luete.[61,62] The conclusions reached by the two studies differ slightly. Warren et al reported that $Ga_2(Se_{1-x}Te_x)_3$ is not composed of a series of continuous Ga_2Te_3-Ga_2Se_3 solid solutions and exhibits an immiscibility gap for selenium atom fraction range $0.5 \leq x_{Se} \leq 0.90$. In this range, powder diffraction patterns showed lines corresponding to two zincblende structures with different lattice constants. The phase digram and lattice constant observed by Warren et al are shown in Figures 3.2a and 3.3b respectively.

Kerkhoff and Luete, conversely, concluded that Ga_2Te_3-Ga_2Se_3 is completely soluble for all selenium atom fractions. Moreover, they concluded that while the pure binary components (Ga_2Te_3 and Ga_2Se_3) exhibit a defect cubic zincblende structure, the ternaries exhibit a tetragonal structure that are based on a weakly distorted cubic zincblende crystals. At a selenium fraction of $\approx 2/3$, the ternary system was believed to revert back to cubic. The phase diagrams and lattice constants observed by Kerkhoff and Luete are shown in Figures 3.2b and 3.3b respectively. As will be seen in the next chapter, x-ray diffraction work done in this dissertation showed phase behavior equivalent to the observations reported by Warren et al and none of the effects observed by Kerkhoff and Luete were observed. Thus, all grown $Ga_2(Se_{1-x}Te_x)_3$ samples studied in this dissertation fell in the range of $0.5 \leq x \leq 1.0$.

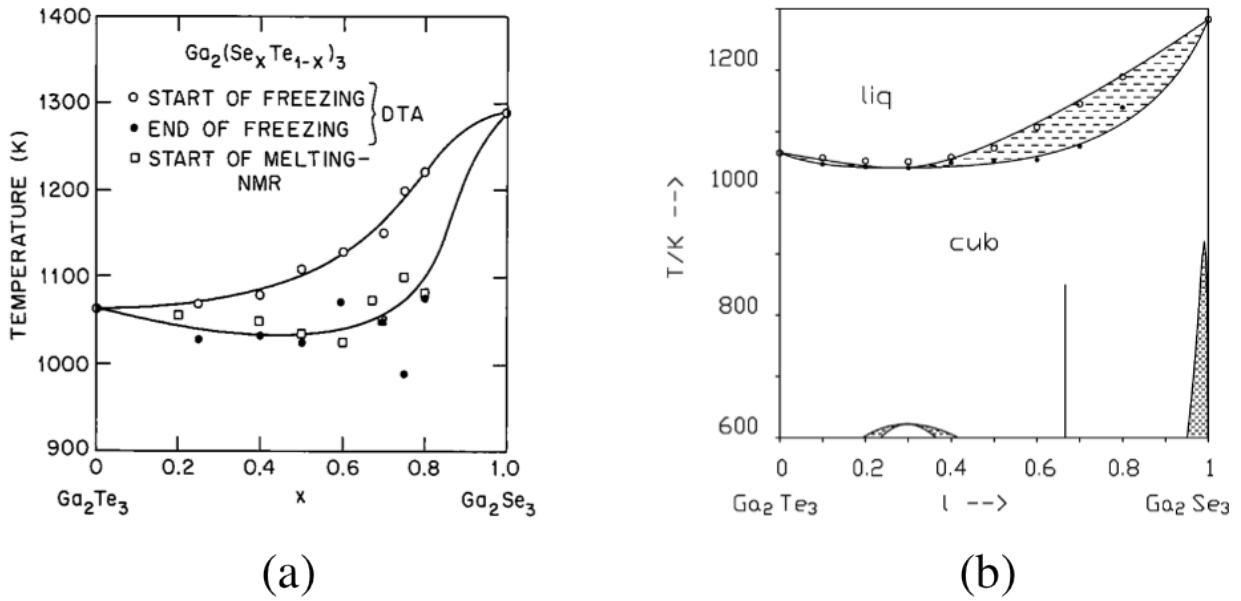

Figure 3.2: (a) Ga_2Te_3-Ga_2Se_3 phase diagram determined by Warren et al via differential thermal analysis (DTA) and Nuclear Magnetic Resonance (NMR).[61] (b) Ga_2Te_3-Ga_2Se_3 phase diagram determined by Kerkhoff and Luete via DTA.[62]

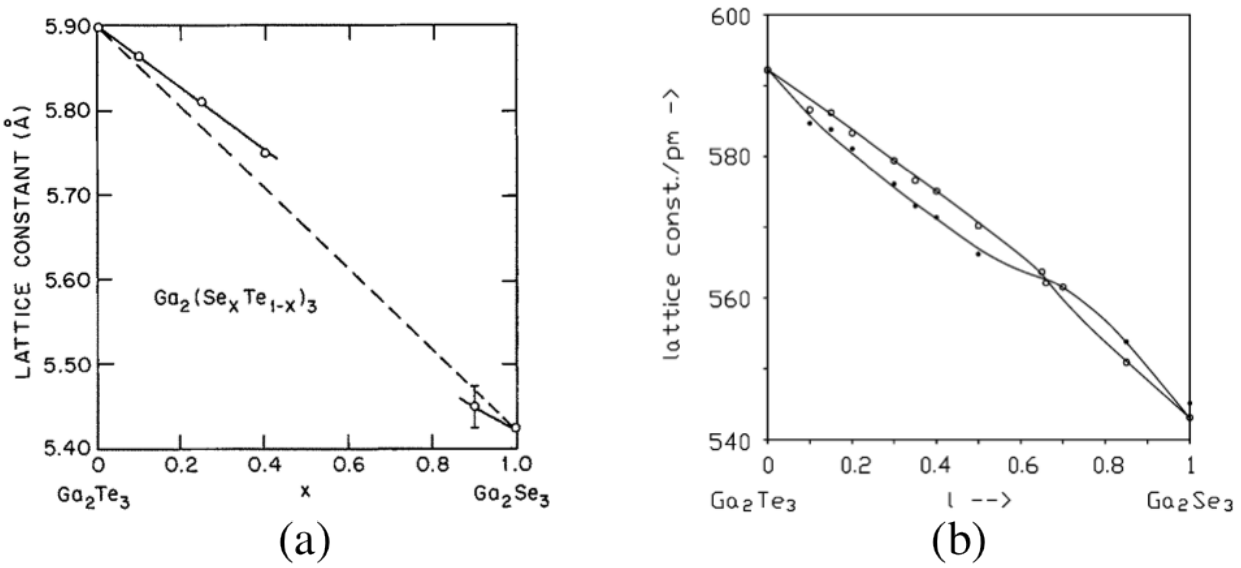

Figure 3.3: (a) Lattice constant a determined by Warren et al[61] and (b) Lattice constants a (open ciricles) and c (filled circles) determined by Kerkhoff and Luete.[62]

3.1.2 Procedure

$Ga_2(Se_{1-x}Te_x)_3$ compounds with $0.5 \leq x \leq 1.0$ were synthesized using stoichiometric amounts of 8N gallium, 6N selenium, and 6N tellurium sealed in quartz crucibles (1.3 cm in diameter) under vacuum (10^{-5} to 10^{-6} Torr). The quartz crucible was placed on an incline (to allow for good mixing) in an alumina boat, and the boat was placed in a 20 cm horizontal tube furnace. Figure 3.4a shows a schematic of the setup of the furnace. A synthesis temperature of 850 °C was used, where the measured profile showed a gradual rise in temperature going from the left to the right of the furnace. Specifically, temperatures of 830 °C at the left end, 855 °C in the middle, and 860 °C at the right end were measured. The stoichiometric amounts of gallium, selenium, and tellurium were allowed to react for 36 h, then the system was cooled directionally at a rate of 0.3 °C/min in an attempt to grow small single crystals. Resulting ingots were composed of small single crystals mixed in a polycrystalline mass of the same composition. The small single crystals were harvested (Figure 3.4b) and the polycrystalline mass was used as the charge for growth of larger single crystals.

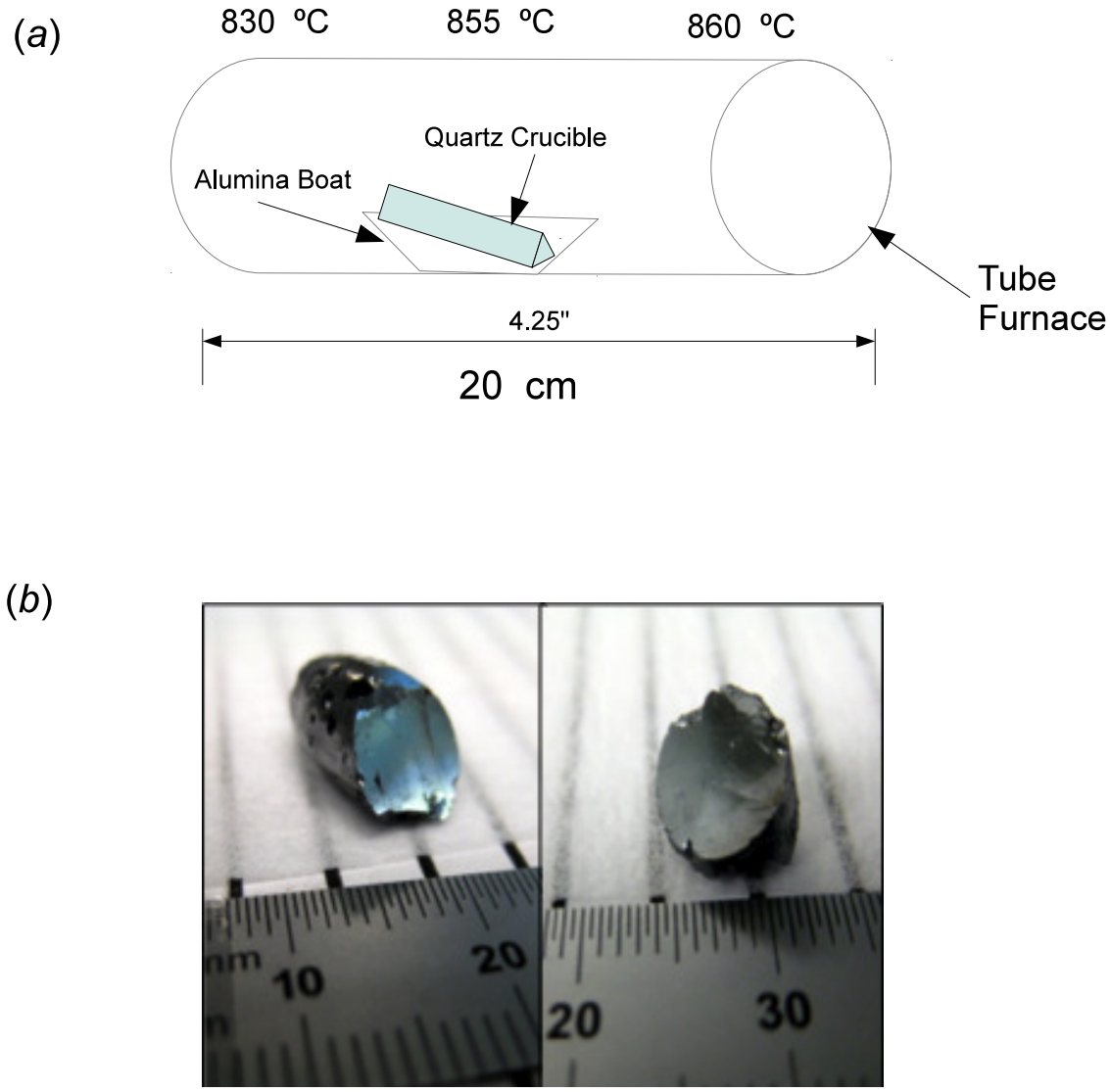

Figure 3.4: (a) Schematic showing the temperature profile and synthesis setup using a horizontal tube furnace an (b) Crystal facets grains of $Ga_2Se_{0.3}Te_{2.7}$ with size on the order 1-2 mm can be harvested from the polycrystalline ingot.

3.2 Crystal Growth

In this section, crystal growth techniques employed for growing bulk $Ga_2(Se_{1-x}Te_x)_3$ crystals are presented. The fundamentals of crystal growth kinetics will first be discussed. Then techniques and procedures used are detailed. Finally, results from the growth experiments are presented.

3.2.1 Crystal Growth Kinetics

All crystal growing techniques follow two basic heat flow objectives: (1) Establish a thermal gradient across a solid-liquid interface that is maintained at equilibrium (i.e. a stable interface that does not move), and (2) Move the temperature gradient in such a way that the solid-liquid interface moves at a controlled rate.[63–65] From basic heat transfer theory, the heat balance at a planar solid-liquid interface can be written as,

$$K_S \frac{dT_S}{dx} + K_L \frac{dT_L}{dx} = f \rho_S H, \tag{3.1}$$

where K_L is the thermal conductivity of the liquid, K_S is the thermal conductivity of the solid, dT_L/dx is the temperature gradient in the liquid at the solid-liquid interface, dT_S/dx is the temperature gradient in the solid at the solid-liquid interface, f is the growth velocity, ρ_S is the density of the solid, and H is the heat of fusion. The growth velocity is highly dependent on the difference between the product of the thermal conductivity and the Gibbs free energy of the sold and liquid.[64] Therefore the maximum growth rate $f_{\max}$ is achieved when the Gibbs free energy of the liquid approaches zero, which gives

$$f_{\max} = \frac{K_S}{\rho_S H} \frac{dT_S}{dx} \tag{3.2}$$

This shows that the maximum growth rate is determined by the magnitude of the temperature gradient in the solid at the solid-liquid interface.

A fundamental thermal consideration in the crystal growth process requires the heat flowing in the crystal away from the growth interface must be greater than the rate of the heat of fusion. From equation (3.3), this can be stated as

$$K_S \frac{dT_S}{dx} > f \rho_S H. \tag{3.3}$$

If this requirement is not met the temperature falls as the growth interface moves further into the melt, which leads to an unstable solid-liquid interface. In real materials, the melt contains impurities or its stoichiometry deviates from the maximum melting composition. As a result, the temperature gradient in the liquid at the solid-liquid interface cannot be neglected and its minimum value is given by

$$\frac{dT_L}{dx} > mCf \left(1 - \frac{C_S}{C_L}\right) / D, \tag{3.4}$$

where m is the rate of change of the melting point of a given material with impurity concentration C, D is the diffusion coefficient, f is the growth rate, and the ratio C_S/C_L is the ratio of impurity concentrations in the solid and liquid phases, also known as the segregation coefficient.[65] Thus, in addition to higher temperature gradients, higher growth rates can also be achieved by using higher purity materials.

The concentration of impurities in a grown crystalline ingot will vary across its length. Usually, the concentration of impurities is lowest where growth began and increases further along the crystal. For example, if the growth interface occurred in a melt situated vertically the purest material will be towards the bottom. This characteristic is related to the impurity concentrations of the solid and liquid at the growth interface. Consider an infinitely long cross -sectional area liquid. As the liquid solidifies from one end, the impurity concentration along the cooled solid $C_S(x)$ is given by

$$C_S(x) = C_0 k_0 \left(1 - x\right)^{k_0 - 1}, \tag{3.5}$$

where C_0 is the impurity concentration of the starting material, k_0 is the serration coefficient, and x is the fraction of the original melt that is cooled.[65] One can see that the segregation coefficient is the driving factor. If the concentration of impurities in the liquid at the solid-liquid interface during growth is greater than that of the solid, impurities will migrate towards the interface. As the interface moves across the melt, impurities are removed from the melt. Hence, the impurity concentration in the solid is greatest at the end piece of the crystal. The dynamics are reversed if the concentration of impurities of the solid at the solid-liquid interface is greater than that of the liquid.

3.2.2 Growth Techniques

Single crystal $Ga_2(Se_{1-x}Te_x)_3$ specimens for $0.5 \leq x \leq 1.0$ were grown using the Bridgman technique. In Bridgman growth, material is loaded into a crucible where it is then melted in a furnace and translated out of its melting zone to a cold zone to produce a single crystal. Not surprisingly, the choice of crucible material is crucial for successful growth experiments. The following criteria are:[65] (1) crucible used should not contaminate the crystal, (2) crucible should have a smaller coefficient of thermal expansion than the crystal to prevent sticking, (3) crucible should have a smaller thermal conductivity than the crystal to ensure good temperature distributions in melt, and (4) sharp corners should be avoided when fabricating the crucibles as such features create negative pressures in the melt (this is illustrated in Figure 3.5). For $Ga_2(Se_{1-x}Te_x)_3$ growth the crucible materials used included quartz, carbon, glassy carbon, and pyrolytic boron nitride (PBN). Experimental trials showed that quartz is the best option for $Ga_2(Se_{1-x}Te_x)_3$.

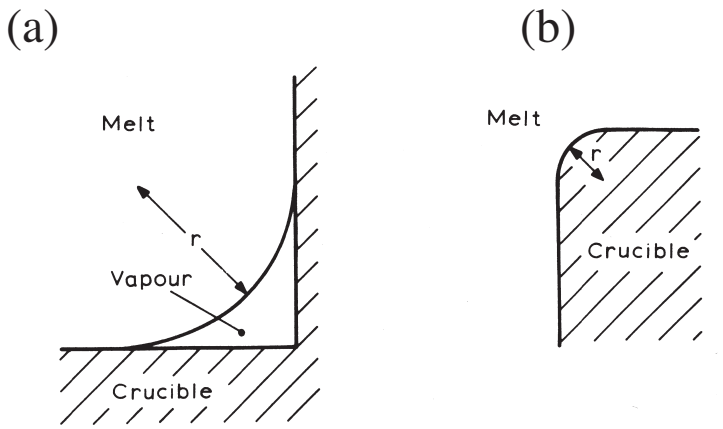

Figure 3.5: (a) and (b) show illustrations of sharp corners in crucible that give rise to added pressures during growth as reproduced from Brice.[65]

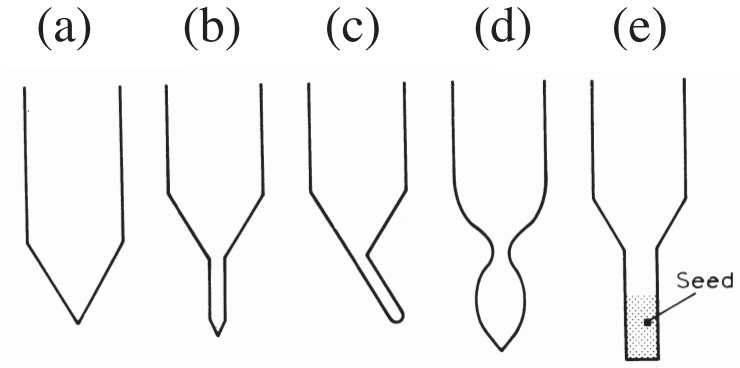

Figure 3.6: Crucible designs for Bridgman growth as reproduced from Brice. For instance, (c) may be used for materials require preferred growth directions.[65]

In Bridgman growth of conventional materials (e.g. Si, GaAs) a seed crystal is used that serves as the source of single crystal nucleation for the growth experiment. The Bridgman method used for $Ga_2(Se_{1-x}Te_x)_3$ growth relied on random nucleation. As the formation of one nucleus is more probable in small volumes, crucibles used in Bridgman growth have tapered tips (these are shown in Figure 3.6). For $Ga_2(Se_{1-x}Te_x)_3$, crucibles were fabricated such that the tapered tip forms a 90 ° angle. A schematic of the Bridgman growth process in shown in Figure 3.7. A sealed quartz crucible (10^{-6} Torr) loaded with synthesized $Ga_2(Se_{1-x}Te_x)_3$ 1.3 cm in diameter was placed in the ≈820 °C region of the furnace, where it was then translated at a rate of 0.2 mm/h through a temperature gradient of 10 °C/cm. Note that the growth process is the same for $Ga_2(Se_{1-x}Te_x)_3$ across all desired stoichiometries.

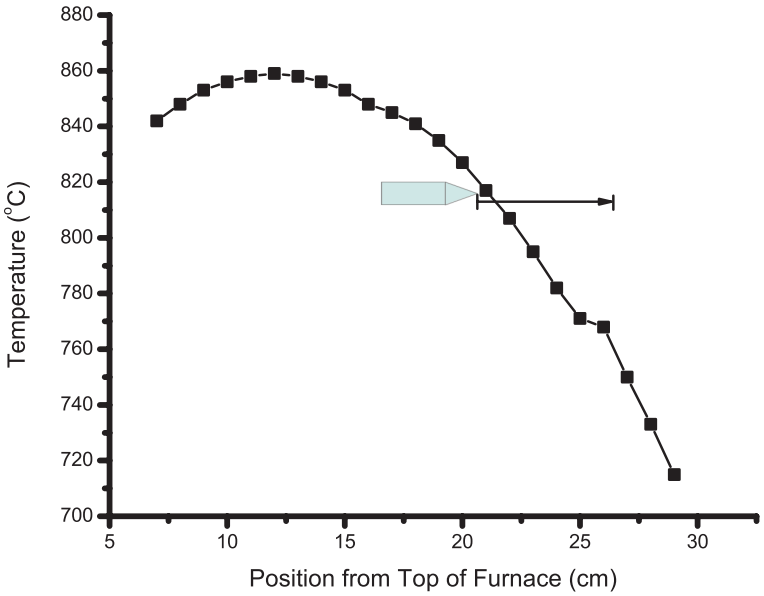

Figure 3.7: Schematic showing the temperature profile and crystal growth setup using a vertical Bridgman furnace.

3.2.3 Results

$Ga_2(Se_{1-x}Te_x)_3$ specimens of varying stoichiometries obtained from Bridgman growth are shown in Figure 3.8. Portions of the ingots extracted from the quartz crucible were still polycrystalline. Cleaving sections of the ingots revealed single crystalline facets that had a a metallic luster. Laue photographs (single crystal x-ray diffraction images) on these facets showed plane orthogonal to the surface of these facets is {111} type. The Laue pattern is shown in Figure 3.9, where the three-fold symmetry of the {111} is clearly evident. Thus, it appears that the natural cleavage planes for $Ga_2(Se_{1-x}Te_x)_3$ is of type {111}.

After the all single crystals are harvested they are cut and polished for further materials characterization. After a crystal is cut using a wire saw, it is lapped on 13 μm silicon carbide paper with ethanol to achieve a smooth surface. The polishing process then begins by first polishing the crystal using 3 μm silicon carbide paper with ethanol. The final stages of polishing involved using 1 μm then 0.5 μm alumina powders mixed with ethanol. The final polish was then done using 0.5 μm cerium oxide powder mixed with ethanol. A polished crystal is shown in Figure 3.8d.

The crystal quality of grown $Ga_2(Se_{1-x}Te_x)_3$ samples was examined with optical microscopy and scanning electron microscopy (SEM). Optical microscopy revealed expected surface defects (e.g scratches etc.) in addition to small black pits on the surface. An optical microscope image of a polished Ga_2SeTe_2 crystal at 100× magnification is shown in Figure 3.10a. To determine the elemental identity of these black pits, the sample was put in an SEM and electron energy loss spectroscopy (EDS) was conducted at one of the pits (Figure

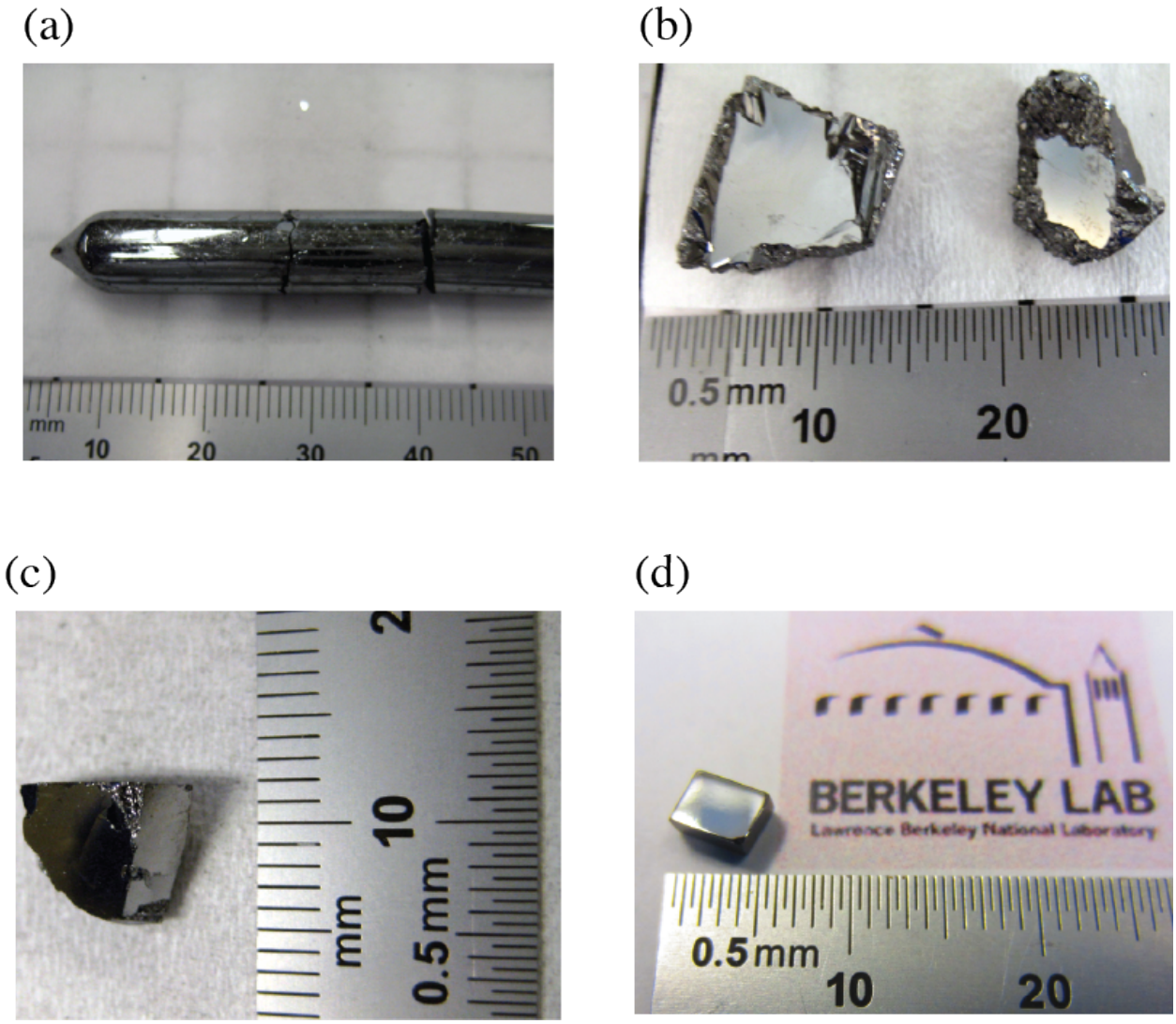

Figure 3.8: (a) Ga_2SeTe_2 ingot extracted from quartz crucible after vertical Bridgman growth, (b) Ga_2SeTe_2 single crystals, (c) $Ga_2Se_{0.6}Te_{2.4}$, and (d) polished and cut Ga_2SeTe_2 single crystal with dimensions 5 mm × 3 mm × 2 mm.

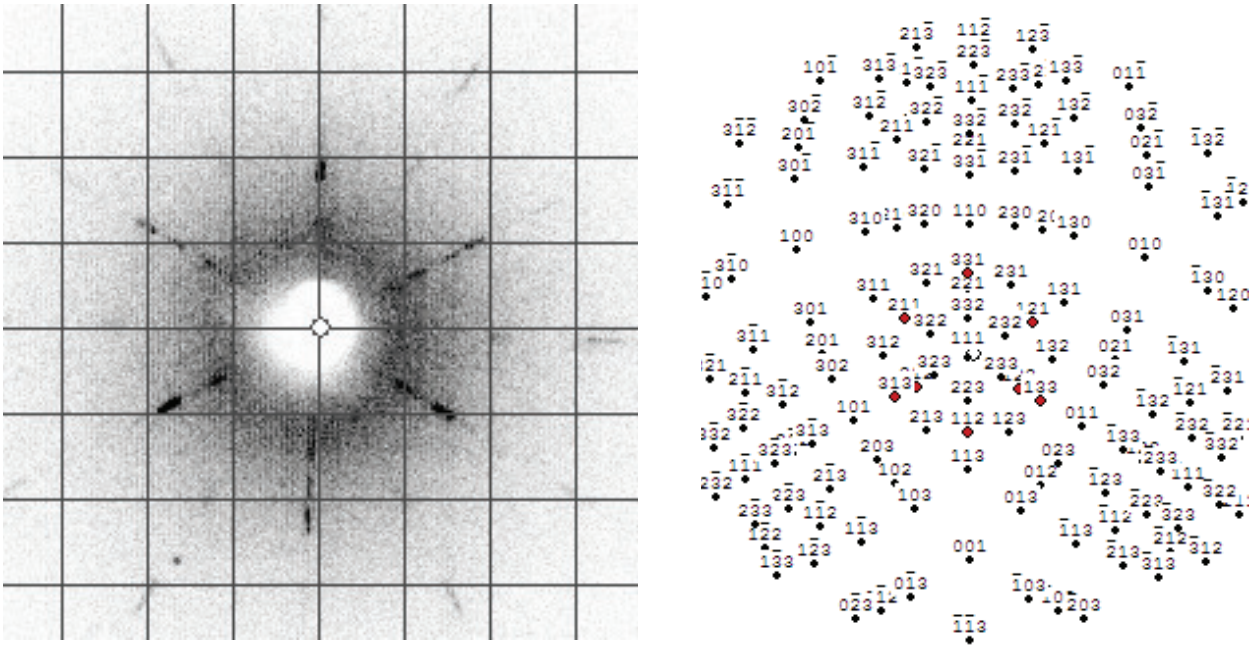

(a) (b)

Figure 3.9: (a) Laue photograph of a cleaved Ga_2SeTe_2 crystal showing a {111} type orthogonal plane and (b) corresponding stereographic projection.

3.10b). The EDS spectra reveal (Figure 3.10c) that the black features are likely Te precepts lodged in the Ga_2SeTe_2 surface. Additional lines corresponding to Al are caused by alumina residue on the crystal surface from polishing.

Glow discharge mass spectroscopy (GDMS) was implemented to investigate the impurity concentrations in a grown Ga_2SeTe_2 ingot. The dominant impurities in the material extracted from the top, middle, and bottom of the crucible are summarized in Table 3.1. A majority of the impurities increase in concentration as one moves towards the bottom of the crucible, implying a segregation coefficient greater than unity. Concentrations of Na, As, Br, and Ba decrease when going from top to bottom (segregation coefficient less than unity). Si (likely originating from the quartz crucible) is anomalous case since its concentration drastically increases at the bottom of the crucible. This feature may be indicative of the design of the crucible used; at the bottom a very thin necking was made hoping to minimize the propagation of multiple single crystal grains. However, this configuration results in a small amount of growth material surrounded by a larger fraction of quartz (compared with the top and bottom). The heavy metallic impurities (As, Zn, Fe, Bi, La, Ba, etc.) are most likely contaminants from the laboratory. Overall, it has been determined that the purity of the samples are satisfactory for carrying out basic research on the structure and properties of $Ga_2(Se_{1-x}Te_x)_3$.

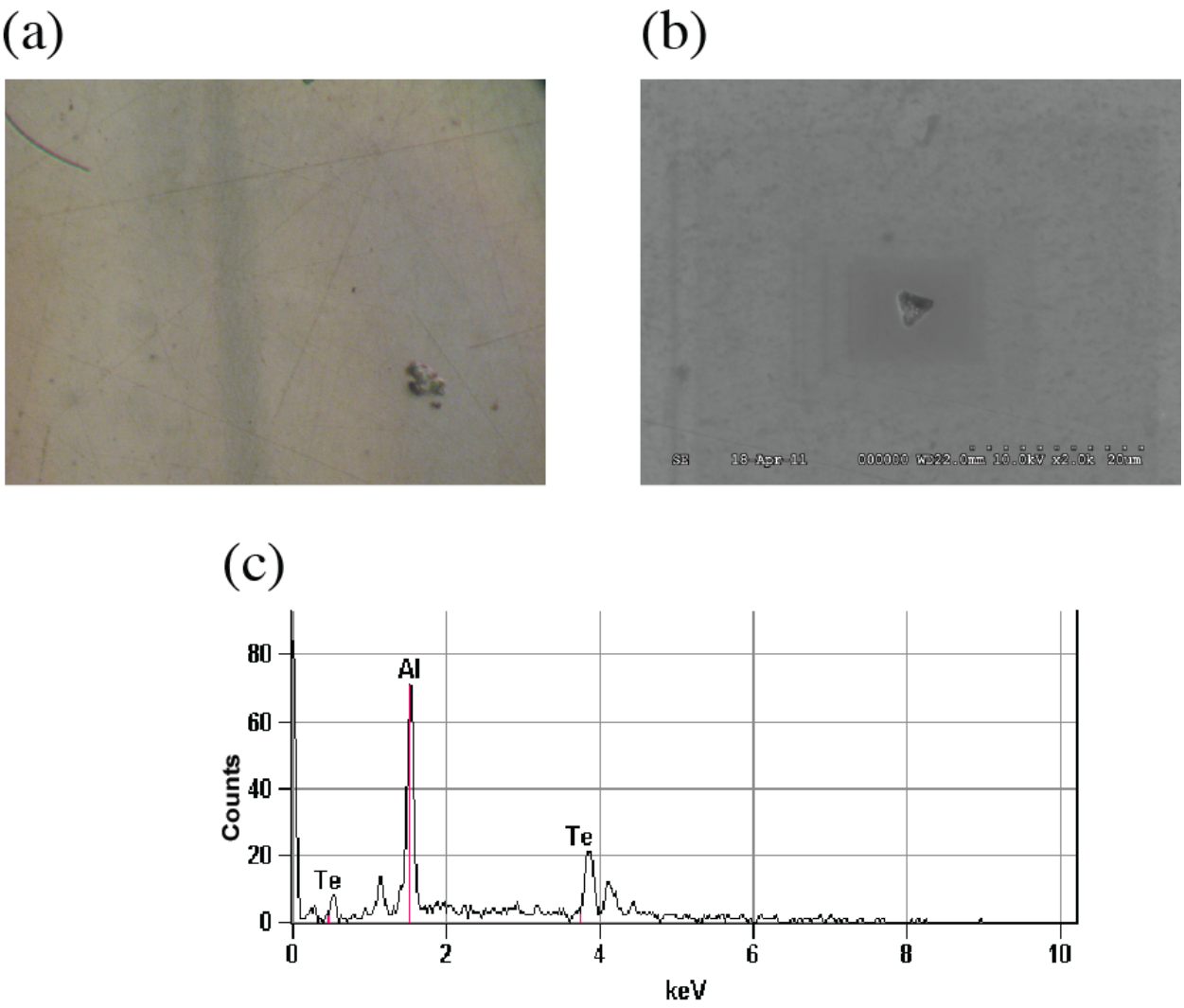

Figure 3.10: (a) Optical micrograph of polished Ga_2SeTe_2 crystal at 100× magnification, (b) SEM image of one black pit on the crystal surface, and (c) EDS spectra collected at the black pit feature.

Table 3.1: Impurity concentrations (in parts per million by weight) measured at the top, middle, and bottom part of grown Ga_2SeTe_2 ingot.

	TOP	MIDDLE	BOTTOM
Element	**Concentration [ppm]**	**Concentration [ppm]**	**Concentration [ppm]**
Na	1.1	0.86	0.62
Al	0.05	0.06	0.21
Si	1.4	1.9	3.8
P	0.59	0.62	0.53
S	2.0	1.9	2.6
Cl	0.32	0.41	0.9
Ca	0.39	0.13	0.37
Mn	0.6	0.64	0.75
Fe	0.73	0.77	0.91
Cu	0.26	0.29	0.57
Zn	0.47	0.5	0.63
As	0.9	0.78	0.66
Br	2.0	1.2	1.7
Ba	2.1	2.6	1.3
La	0.33	0.19	0.39
Bi	0.36	0.43	1.3

3.3 Conclusions

Single crystals of $Ga_2(Se_{1-x}Te_x)_3$, for $0.5 \leq x \leq 1.0$ were grown in a reproducible manner utilizing the Bridgman method. Grown crystals naturally cleaved along {111}. Optical microscopy and SEM revealed the presence of Te precipitates on the crystal surface. Mass spectroscopy on the top, middle, and bottom portions of the ingot revealed that most impurities (at ppm concentrations) tend to collect towards the bottom of the crystal (i.e. a segregation coefficient greater than unity). From a device physics standpoint the impurities at ppm concentrations would be a major hindrance, but for experiments probing the structure and physical properties $Ga_2(Se_{1-x}Te_x)_3$ it is sufficient.

Chapter 4

X-Ray Diffraction Studies

4.1 Introduction

In this section, the results and analysis of x-ray diffraction studies of $Ga_2(Se_{1-x}Te_x)_3$ are presented. An overview of diffraction theory is discussed first. Conventional and synchrotron powder x-ray diffraction on $Ga_2(Se_{1-x}Te_x)_3$ results are then shown. After this, high resolution single crystal diffraction experiments are described. Finally, diffraction experiments at high temperatures and pressures are presented. The majority of the diffraction work was done on $Ga_2(Se_{1-x}Te_x)_3$ with $x = 2/3$, or Ga_2SeTe_2.

4.1.1 Diffraction Theory

The concept of diffraction of x rays by crystalline solids dates back to the early twentieth century. At that time mineralogists suspected that the crystal structure of solids was composed of periodic atomic motifs on an Å length scale. Simultaneously, there were indications that x-ray radiation, recently discovered by Röntgen, may be electromagnetic waves with wavelengths on the order of 1 to 2 Å. Based on this knowledge, von Laue put forth the hypothesis that if x rays have wavelengths at the Å length scale and if crystals are constructed of periodic atomic units at the same length scale, then x rays should be diffracted by crystals. The hypothesis was experimentally verified in 1912 and the results became the fundamental basis of x-ray crystallography.[66] Shortly after, the father-son duo of Bragg expressed the results of von Laue in an elegant mathematical form and laid the out the necessary conditions for diffraction in any crystalline system.

X-ray diffraction in a crystal is a scattering process wherein constructive and destructive interference occur among many scattered incident x-ray waves. A crystal is constructed by a periodic structural motif known as the unit cell and the points where origins of the unit cell are located create a lattice.[67] The repeated physical units (i.e. atoms or molecules) located at the unit cell are called the basis. A crystal then is a lattice with a basis. Mathematically, crystal structure is a convolution of a lattice and a basis (as illustrated in Figure 4.1). It follows then that the symmetry of crystals can be described by symmetries of the lattice and basis, or space groups.

Consider a three-dimensional lattice defined by set of vectors $\mathbf{R_n}$ such that

$$\mathbf{R_n} = n_1\mathbf{a}_1 + n_2\mathbf{a}_2 + n_3\mathbf{a}_3, \tag{4.1}$$

where $\mathbf{a}_1$, $\mathbf{a}_2$, and $\mathbf{a}_3$ are lattice vectors, and n_1, n_2, and n_3 are integers. Suppose x rays (or any kind of radiation) incident on this lattice with wavevector $\mathbf{k}$ are elastically scattered with a resulting wavevector $\mathbf{k}'$. The scattering vector $\mathbf{Q} = \mathbf{k} - \mathbf{k}'$ measures the change between the incident and scattered wave. As they are elastically scattered, the magnitudes of the wavevectors are equivalent. Ideal diffraction occurs when complete destructive interference is produced in all directions except those of the diffracted waves, which undergo complete constructive interference. This means that the sum of phases must be 2π or multiples thereof. This phenomenon can be expressed as

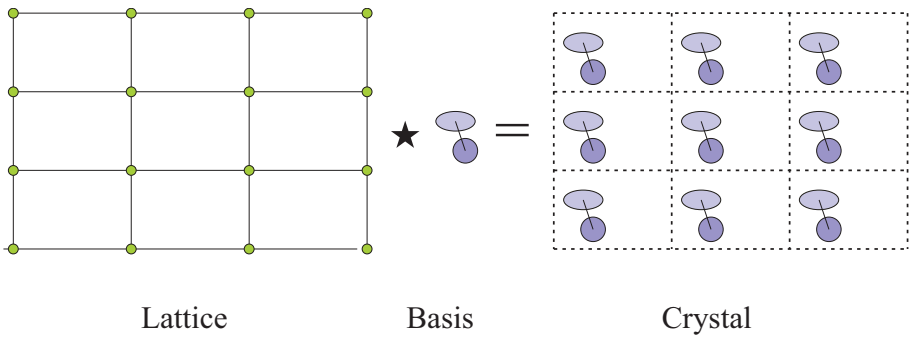

Figure 4.1: A two dimensional crystal constructed via the convolution of a lattice and basis as reproduced from Als-Nielsen and McMorrow.[67]

$$\mathbf{Q} \cdot \mathbf{R_n} = 2\pi \times \text{integer}. \tag{4.2}$$

To solve this expression, consider a lattice in wavevector space (with dimensions of reciprocal length) with basis vectors $\mathbf{a}_1^*$, $\mathbf{a}_2^*$, and $\mathbf{a}_3^*$ that satisfy the condition

$$\mathbf{a}_i \cdot \mathbf{a}_j^* = 2\pi\delta_{ij}, \tag{4.3}$$

where δ_{ij} is the Kronecker delta where $\delta_{ij} = 1$ and is zero otherwise. This then gives a reciprocal lattice $\mathbf{G}$ defined by a set of vectors such that

$$\mathbf{G} = h\mathbf{a}_1^* + k\mathbf{a}_2^* + l\mathbf{a}_3^*, \tag{4.4}$$

where h, k, and l are integers (also known as Miller indices). The reciprocal lattice satisfies the the condition set in equation (1.2), since $\mathbf{G} \cdot \mathbf{R_n} = 2\pi(hn_1 + kn_2 + ln_3)$ where the quantity in the parenthesis will always be an integer. Thus diffraction by a crystal will occur if the scattering vector of the incident radiation is a vector of the reciprocal lattice, or

$$\mathbf{Q} = \mathbf{k} - \mathbf{k}' = \mathbf{G}. \tag{4.5}$$

This is known as the Laue condition and is a powerful representation of diffraction phenomena. Examples of reciprocal lattice constructions are shown in Figure 4.2. The reciprocal lattice display two important characteristics: (1) A reciprocal lattice vector $\mathbf{G}_{hkl}$ is perpendicular to planes with Miller indices (hkl) and (2) the magnitude of a reciprocal lattice vector, $|\mathbf{G}_{hkl}|$, is $2\pi/d_{hkl}$, where d_{hkl} is the (hkl) plane spacing in the lattice. The latter can be easily derived via simple vector algebra. If equation (4.5) is rearranged and squared, the result would yield $\mathrm{G}^2 = \mathrm{Gk}\sin\theta$, or

$$n\lambda = 2d\sin\theta, \tag{4.6}$$

which is otherwise known as Bragg's law for diffraction, where n is an integer, λ is the wavelength of the radiation being diffracted, d is lattice plane spacing, and θ is the scattering

angle of the diffracted wave. The equivalence of Laue and Bragg representations of diffraction is illustrated in Figure 4.3. Note that while Bragg's law is admired for its simplicity, it does not address all diffraction phenomena (e.g. diffuse scattering at non-Bragg angles), hence the representation of diffraction in reciprocal space provides a more robust model.

Now consider an example of a one-dimensional lattice with a lattice spacing of a described by the function $\mathcal{L}(x)$. Let this lattice be composed of a series of infinitely sharp points such that,

$$\mathcal{L}(x) = \sum_n \delta(x - n\mathrm{a}), \tag{4.7}$$

where $\delta(x\text{-}n\mathrm{a})$ is the Dirac delta function. Since the reciprocal lattice vector $\mathbf{G}_{hkl}$ represents a family of {hkl} planes in real space, the relationship between the real space lattice and the reciprocal lattice can be deduced by considering the Fourier transform of $\mathcal{L}(x)$:[67]

$$\int_{-\infty}^{\infty} \mathcal{L}(x)\mathrm{e}^{i\mathrm{Q}x}\,\mathrm{d}x = \sum_n \int_{-\infty}^{\infty} \delta(x - n\mathrm{a})\mathrm{e}^{i\mathrm{Q}x}\,\mathrm{d}x = \mathrm{a}^* \sum_n \delta(Q - n\mathrm{a}^*) \tag{4.8}$$

As a result the Fourier transform of the one dimensional lattice with spacing a gives a reciprocal lattice with spacing $\mathrm{a}^* = 2\pi/\mathrm{a}$. This example can easily be expanded to higher dimensions. In then follows that reciprocal space is nothing more than the Fourier transform of real space.

4.1.2 X-Ray Sources

Standard x-ray tubes comprise the bulk of laboratory x-ray sources (illustrated in Figure 4.4). They consist of a filament and a metal target housed in a vacuum tube. Electrons from the filament impinge on the metal anode and inelastically scatter, where they scattered electrons release a spectrum of electromagnetic radiation. The energy of x-rays generated by this process have two components: a continuous bremsstrahlung component associated with electron deceleration and discrete peaks corresponding to fluorescent x-rays coming from the target. The latter arises by when an incident electron on the metal anode release an atomic electron. The electron vacancy is then filled from an outer shell electron and an x-ray of characteristic energy is released.

X-ray tubes are satisfactory for conventional most conventional crystallography work. However, higher x-ray fluxes may be required for weakly diffracting phenomenon or there may be a need for x-rays with finely tunable energies. In this case synchrotrons are utilized (Figure 4.5). Here, a source of electrons (usually made by boiling electrons off a cathode surface) is feed into a linear accelerator, where they are accelerated to a velocity near the speed of light. These electrons then circulate to booster ring, where their energy is further increased. The electrons are then injected to a storage ring where they circulate around the ring via bending magnets. These bending magnets cause the electrons to change their velocity vector and causes them to emit radiation (in this case x-rays). The emitted radiation can

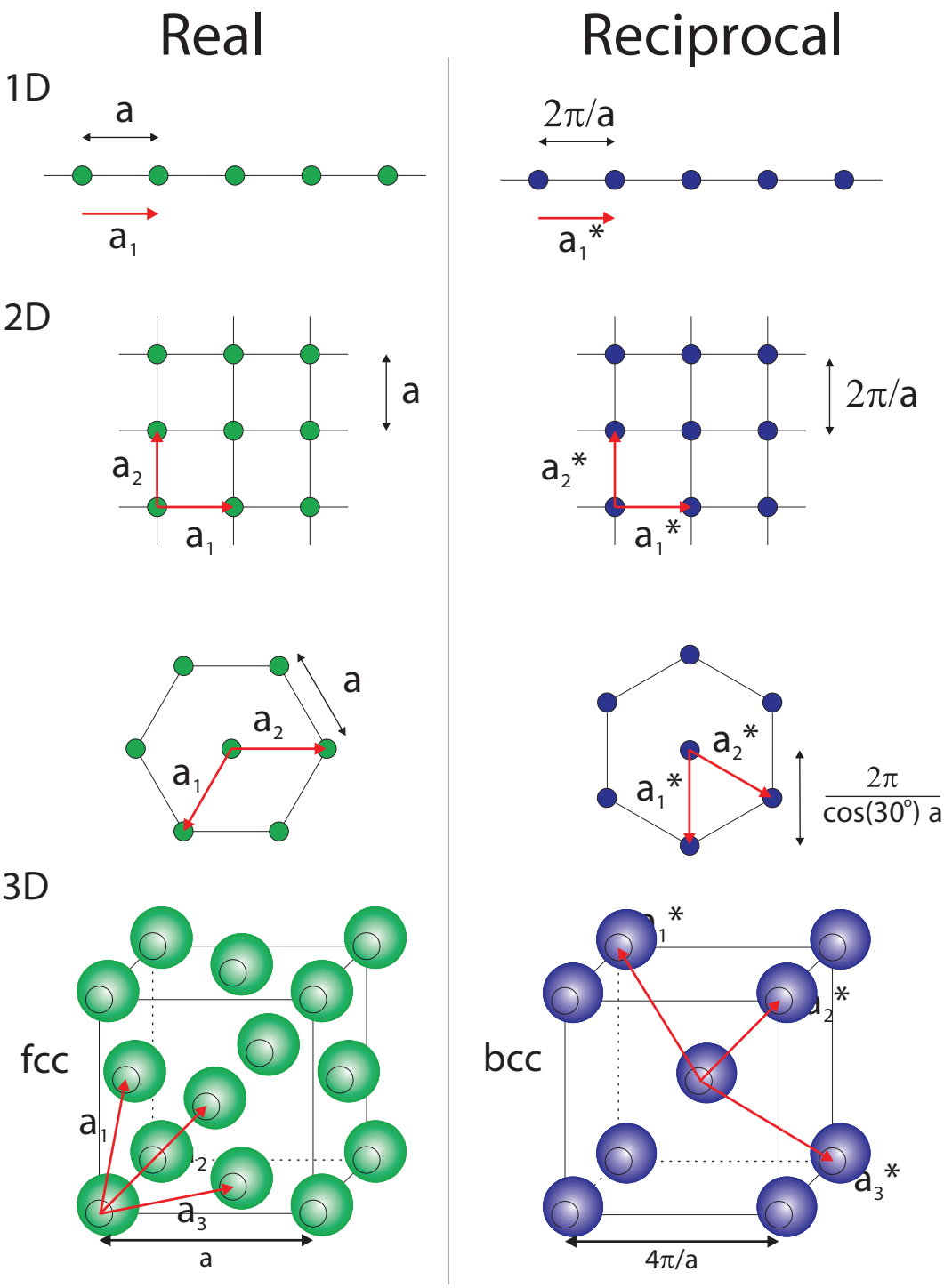

Figure 4.2: Examples of reciprocal lattice constructions in one, two, and three dimensions as reproduced from Als-Nielsen and McMorrow.[67]

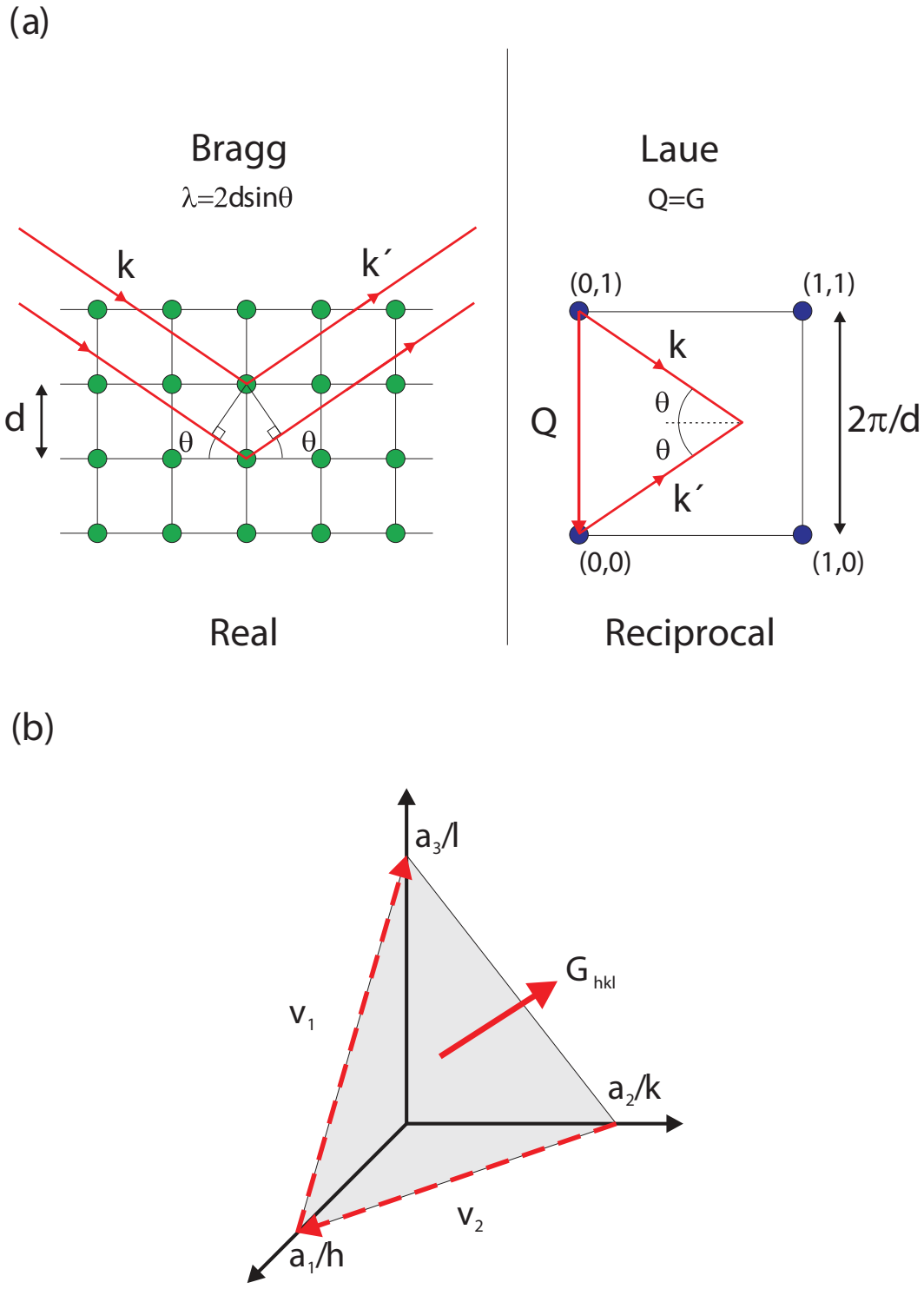

Figure 4.3: (a) Equivalence of Bragg and Laue diffraction representations and (b) relationship between reciprocal lattice vectors and Miller indices as reproduced from Als-Nielsen and McMorrow.[67]

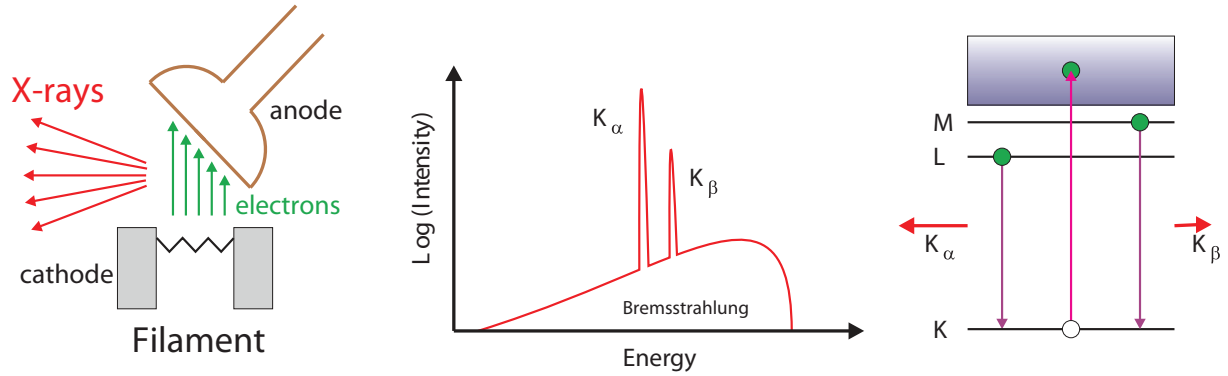

Figure 4.4: Schematic of an x-ray tube with the corresponding energy spectrum composed of a conitinous component from electron deceleration (i.e. bremsstrahlung) and discrete energy lines originating from fluorescent x-rays from the metal anode as reproduced from Als-Nielsen and McMorrow.[67]

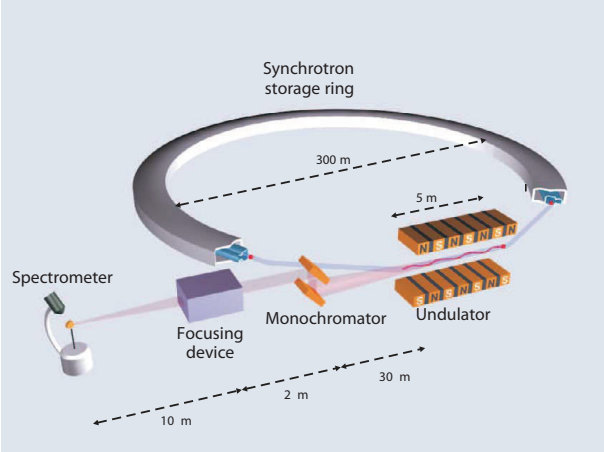

Figure 4.5: Representation of an x-ray beam line at a synchrotron facility as reproduced from Als-Nielsen and McMorrow.[67]

then be focused to many different experimental hutches. Insertion devices such as undulators and wigglers are employed that cause additional acceleration of electrons in the storage ring, which increases the available flux of emitted radiation. The flux of x-rays achieved by synchrotrons is eight orders of magnitude greater than that of the conventional x-ray tube. In the work carried for this dissertation, three synchrotron facilities were used: the Advanced Photon Source (APS) at Argonne National Laboratory, the Stanford Synchrotron Radiation Light Source (SSRL) at SLAC National Accelerator Laboratory, and the Advanced Light Source (ALS) at Lawrence Berkeley National Laboratory.

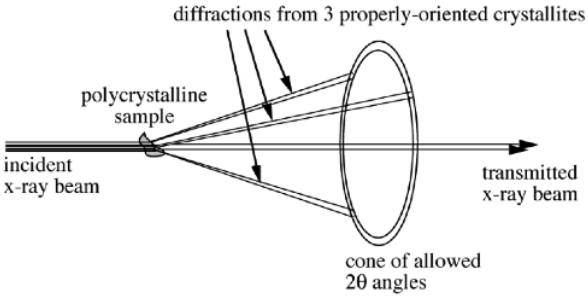

Figure 4.6: Representation of diffraction from a polycrystalline sample as reproduced from Fultz and Howe.[68]

4.2 Powder X-Ray Diffraction

Powder diffraction (also known as Debye-Scherrer) methods employ monochromatic x rays incident on a polycrystalline sample in a setup where the diffraction angle 2θ can be controlled. However, even when θ meets the Bragg condition, the majority of incident x-rays are at incorrect angles for diffraction. In a powder sample, all possible crystallographic planes are available for diffraction. Therefore, there would be some crystallites oriented correctly for successful Bragg diffraction. These crystallites diffract the incident x-rays into a set of diffraction cones that are collected by an x-ray detector (Figure 4.6). The resulting diffraction patterns appear as concentric rings, with the each ring corresponding to a cone of allowed 2θ angles. The two dimensional patterns are commonly plotted in one dimension intensity versus 2θ plots. In this section results from powder x-ray diffraction experiments on $Ga_2(Se_{1-x}Te_x)_3$ are presented.

4.2.1 Experimental Setup

Powder diffraction experiments on $Ga_2(Se_{1-x}Te_x)_3$ utilize conventional laboratory and synchrotron x-ray sources. In the laboratory, a Siemens D5000 x-ray diffractometer that utilizes a Cu x-ray tube operated at 40 kV and 30 mA was employed. Small ($\approx$ 0.5 mm to 1 mm) $Ga_2(Se_{1-x}Te_x)_3$ single crystals are ground to powders using an agate mortar and pestle. The powder sample is dispersed into a grooved plastic cube measuring 5 cm $\times$ 5 cm $\times$ 5 cm. The sample is loaded onto a four-circle goniometer and Cu K_α (8 keV, 1.5498 Å) x- rays (collimated via a double crystal four-bounce Ge monochromator) scatter off the sample. The diffracted x rays are collected by a scintillation counter.

A Nonius FR591 water-cooled rotating copper-anode x-ray generator was also used for powder diffraction measurements. Here, a powder sample is dispersed on plastic tape and the sample is sealed by overlaying a second piece of plastic tape. The sealed sample is attached to a nylon washer that is loaded into a computer controlled specimen holder. Cu K_α x-rays transmit through the sample and the diffracted x rays are collected by a MAR detector

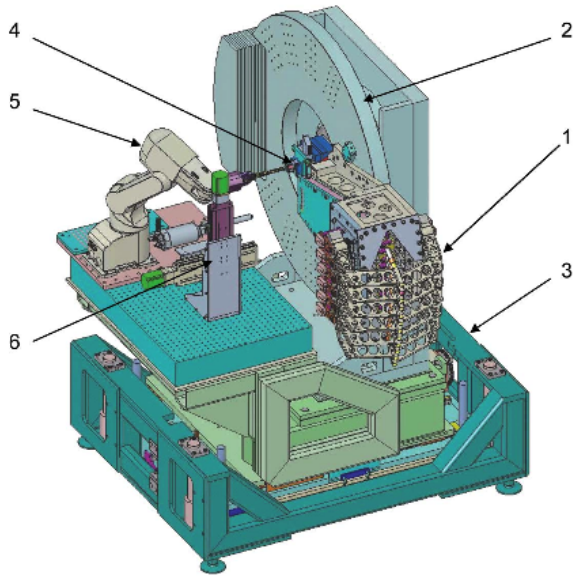

Figure 4.7: Model of the diffractometer utilized at the 11-BM at the APS.[70] (1) 12-analyzer detector system, (2) two-circle goniometer, (3) support table, (4) sample stage, (5) sample mounting robot, and (6) cryostream stages.

plate. The collected two dimensional ring powder diffraction patterns are integrated to one dimensional diffraction pattern using the Fit2D software.[69]

Synchrotron powder x-ray diffraction was carried out at the bending magnet beam line 11-BM at the APS. A focused beam of 30 keV (0.41328 Å) x rays and a two-circle diffractometer consisting of 12 independent Si (111) crystal analyzers is used. $LaCl_3$ scintillation detectors are used to collect the diffraction. The x-ray beam is aligned such that it is parallel to the rotating surface of the two-circle diffractometer and passes through its center of rotation, the slit box, and onto the crystal analyzers. A detailed description of the instrumentation at the 11-BM beam line was reported by Lee et al.[70] Powders were loaded into Kapton capillaries measuring 0.80 mm in diameter. The tubes were sealed with clay at the top and are then mounted onto the beam line using a robotic sample loader. A schematic of the beam line is shown in Figure 4.7.

4.2.2 Results and Discussion

An initial powder diffraction pattern for Ga_2SeTe_2 is shown in Figure 4.8. The Bragg reflections observed matched to a cubic zincblende structure previously reported in the International Center for Diffraction Data (ICDD) powder diffraction file (PDF). However, a weak satellite reflection close to the 111 Bragg line (arrowed in Figure 4.8), was noted that could not be index to a specific structure. At this point, this feature in the diffraction pattern was believed to be some extrinsic impurity in the sample and was initially ignored. To readily

confirm the cubic structure, the diffraction pattern was simulated using the FullProf software and was matched to the experimental data.[71] The results are shown in Figure 4.9. Here, the only theoretical pattern that converged to the experimental data was that of the cubic zincblende structure. Hence, it is concluded that Ga_2SeTe_2 takes a zincblende structure, with a computed lattice constant of 5.8 Å and a density of 5.3 g/cm^3.

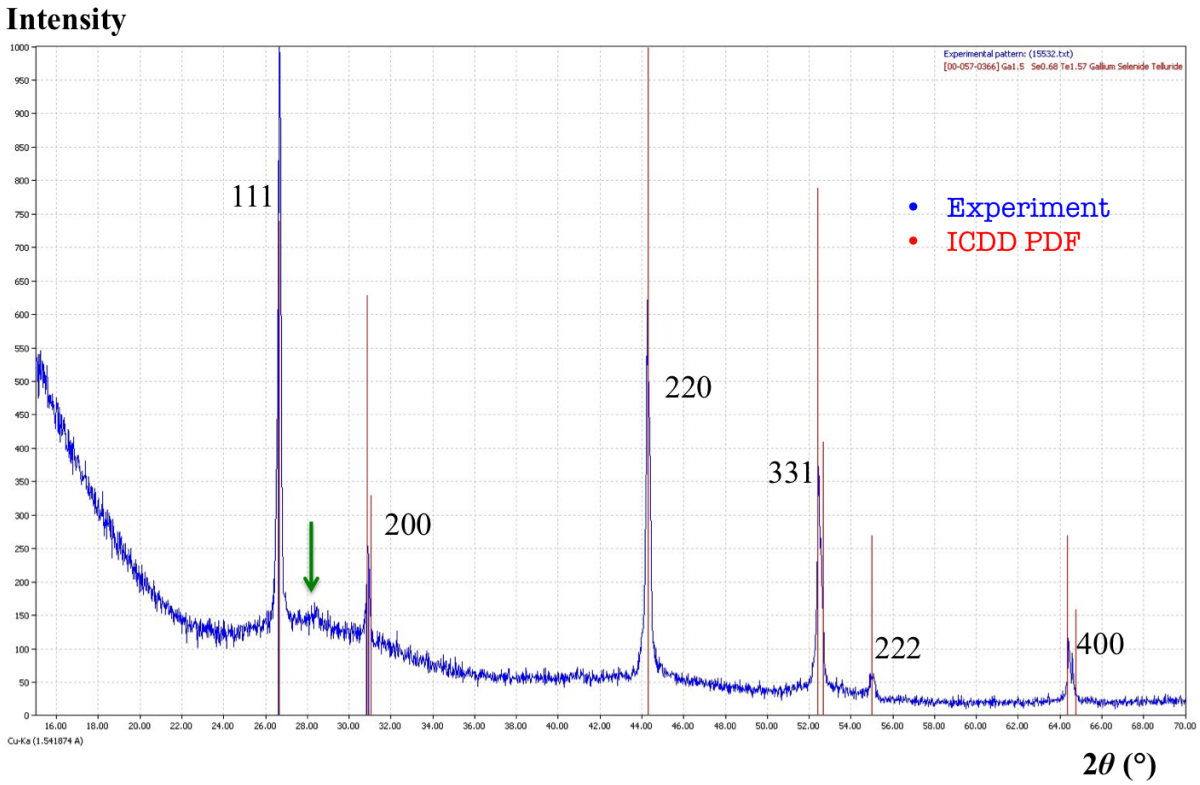

Figure 4.8: Powder pattern of Ga_2SeTe_2 showing a zincblende cubic structure when compared with the ICDD PDF. Features around the 111 reflection (arrowed), were also observed.

Additionally, diffraction patterns of $Ga_2(Se_{1-x}Te_x)_3$ with varying tellurium concentrations were collected. The results confirmed the behavior observed by Warren et al,[61] in which compounds with tellurium concentrations $x \leq 0.5$ showed multiple phases. This is illustrated in the diffraction pattern for Ga_2Se_2Te (i.e. $x = 1/3$) shown in Figure 4.10. Here multiple phases of Ga-Se compounds are observed and no clear structure is prevalent. As a result, the research carried out in this dissertation maintained tellurium stoichiometries of $x \geq 0.5$, where $Ga_2(Se_{1-x}Te_x)_3$ compounds in this range maintained the cubic zincblende structure, and for which the lattice constant decreases with increasing selenium atom fractions. For matters of consistency, the bulk of the structural work was carried out on Ga_2SeTe_2 ($x = 1/3$).

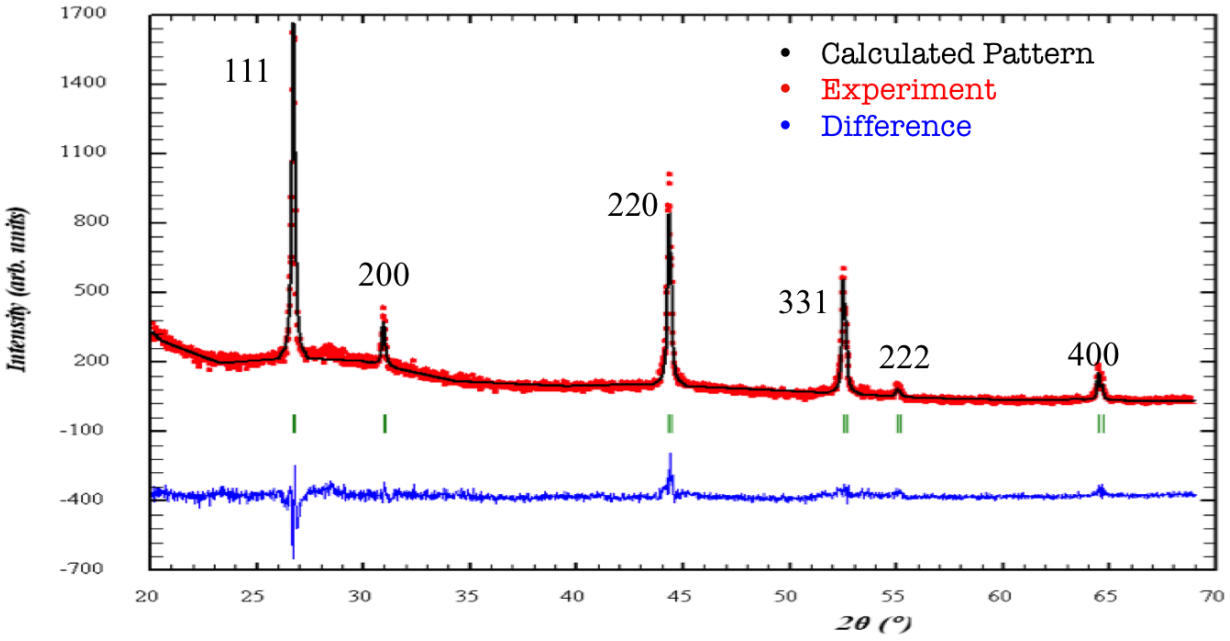

Figure 4.9: Refined diffraction pattern of Ga_2SeTe_2, showing the simulated cubic pattern (black line) converges to the experimental data (red).

Upon further examination, it is believed that the satellite feature around the 111 Bragg line in Figure 4.8 is structural in nature and not associated with an impurity. As there must be structural vacancies to maintain charge neutrality in the zincblende structure, the vacancies should have an impact on x-ray scattering power, though not as strong as the constituent atoms. To observe the satellites more clearly, Ga_2SeTe_2 powders patterns were collected at the APS at beam line 11-BM. The results are shown in Figure 4.11. The high-resolution pattern refined to the zincblende structure with a lattice constant of 5.77 Å. The inset of Figure 3 highlights the presence of satellite peaks around the 111 Bragg line not associated with crystal lattice reflections. Examining the two pairs of satellite peaks, the intensities of the peaks on opposites sides of the 111 Bragg line are not commensurate with each other. This appears to be an indication of short range ordering of the structural vacancies in Ga_2SeTe_2 and hints that ordering dynamics in this material may be manipulated.

As was discussed in Chapter 2, structural studies on Ga_2Te_3 revealed that structural vacancies manifest themselves as two dimensional structures by Kim et al.[37] This was confirmed through electron microscopy and diffraction investigations where satellite reflections around the 111 Bragg lines corresponded to two-dimensional vacancy structures. Moreover, vacancy ordering has been shown to occur in Ga_2Te_3 through annealing treatments. It was seen that annealing Ga_2Te_3 powders close to melting temperature and quenching to 0 °C caused complete vacancy ordering and annealing at lower temperatures and slowly cooling caused further disorder. With this in mind, similar annealing treatments were subjected to

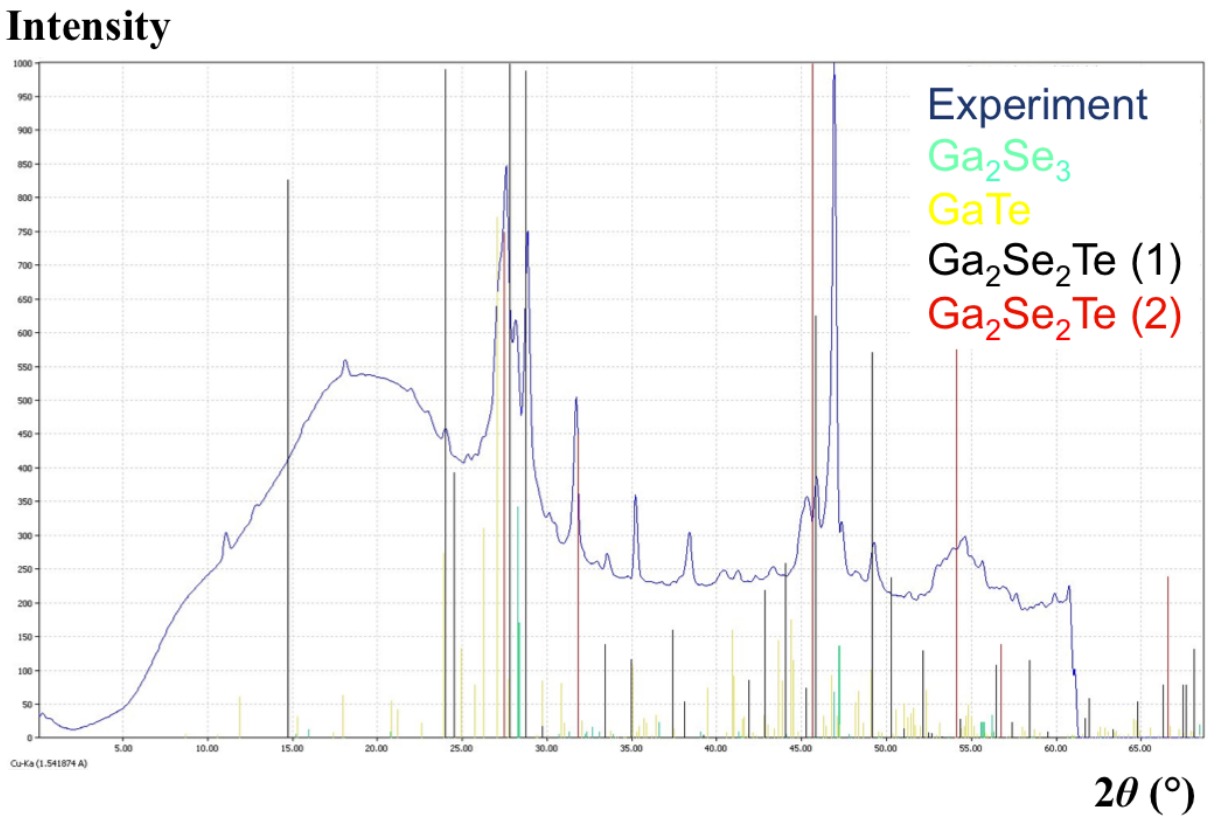

Figure 4.10: Ga_2Se_2Te showing a multitude of phases predicted by the ICDD PDF database. The broad feature at low 2θ values originates from the plastic tape on which the powder sample is dispersed.

Ga_2SeTe_2 powders to observe this effect. Samples were annealed 735 °C for 14 days then quenched to 0 °C and 435 °C for 14 days followed by slow cooling. The resulting powder diffraction patterns (focused around the 111 Bragg reflection) collected at the 11-BM beam line are shown in Figure 4.12. Similar to the as-grown compound, the annealed specimens conformed to a cubic zincblende structure with a lattice constant of 5.77 $\AA$. However, the distribution of the structural vacancies is is altered with thermal history evinced by the contrasting intensities of the satellite reflections around the 111 Bragg peak. Examining the 735 °C powder, the most prominent satellite reflection pair (labeled a in Fig. 4.12) occurs at at $\Delta(2\theta)$=0.45 °C (Δq=0.12 $\AA^{-1}$). Closer to the Bragg peak another satellite reflection pair (labeled b in Figure 4.12) is observed at $\Delta(2\theta)$=0.20 °C (Δq=0.05 $\AA^{-1}$). In both instances, this indicates the formation of modulated two-dimensional vacancy structures upon high temperature annealing followed by quenching. The diffraction space for the as-grown and 435 °C annealed samples shows broadened satellite reflections around the 111 Bragg line, indicating that the two-dimensional vacancy structures parallel to the <111> directions are

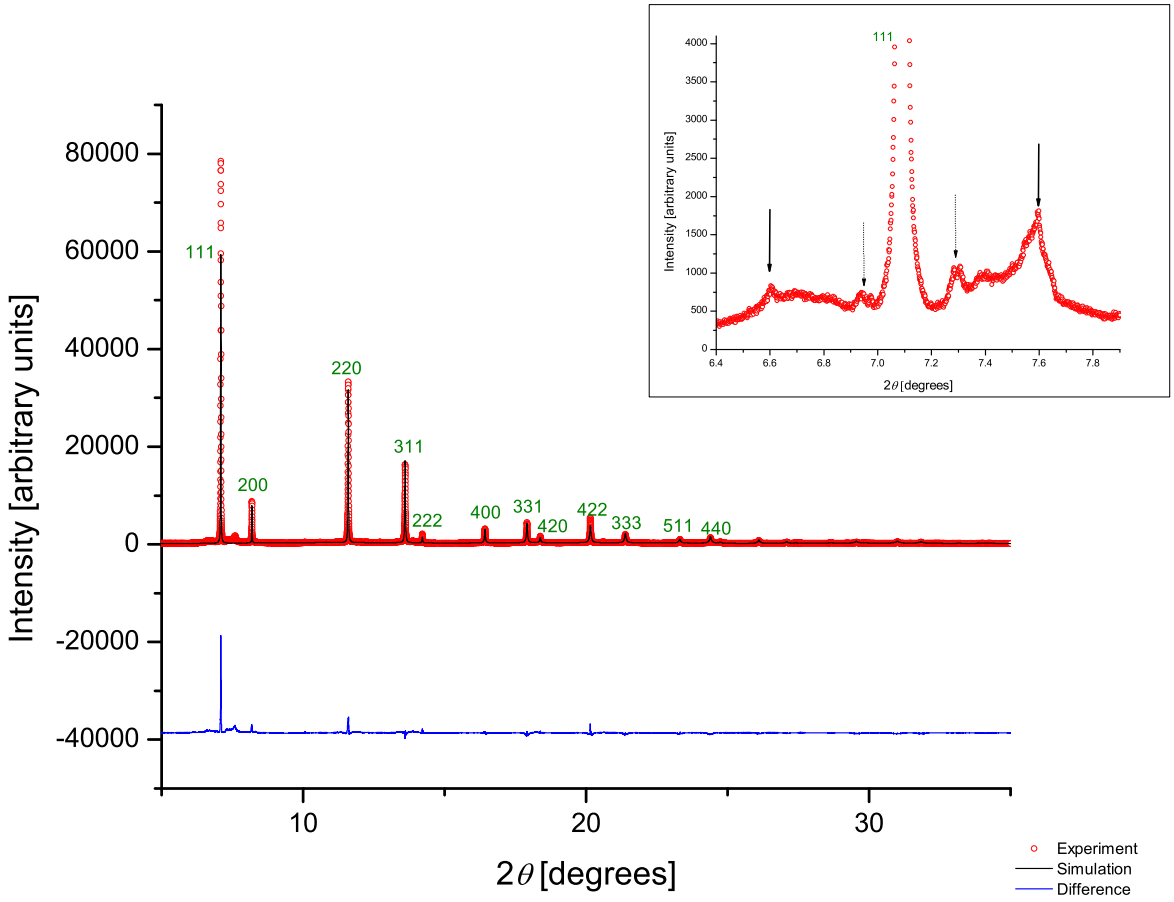

Figure 4.11: High resolution diffraction pattern of Ga_2SeTe_2 collected at the APS 11-BM beam line. The red points represent the experimental data, the black line represents the simulated pattern, the blue line represents the error between experiment and calculation, and the green represents all possible Bragg reflections for a zincblende lattice. The inset shows two prominent pairs of satellite peaks (arrowed) around the 111 Bragg line.

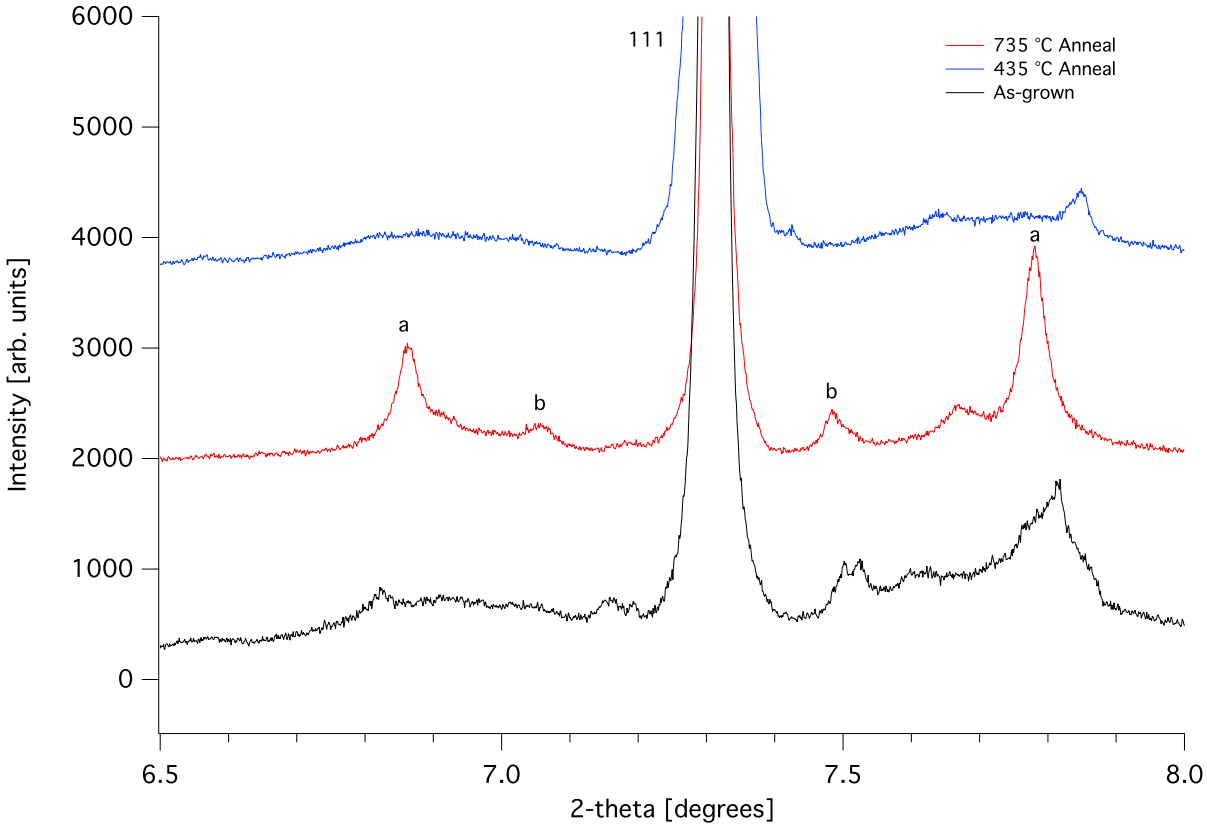

Figure 4.12: Diffraction patterns of as-grown (black), 735 °C (red) annealed, and 435 °C annealed Ga_2SeTe_2 powders collected at the APS. Annealing at 735 °C and quenching to 0 °C produces sharp satellite peaks around the 111 Bragg reflection (labelled a and b) attributed to two-dimensional vacancy structures parallel to the <111> directions. The satellites are still present in the as-gown and 435 °C specimens, but are diffuse, suggesting the two dimensional vacancies are still present but adopt a disordered modality.

present in the as-grown and 735 °C specimens, but they loose their periodicity. These results show that temperature is a pivotal driving factor for vacancy ordering in Ga_2SeTe_2.

4.3 Single Crystal X-Ray Diffraction

To examine the effect of thermal annealing on the structure of Ga_2SeTe_2 in more detail requires high-resolution reciprocal space mapping of all observed Bragg reflections; this can be performed via single crystal diffraction. Here, a bulk single crystal is used as the diffracting medium and the orientation of one of its facets must be precisely known. Recall from Chapter 3, that Laue photographs of Ga_2SeTe_2 show a preferred (111) orientation. Hence, in single crystal diffraction experiments a four-circle diffractometer (depicted in Figure 4.13) is used to drive the crystal in reciprocal space. In this geometry, the available degrees of freedom include: (1) the χ axis that passes through crystals and lies in the diffraction plane (2) the ϕ axis corresponding to rotation of the goniometer to which the crystal is attached (3) the Ω axis, which passes through the crystal and is perpendicular to the diffraction plane, and (4) the detector angle 2θ. In this section, results from single crystal diffraction experiments on annealed and as-grown Ga_2SeTe_2 single crystals are presented.

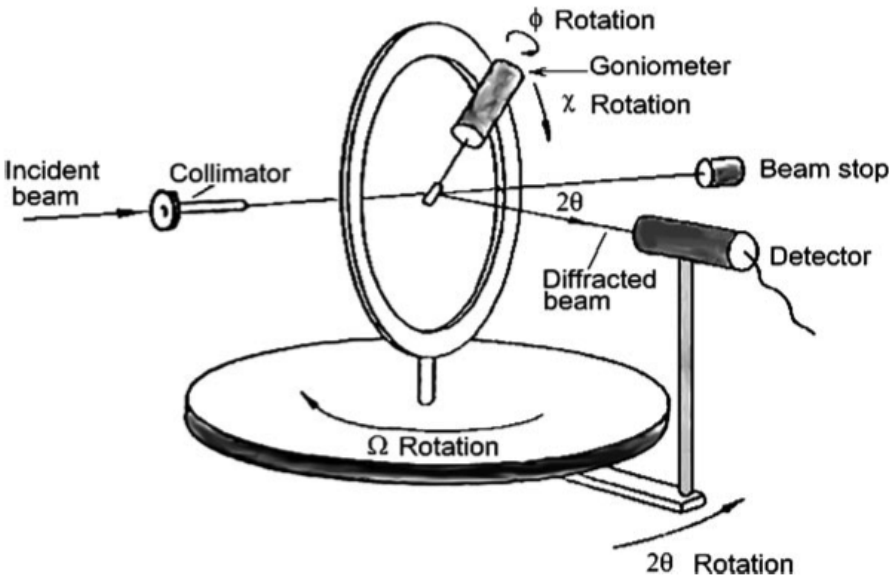

Figure 4.13: Representation of a diffractometer with four-circle geometry as reproduced from Sirdeshmukh.[72]

4.3.1 Experimental Setup

Single crystal diffraction measurements were carried out at the APS (33-BM beam line) and at SSRL (beam line 7-2). X-rays are tuned using a Si (111) double-crystal monochromator that allows for x-ray tuning from energies of 5 to 38 keV (APS 33-BM) and 4.6 to 16.5 keV (SSRL). Details on instrumental setups can be found elsewhere.[73] A focused beam of 15 keV x rays was used in the single crystal diffraction experiments. Single crystal Ga_2SeTe_2 specimens were mounted on a four-circle diffractometer utilizing a scintillation area detector (APS) and scintillation counter (SSRL) for data collection (Figure 4.14). The reflection setup used an off-specular geometry. Single crystalline specimens were subjected to three thermal treatments: (1) 735 °C anneal followed by quenching to 0 °C, (2) 435 °C for 28 days with the furnace then shut down and the crystal slowly cooled, (3) sample in the as-grown state. Single crystals used had approximated dimensions of 3 mm × 3 mm × 1 mm. The natural (111) facets of the single crystals were used, where no additional polishing was necessary. The crystals were lapped at their non-faceted sides so that they could be mounted flat on the goniometer. This was done using double-sided tape (at the APS) or a vacuum chuck (at SSRL). Reciprocal lattice scans were taken by driving the computer controlled goniometer motors (via the SPEC software package) to allowed Bragg reflections that are specular to the known 111 reflection. Each reciprocal space scan had a data collection time of ≈30 m.

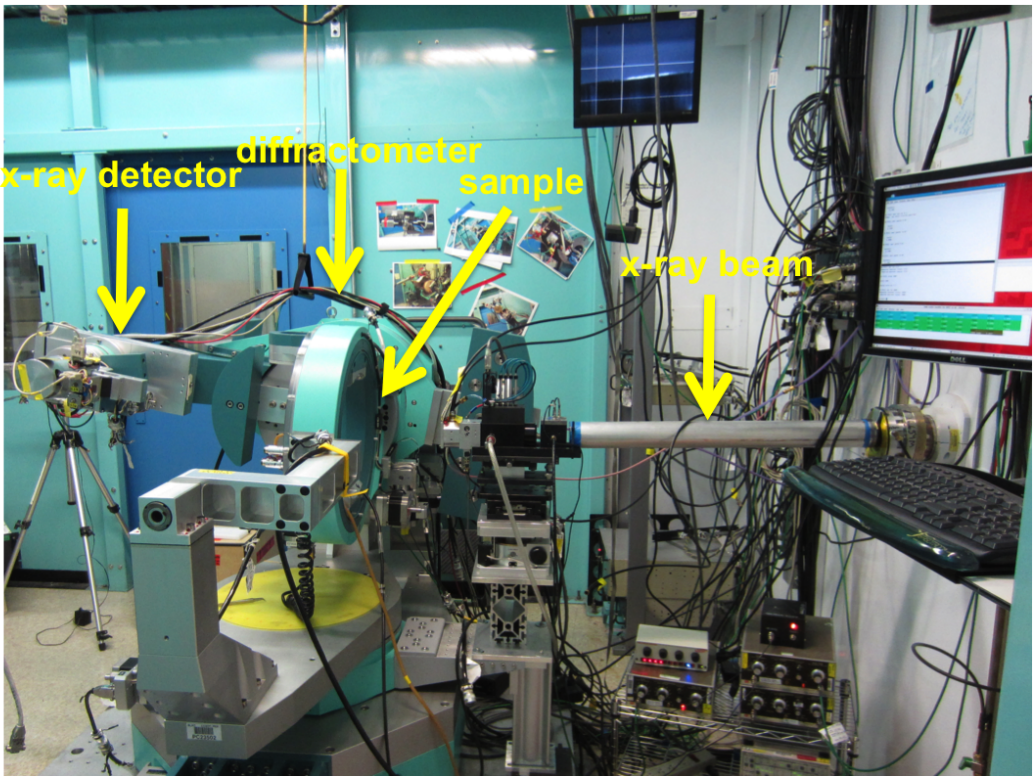

Figure 4.14: Single crystal diffraction experimental setup at SSRL, beam line 7-2.

4.3.2 Results and Discussion

Results from single crystal diffraction experiments on Ga_2SeTe_2 single crystals are shown as two-dimensional *h*-*k* contour maps (Figures 4.15-4.20) for a variety of Bragg reflections. On each contour map, the reciprocal space for an as-grown, 435 °C, and 735 °C specimens is shown. In a similar manner to the powder diffraction results, going from the as-grown to the annealed conditions, satellite reflections begin to develop around the main Bragg peaks. One common feature across all specimens is the varying degree of elongation across the *h*-*k* direction.This suggests the presence of structural vacancies produces strain the zincblende lattice, but leaves its overall symmetry intact. Yet the presence of vacancy structures may distort the local environment around the Ga, Se, and Te atom sites in Ga_2SeTe_2.

Inspecting the 111, 004, 222, 333, 331, and 226 *h*-*k* contour maps of 735 °C annealed crystal (Figure 4.15 and 4.16), four satellite reflections are observed at 1/16[1,2] and 1/16[2,1] around the main Bragg peak. Satellite pairs around 1/16[2,3] and 1/16[3,2] in *h*-*k* space are also observed in the 111, 222, and 333 Bragg reflections. At the 004, 331, 113, 264, and 226 Bragg peaks, pairs of satellites occur at 1/8[1,0] and 1/8[0,1] around the main Bragg reflections in *h*-*k* space, pointing to structural modulations. Note that across certain Bragg reflections crystal twinning was observed via the observation of split diffraction peaks, most notably at 004, 113, and 264. In other cases, satellite peak pairs had incommensurate intensities, 113, 220, and 331 being the notable examples. This does not appear to be a physical effect, but rather one that results from the detector-sample geometry. For instance, the intensities of satellite pairs at the 111 contour map are all commensurate, so it would follow that 333 should show the same behavior. However, higher order reflections requires more specimen tilting that would push the boundary for the collection efficiency of diffracted x-rays. Fundamentally, the 735 °C annealing treatment leads to an extremely rich reciprocal space arising from modulated (most likely vacancy based) superstructures embedded in the cubic zincblende lattice.

The single crystal data show diffraction behavior resulting from superstructures that is not only limited to the 111 Bragg reflection, but also spans across all allowable reflections for a zincblende lattice. As was discussed in Chapter 2, two-dimensional vacancy structures for Ga_2Te_3 parallel to <111> directions were observed. The single crystal diffraction data appear to indicate that additional vacancy structures oriented on different directions may be present. Another possible explanation is that satellite reflections at higher order reflections can be second order harmonics of x rays diffracted by the {111} type vacancy structures. To resolve this question, one simply needs to image the structure at the atomic level (this will be shown in Chapter 6).

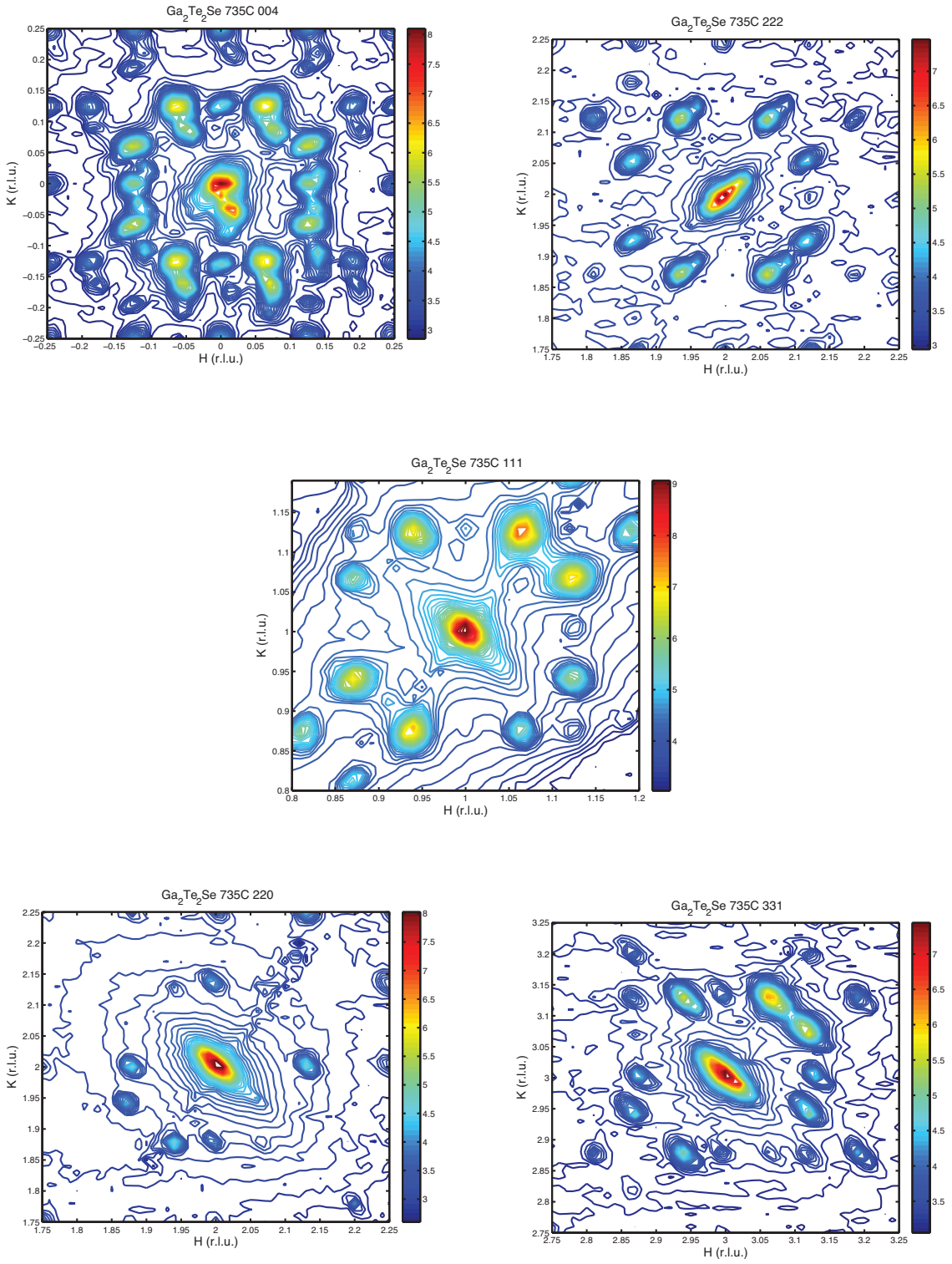

Figure 4.15: Two-dimensional reciprocal lattice contour maps of 735 °C annealed Ga_2SeTe_2 crystal at the 004, 222, 111, 220, and 331 Bragg reflections.

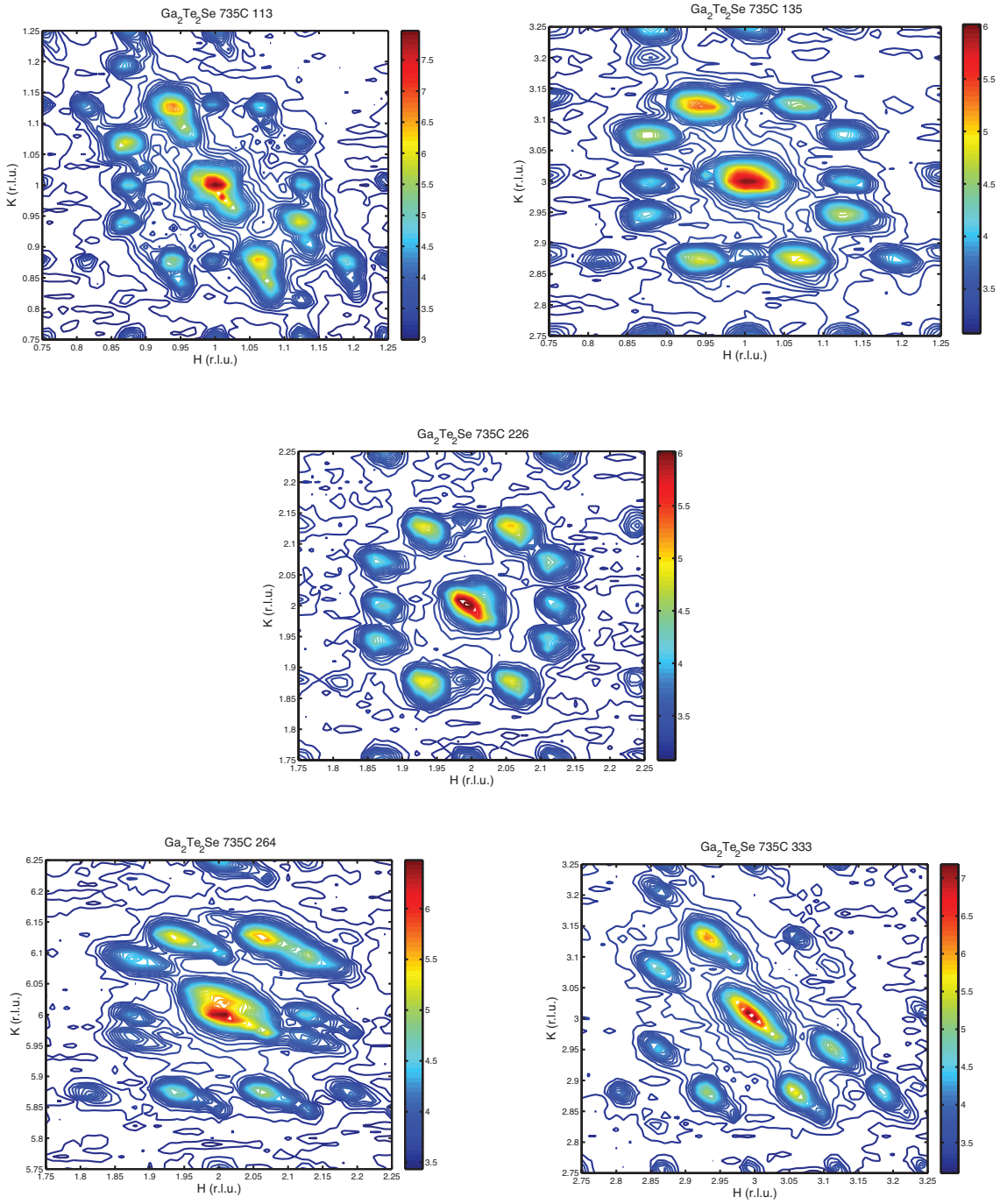

Figure 4.16: Two-dimensional reciprocal lattice contour maps of 735 °C annealed Ga_2SeTe_2 crystal at the 113, 135, 226, 264, and 333 Bragg reflections.

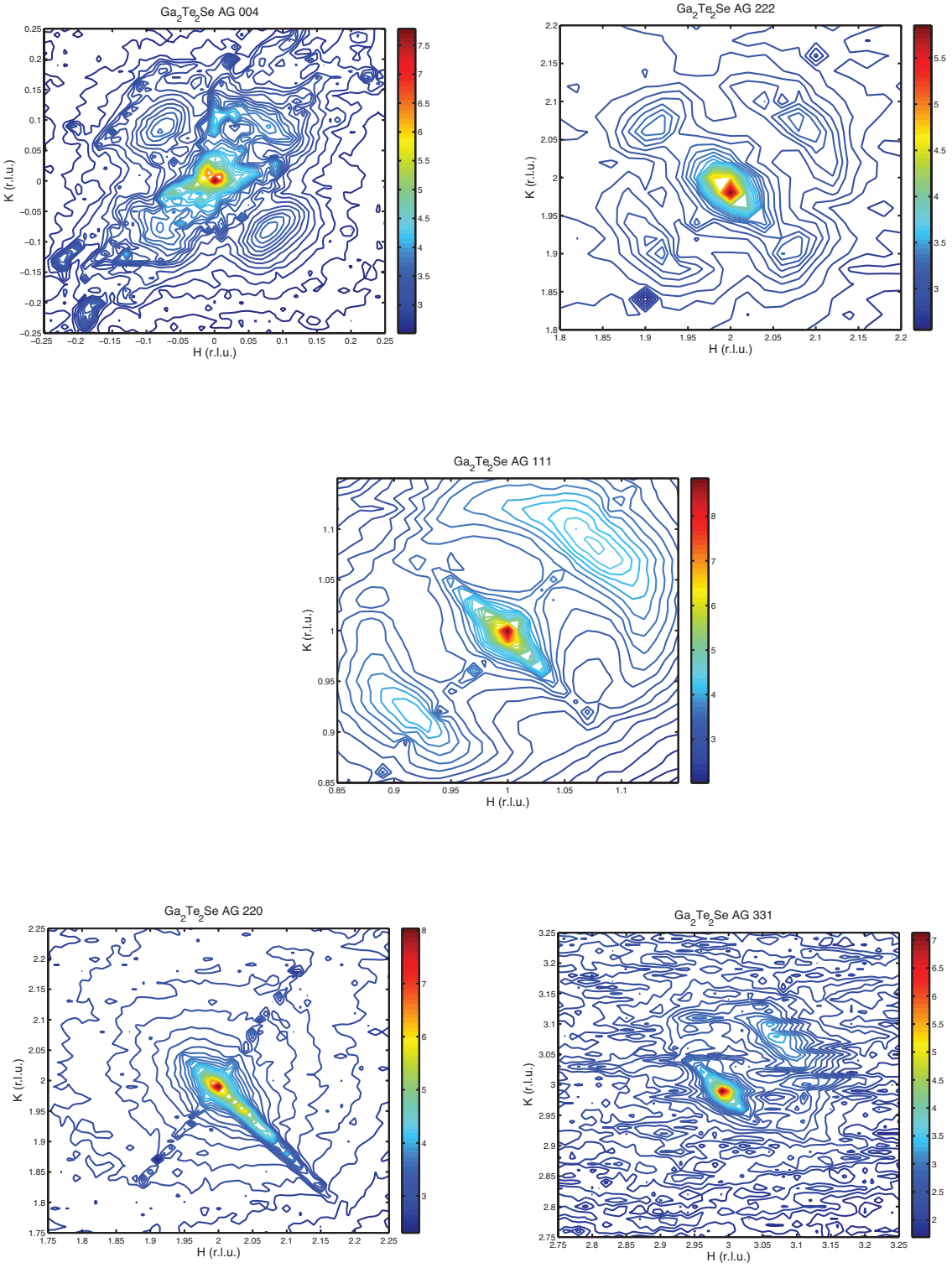

Figure 4.17: Two-dimensional reciprocal lattice contour maps of as-grown Ga_2SeTe_2 crystal at the 004, 222, 111, 220, and 331 Bragg reflections.

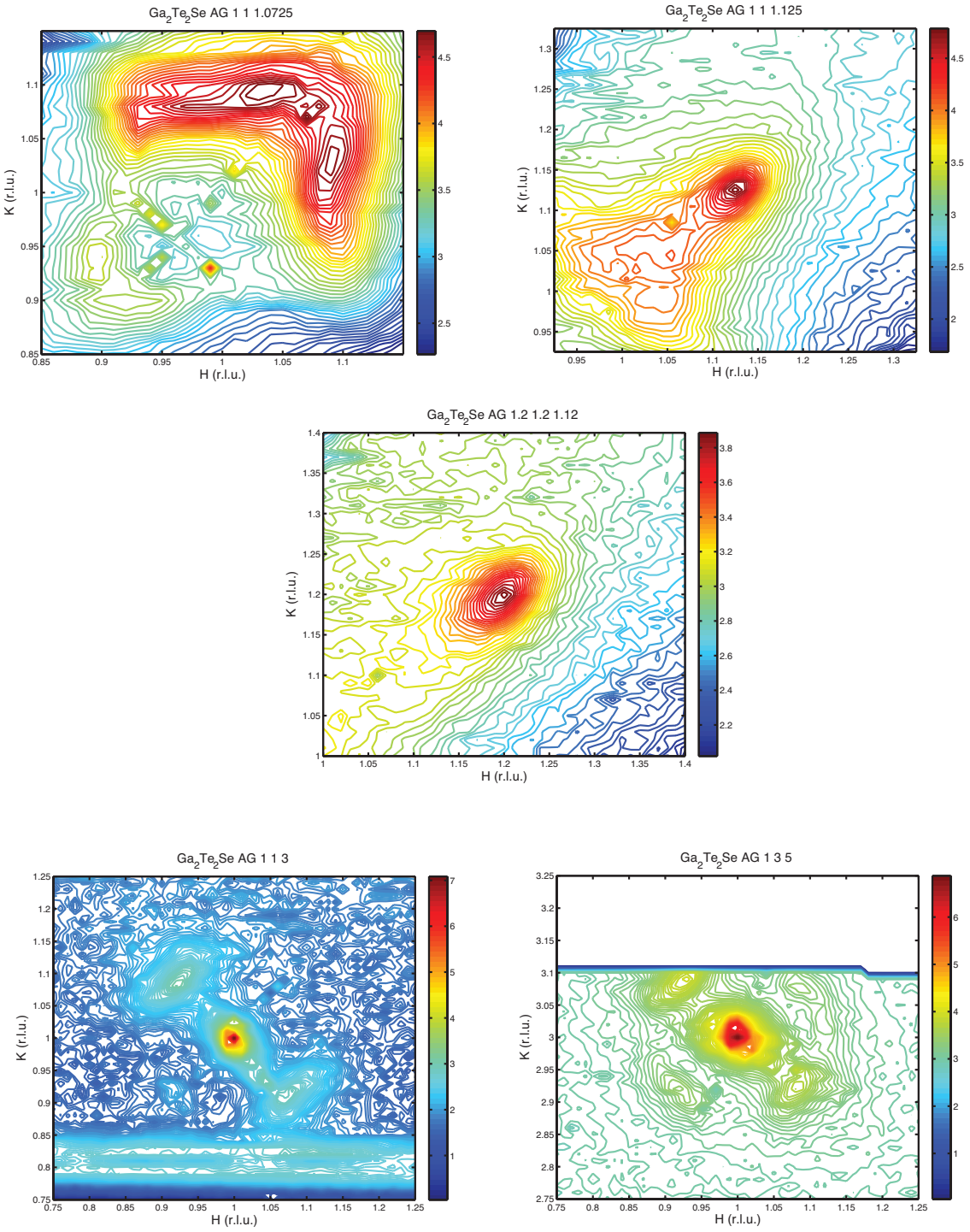

Figure 4.18: Two-dimensional reciprocal lattice contour maps of as-grown Ga_2SeTe_2 crystal where the top three maps show the reciprocal space around 111 where diffuse x-ray scattering is observed. The bottom two are maps at the 113 and 135 Bragg reflections. During data collection at the APS, the beam went down, but the collected reflections still provide a good representation of the diffraction phenomena.

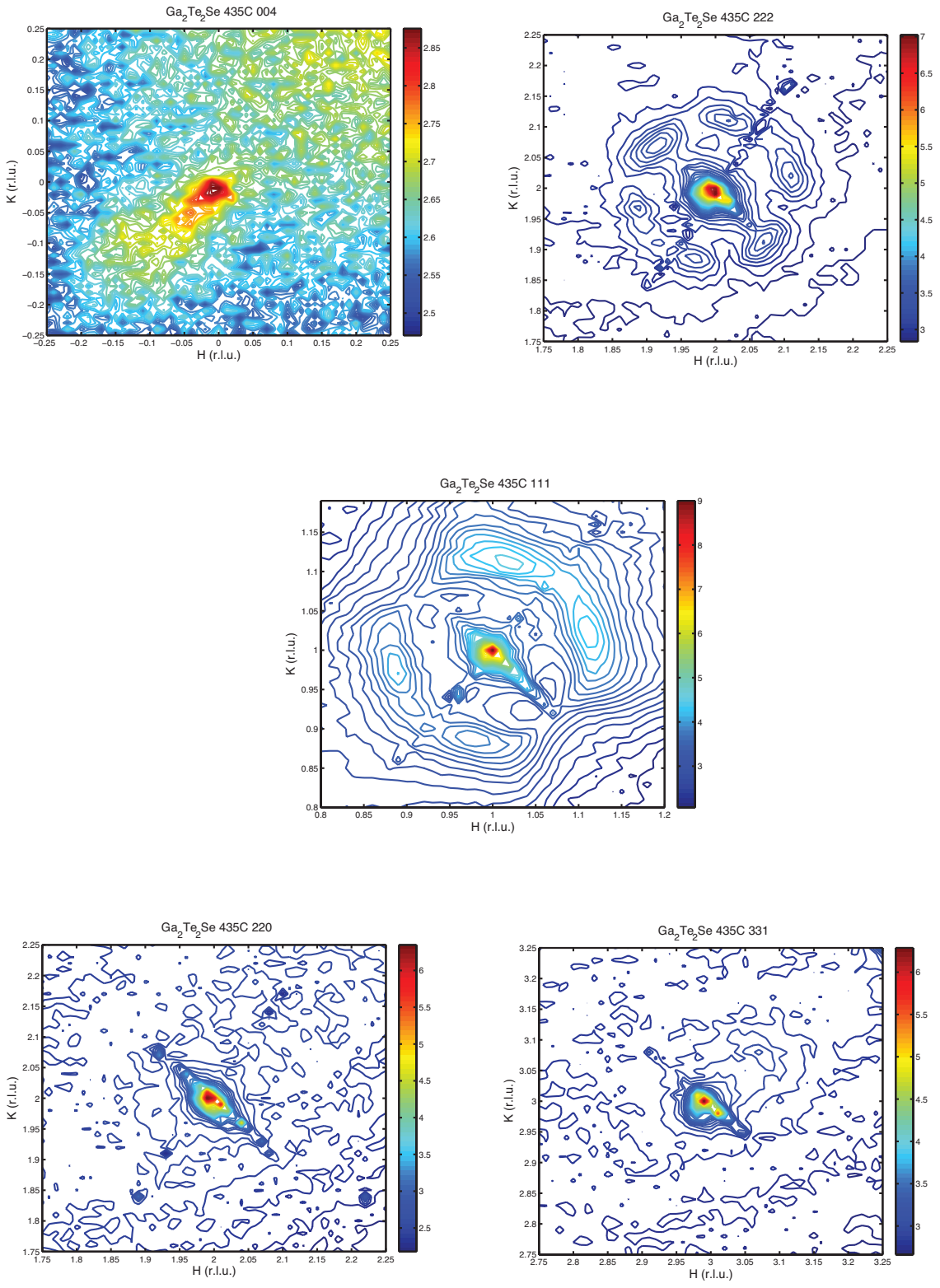

Figure 4.19: Two-dimensional reciprocal lattice contour maps of 435 °C Ga_2SeTe_2 crystal at the 004, 222, 111, 220, and 331 Bragg reflections.

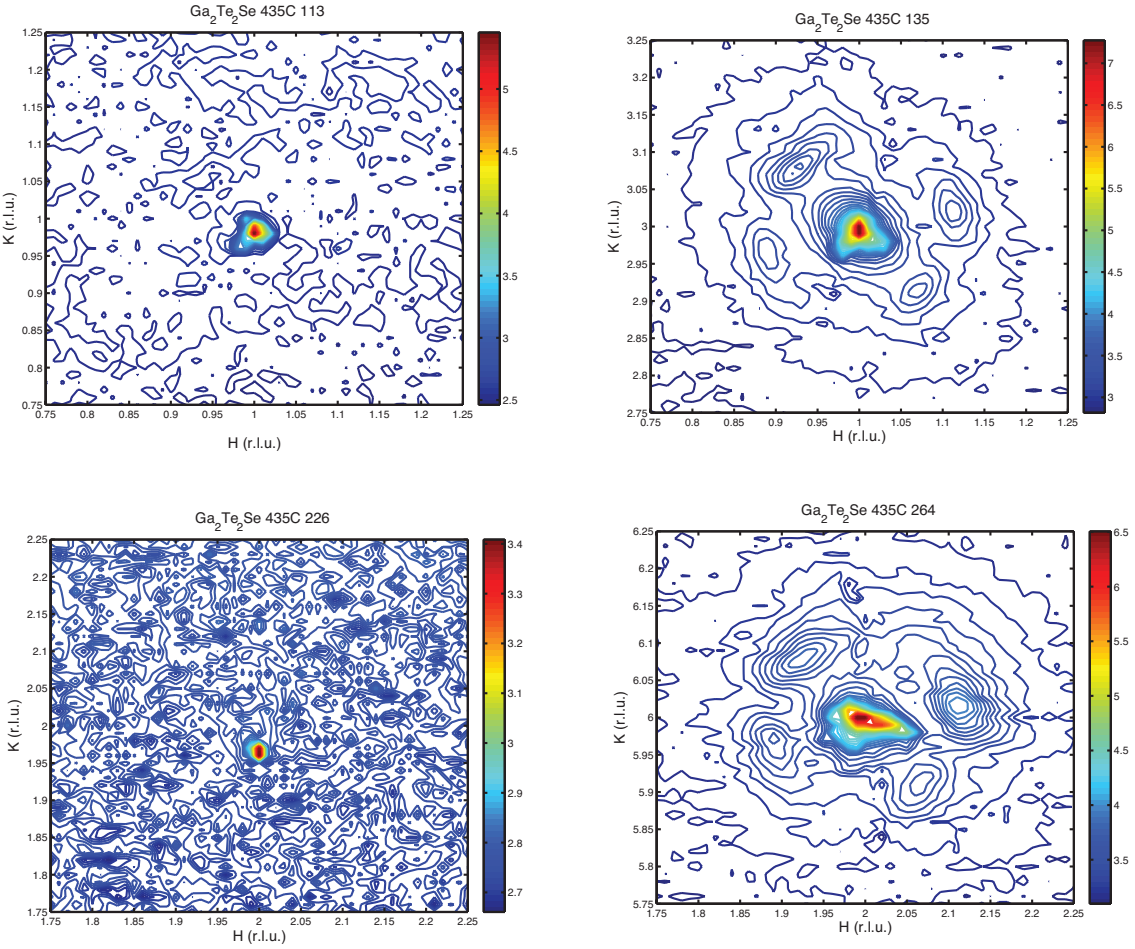

Figure 4.20: Two-dimensional reciprocal lattice contour maps of 435 °C Ga_2SeTe_2 crystal at the 113, 135, 226, and 264 Bragg reflections.

X-ray contour maps for the as-grown (Figures 4.17 and 4.18) and 435 °C (Figures 4.19 and 4.20) annealed samples show the cubic zincblende lattice structure as the main scattering source. Nonetheless, diffuse scattering features are observed across all Bragg reflections. For example 111, 222 contour maps show diffuse lobes that seen diagonally along the h-k axis (i.e. bottom left to upper right) in the as-grown sample are split in the 435 °C annealed sample. Similar observations occurred at other Bragg reflections such as the 333, 135, and 264. Such an observation indicates that vacancy plane ordering is not a discrete phenomenon, but a gradual process. Moreover, the observed diffuse scattering illustrates the intrinsic nature of vacancies in Ga_2SeTe_2. This is highlighted by showing the reciprocal space in the vicinity of the 111 reflection in the as-grown sample (top three contour maps in Figure 4.18). Here, the diffuse features become are more readily observed. To show this even more clearly, a three-dimensional reconstruction of the reciprocal space around the 333 Bragg reflection is attempted. This is done by collecting two-dimensional reciprocal lattice scans around the 333 reflections in h, k, and l directions. The result is shown in Figure 4.21. The three-dimensional diffuse scattering features show striking resemblance to hexagonal symmetry.

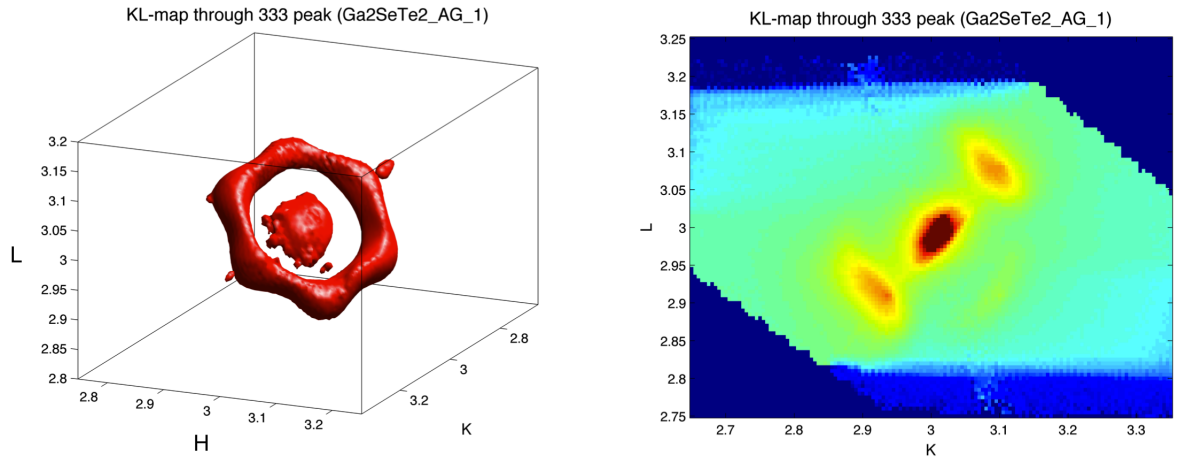

Figure 4.21: Three-dimensional reciprocal space reconstruction of (333) Bragg reflection for as-grown Ga_2SeTe_2. A (111) cut is also shown that recovers the diffraction features expected in two-dimensional reciprocal space.

4.4 High-Temperature X-Ray Diffraction

The single crystal diffraction experiments conducted at the APS and SSRL show that vacancy ordering in Ga_2SeTe_2 is readily manipulated by temperature. Moreover, the satellite peaks associated with vacancy structures appeared to form gradually when going from the as-grown to annealed specimen. In this section, in-situ high-temperature powder x-ray diffraction experiments are preformed on as-grown and annealed Ga_2SeTe_2 samples in an attempt to probe the kinetics of vacancy ordering.

4.4.1 Experimental Setup

High temperature powder XRD measurements were performed at the bending magnet beam line 12.2.2 at the ALS at Lawrence Berkeley National Laboratory. A focused beam (10 x 10 μm spot size) of 30 keV (0.4133 Å) x-rays was used to perform the diffraction experiments. Diffraction images were collected using a MAR 345 image plate detector. A LaB_6 standard powder specimen was used to measure sample-detector distance and detector tilt angles.

High-temperature measurements were conducted at ambient pressure. The setup involved mounting sealed 1 mm diameter quartz capillaries (10^{-6} Torr) containing Ga_2SeTe_2 powder between two halogen lamps where the sample can be radiantly heated (Figure 4.22). Temperature was controlled by toggling the voltage and current supplied to the lamps and was measured using a type-K thermocouple. The voltage-current relationship was linear and temperatures up to 820 °C were possible (Ga_2SeTe_2 melts at ≈800 °C).

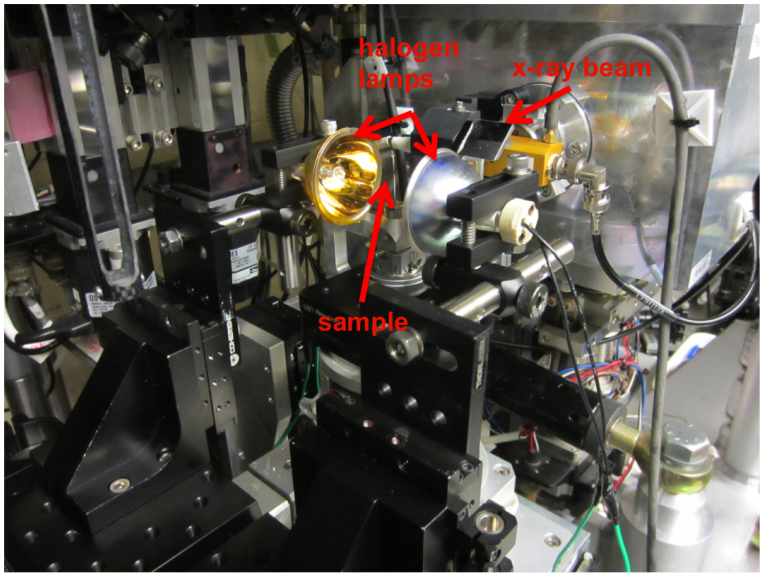

Figure 4.22: Heating setup at beam line 12.2.2 at the ALS.

4.4.2 Results and Discussion

To probe the formation of ordered vacancy planes with temperature, x-ray diffraction patterns as a function of temperature at ambient pressure are first collected for as-grown Ga_2SeTe_2. Temperature was increased from ambient to 735 °C in 100 °C increments. Data was also collected upon cool down (also in 100 °C steps). The results are shown in Figure 4.22. As the temperature is increased to 735 °C prominent satellites begin to form around the 111 and 002 Bragg reflections (labelled a-e in Figure 4.22). Upon cooling, diffraction patterns show no change from the 735 °C state. These results show that vacancy ordering in Ga_2SeTe_2 is not a discrete phenomenon, but a gradual process that is fully realized at temperatures close to the melting point. Furthermore, the vacancy ordered state remains stable upon fast cooling, as expected based on the 735°C annealing treatment applied to single crystal Ga_2SeTe_2. Equivalent experiments were also conducted for Ga_2SeTe_2 annealed under the 435 °C and 735 °C annealing treatments. The results are shown in Figures 22-23. As structural vacancies order with temperature, it is not surprising to see that the annealed samples show the same effect as the as-grown, where the intensity of satellite peaks increase with temperature. As the specimens are cooled quickly, the satellite peaks remain.

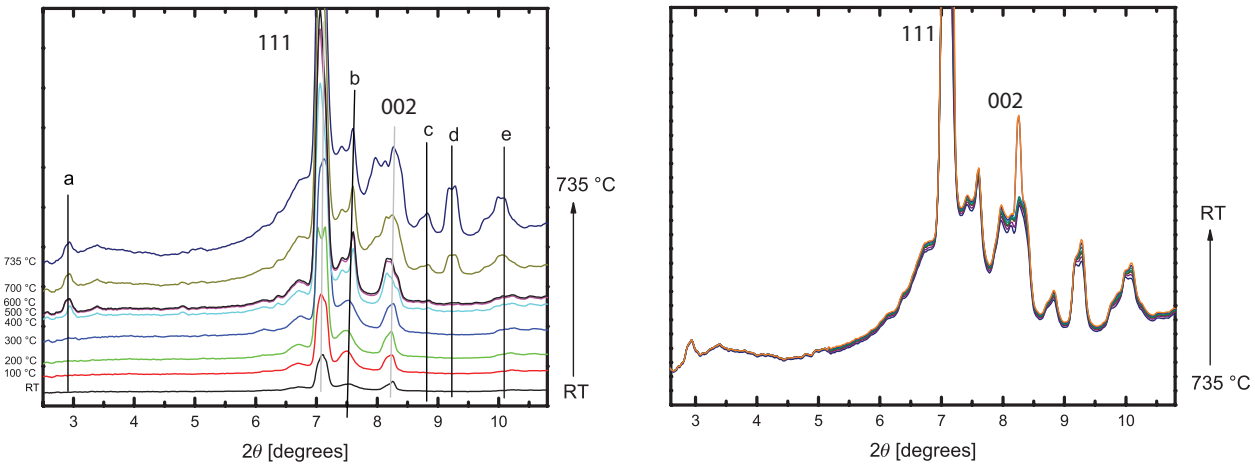

Figure 4.23: XRD patterns for as-grown Ga_2SeTe_2 as a function of increasing (right) and decreasing (left) temperature. Each pattern is normalized to the maximum value peak.

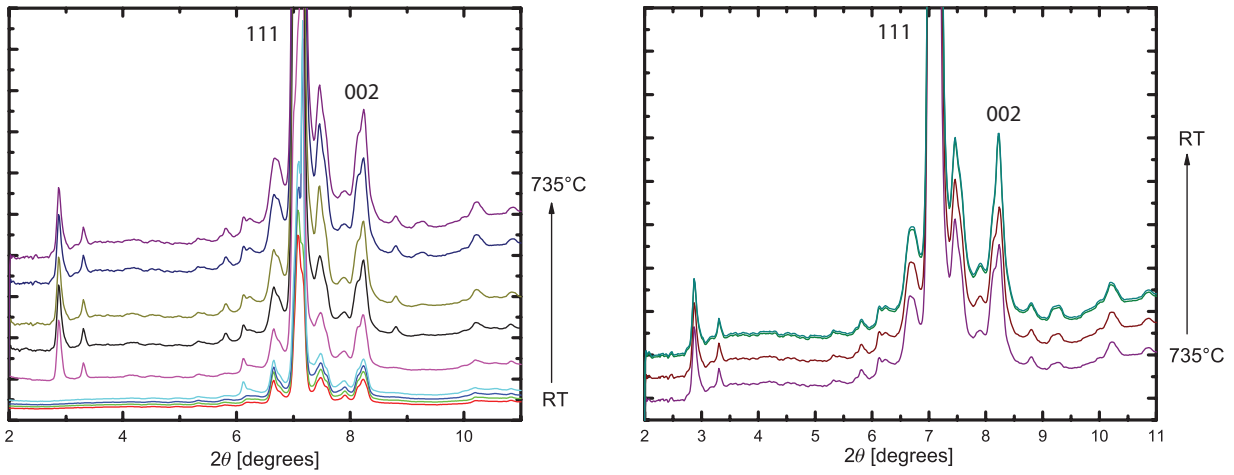

Figure 4.24: XRD patterns for 735 °C annealed Ga_2SeTe_2 as a function of increasing (right) and decreasing (left) temperature. Each pattern is normalized to the maximum value peak.

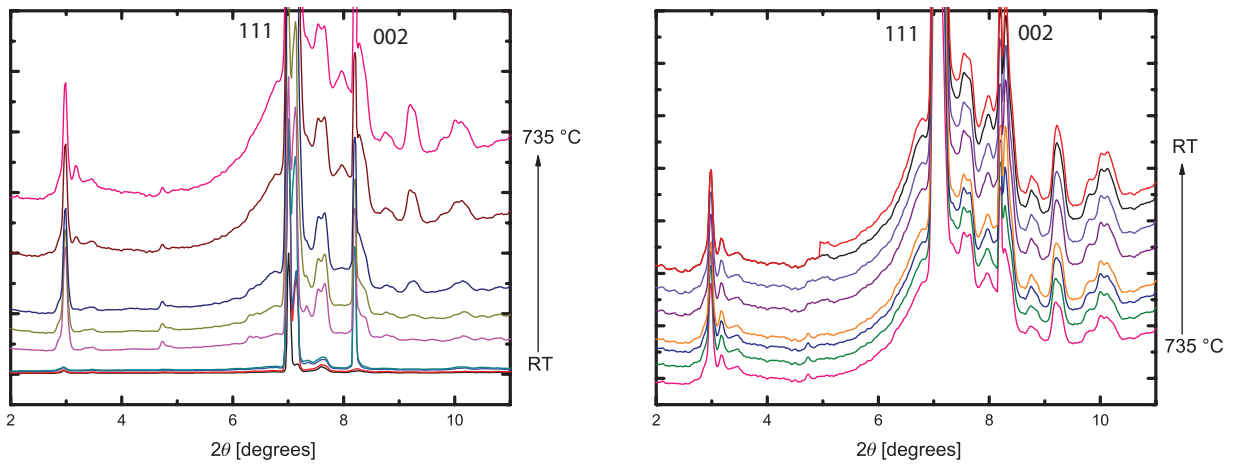

Figure 4.25: XRD patterns for 435 °C annealed Ga_2SeTe_2 as a function of increasing (right) and decreasing (left) temperature. Each pattern is normalized to the maximum value peak.

4.5 High-Pressure X-Ray Diffraction

In this section, the effect of vacancy ordering on the phase change behavior of Ga_2SeTe_2 is investigated. Common phase change materials utilize compounds that have a high concentration of structural vacancies for phase change random access memory applications. To alter the phase change behavior, the vacancy concentration is toggled (usually through stoichiometry variation). Yet altering phase-change dynamics by vacancy redistribution (vacancy ordering being an example) is a topic that is scarcely studied.

4.5.1 Experimental Setup

High-Pressure powder diffraction was carried out at beam line 12.2.2 at the ALS. The experimental geometry and x-ray beam was identical to that used in the high-temperature diffraction experiments disused in Section 4.4. Measurements were carried out at ambient temperature using a standard symmetric diamond anvil cell (DAC). The DAC consisted of two 300 μm cutlet diamonds with a 60 μm indented rhenium gasket in between. Ga_2SeTe_2 powder mixed with pressure transmitting fluid (a 4:1 methanol/ethanol mixture) and a pressure marker (ruby pieces) was loaded in a 180 μm hole drilled at the center of the indentation. A more detailed description of the instrument setup at beam line 12.2.2 at the ALS has been reported elsewhere.[74] The setup is shown in Figure 4.46.

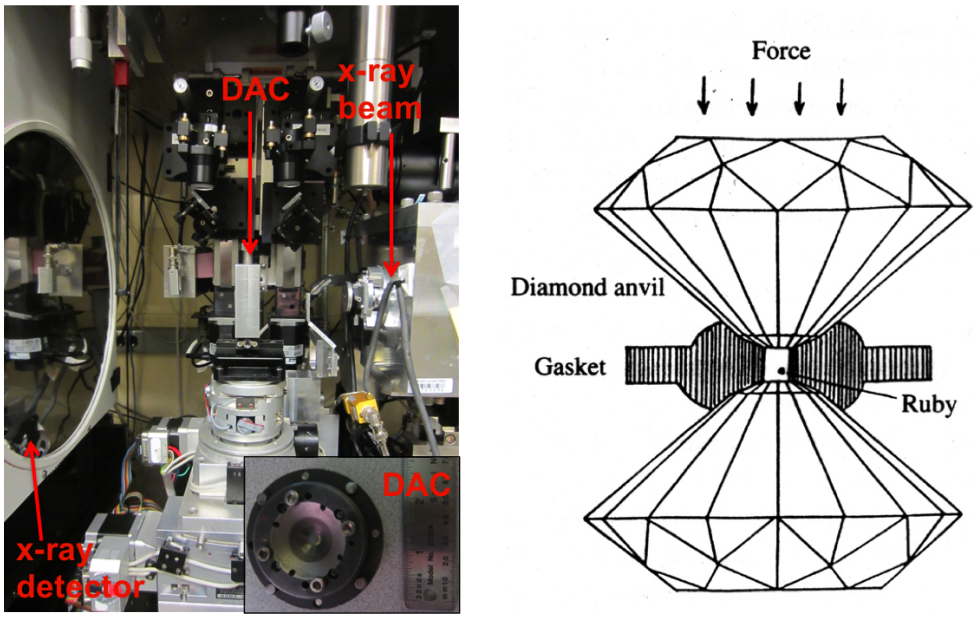

Figure 4.26: Diamond anvil cell mounted at beam line 12.2.2 at the ALS. The inset shows the diamond anvil cell, where the pressure is increased by tightening the screws that cause the diamonds to compress the sample, as illustrated in the diagram.[75]

4.5.2 Results and Discussion

X-ray diffraction patterns as a function of increasing pressure for the as-grown, 435 °C, and 735 °C annealed Ga_2SeTe_2 specimens are shown in Figure 4.27 (a-c). All samples showed Bragg peaks that correspond with a cubic zincblende structure. Additional peaks located at $2\theta \approx 9.9$ ° and $2\theta \approx 11.3$ ° are attributed to the rhenium gasket within the DAC. Upon compression, the Bragg reflections shift toward higher angles indicative of unit cell compression. The key observation in the compression data, however, is the thermal history of Ga_2SeTe_2 seems to have an effect on its solid-state amorphization. During compression the as-grown and 735 °C specimens show a cubic to amorphous phase transition between ≈10 GPa and 12 GPa evinced by the formation of broad amorphous bands at $2\theta \approx 8.8°$ and $2\theta \approx 12.5$ ° Above 12 GPa, the specimens remain amorphous with no additional phase transition up to ≈ 50GPa. The compression behavior of the 435 °C annealed sample is identical to the other two with the exception that solid-state amorphization occurred at lower pressure, between 7 GPa and 8 GPa. This suggests that structural vacancy distribution has a direct effect on the amorphization behavior of Ga_2SeTe_2. Additionally, diffraction patterns as a function of decompression on as-grown, 435 °C, and 735 °C annealed specimens were collected. For all samples the cubic zincblende phase was not recovered as the pressure was lowered to ambient conditions (Figure 4.28 shows the decompression results for the as-grown and 735 °C annealed samples). This implies that the solid-state amorphization observed of Ga_2SeTe_2 is an irreversible phenomenon.

The most interesting result from the high pressure experiments is the observation that the 435 °C annealed sample underwent a crystal-amorphous phase transition at lower pressures than the as-grown and 735 °C annealed specimen. This suggests that vacancy ordering plays a role in the solid-state amorphization of Ga_2SeTe_2. The notion that vacancy ordering and disordering can induce pronounced changes in material properties is a field that is being actively investigated. Recent investigations on the role of vacancies in phase-change materials have shown that vacancy ordering-disordering can induce metal-insulator phase transitions.[53,54,76] Density functional theory (DFT) calculations ,using a $Ge_{125}Sb_{1024}Te_{2048}$ super-cell, revealed an insulator to metal transition driven by a progression of disordered vacancy (manifested as vacancy clusters, which create localized electronic states) to ordered vacancy layers.[54] Furthermore, vacancy ordering was also responsible for the occurrence of a structural phase transition (cubic to hexagonal).[54] The high-pressure diffraction results appear to be analogous in the sense that the extent of vacancy ordering governs the cubic to amorphous transition of Ga_2SeTe_2. It is posited that Ga_2SeTe_2 with highly disordered vacancies exhibits an energetically unstable state that is more likely to collapse under high pressures than Ga_2SeTe_2 with ordered and partially ordered vacancy planes. DFT calculations conducted by Zhang et al for $GeSb_2Te_4$ have shown that a fully vacancy ordered phase is the most stable and it is possible that Ga_2SeTe_2 should display similar behavior.[54]

Finally, the irreversibility of Ga_2SeTe_2 amorphization is discussed. Such an occurrence is likely related to its defect zincblende structure. Recall from Section 1.4 that single crystal diffraction experiments revealed streaking in all of the observed Bragg reflections. This im-

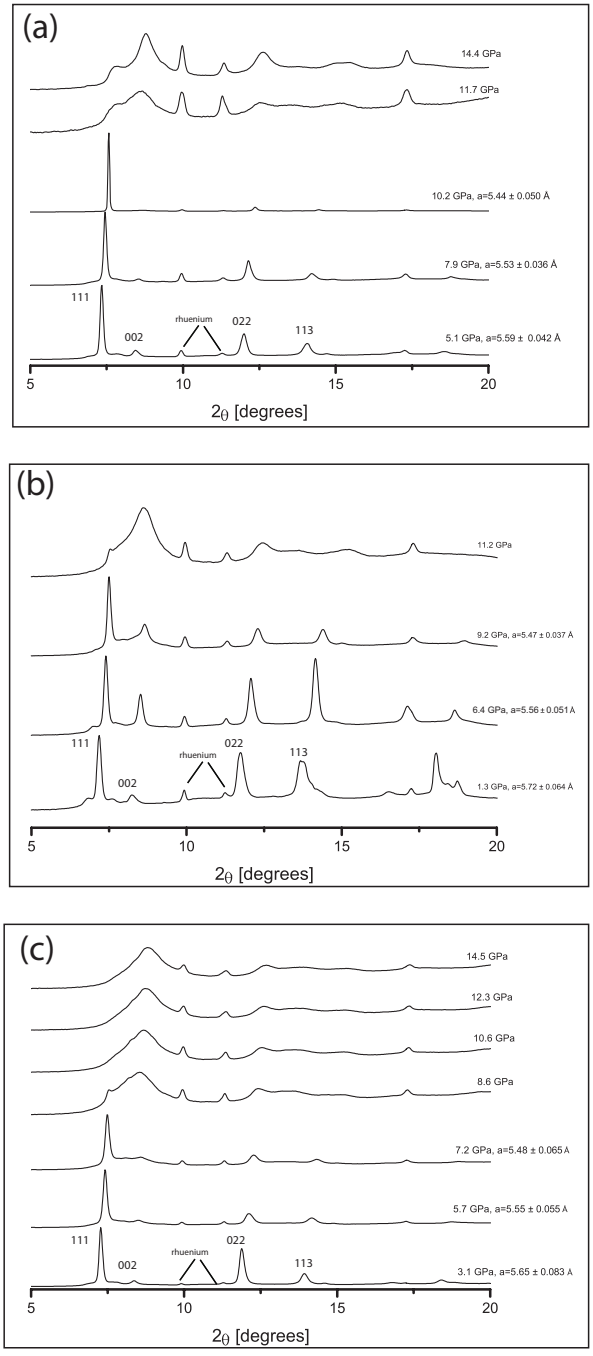

Figure 4.27: diffraction patterns as a function of increasing pressure for as-grown (a), 735 °C annealed (b), and °C annealed (c) Ga_2SeTe_2 samples.

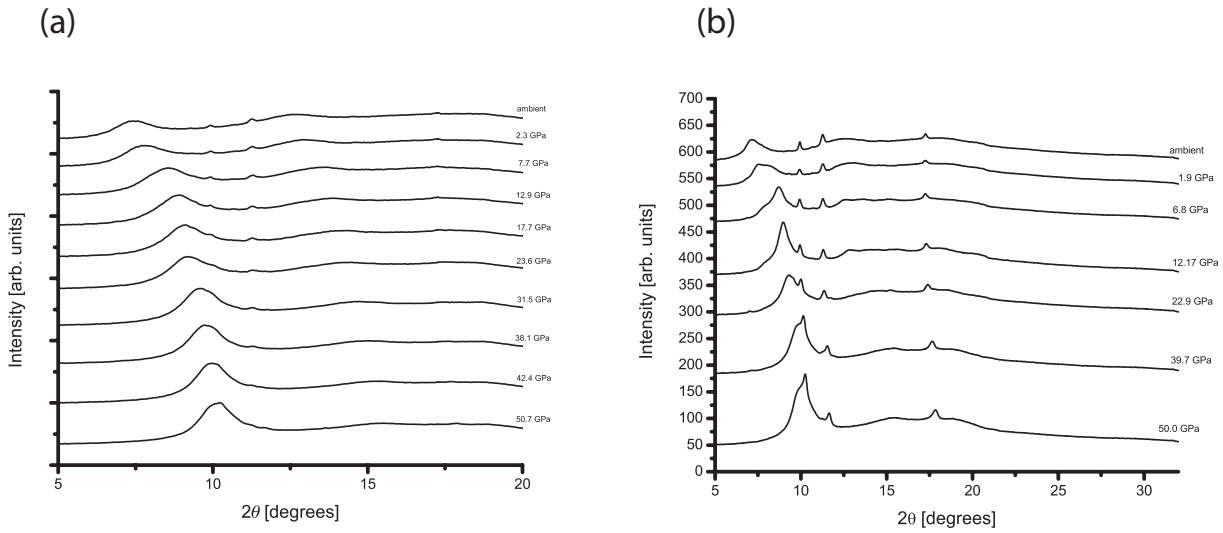

Figure 4.28: Diffraction patterns for 735 °C annealed (a) and as-grown (b) Ga_2SeTe_2 upon decompression from ≈ 50 GPa to ambient conditions. After decompression the sample remains amorphous. Identical behavior was observed for the as-grown and 435 °C annealed specimens. The sharp peaks originate from the rhenium gasket.

plies that the crystalized lattice under ambient conditions is under strain, likely caused by the secondary vacancy plane structures that exists within the lattice. As the the pressure is increased to the amorphization point, the lattice collapses and the strain induced by the structural vacancies is released. This means that amorphous Ga_2SeTe_2 should be more energetically stable than crystalline Ga_2SeTe_2. Consquently, upon decompression, amorphous Ga_2SeTe_2 does not refer back to its crystalline state.

4.6 Conclusions

X-Ray diffraction experiments have revealed that vacancy ordering in Ga_2SeTe_2 is highly dependent on sample thermal history. Room temperature powder diffraction measurements show that Ga_2SeTe_2 annealed at 735 °C then quenched produced ordered two-dimensional vacancy structures that are parallel to <111> directions. Annealing specimens at 435 °C followed by a slow cool appeared to cause disordering of the two-dimensional vacancy structures. Single crystal diffraction showed that the diffraction behavior of vacancy structure extends to all Bragg reflections (satellites were visible at all allowable reflections). This may indicate that of two-dimensional modulated vacancy structures occur at different orientations other than {111}, though this cannot be verified. Elongation across all Bragg reflections was observed, which indicates that the structural vacancies in Ga_2SeTe_2 strain the lattice, though the symmetry of the zincblende lattice is preserved. However, there may be local distortions

around the Ga, Se, and Te atomic environments.

High-pressure (ambient temperature) x-ray diffraction experiments have revealed that the extent of vacancy ordering has a direct effect on the amorphization of Ga_2SeTe_2. Ga_2SeTe_2 with disordered vacancies amorphized at $\approx$ 7-8 GPa as opposed to specimens with ordered and semi-ordered vacancies, which became amorphous at $\approx$ 10-11 GPa. This suggests that a Ga_2SeTe_2 crystal lattice with disordered vacancies is energetically less stable than ordered and semi-ordered systems. High temperature diffraction (ambient pressure) experiments showed that the process of vacancy ordering is gradual with increasing temperature. Overall, the results serve as evidence that a material's phase change behavior is altered by its intrinsic structure.

Chapter 5

X-Ray Absorption Fine Structure (XAFS)

5.1 X-Ray Absorption in Crystals

The x-ray diffraction investigation presented in Chapter 4 hinted that structural vacancies appeared to strain the cubic zincblende lattice as evidenced by Bragg peak streaking. However, diffraction experiments show that the cubic zincblende symmetry was still preserved. As a results it is suspected that structural vacancies distort the cubic lattice at atomic length scales. In this section, the local structure is probed utilizing x-ray absorption fine structure (XAFS) experiments on as-grown and annealed Ga_2SeTe_2 specimens.

Where the diffraction of x rays in a crystal reveals can reveal global structural information, absorption of x rays can serve as a probe of the local environment of a crystal. Materials characterization via x-ray absorption utilizes the photoelectric effect. Here, incident photons on an atom transfer energy to a bound electron, and in the process, get annihilated. If the photon energy is greater than the binding energy of an orbital electron, the absorbing electron can be excited to the continuum of free states (illustrated in Figure 5.1a). This in turn causes discontinuous increases in the absorption cross-section for x-rays with energies greater than the binding energies of atomic electrons. These features in the photon absorption spectrum for an atom are known as absorption edges (shown in Figure 5.1b). Since electrons are bound in atoms at discrete energy levels, the occurrence of absorption edges likewise occurs at discrete energies.

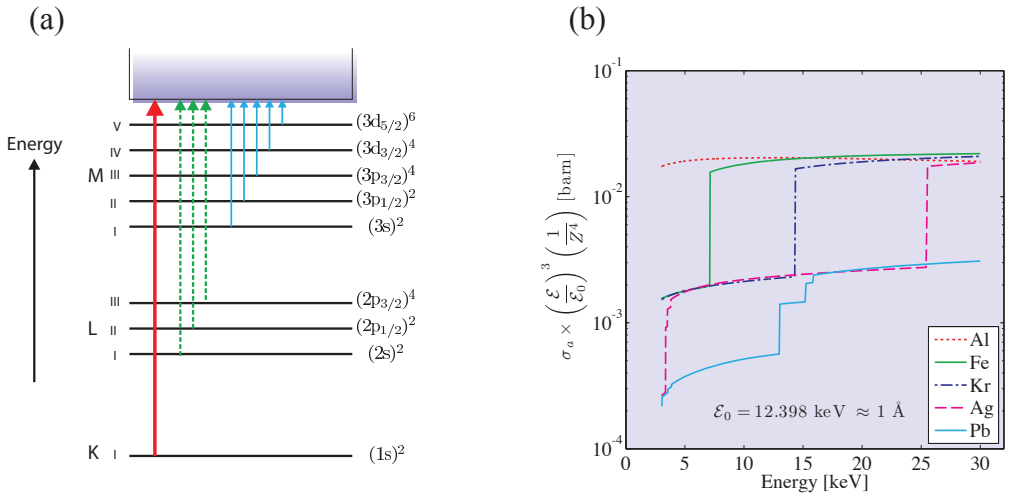

Figure 5.1: (a) Schematic as reproduced from Als-Nielsen and McMorrow showing the process of x-ray absorption in an atom by atomic orbital electrons, (b) photon absorption cross-section for aluminum, iron, krypton, silver, and lead.[67]

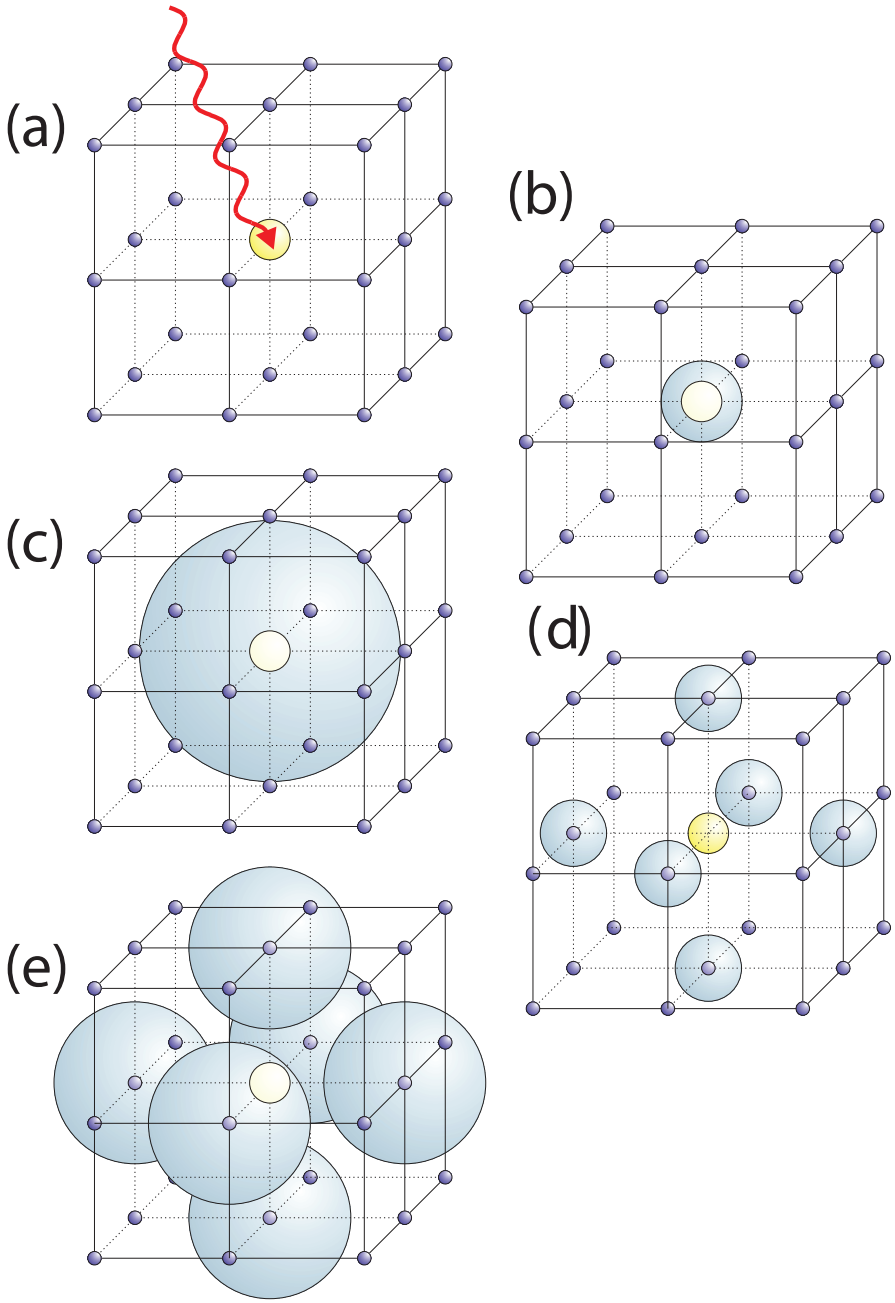

Figure 5.2: Representation of the EXAFS process as reproduced from Als-Nielsen and McMorrow.[67] (a) x-ray photon incident on an atom in a crystalline lattice. If the energy of the photon is high enough, it can liberate an bound atomic electron. During this process the photon is absorbed. In (b)-(c) the released photoelectron propagates in the lattice as a spherical wave. Neighboring atoms in the lattice scatter the spherical wave, shown in (d)-(e), resulting in back scattered waves. Oscillations in the absorption cross-section are produced by the interference between outgoing and backscattered photoelectron spherical waves.

When photoelectric absorption occurs in system consisting of an assembly of atoms (e.g. crystals, molecules) the absorption edges in the photon absorption spectrum develop structure. The collective phenomena that lead to structure in the absorption cross-section are known as x-ray absorption fine structure (XAFS). These can be can be categorized according to the energy of the incident photon relative to the absorption edge:[67] The x-ray absorption near edge structure (XANES) occurs within ± 10 eV of the edge where the absorption cross-section may overshoot the discrete steps expected for a single atom. This physically corresponds to released electrons occupying unfilled bound states close to the continuum of free electron states. Here, the density of such unbound states may be higher than the density of free electron states, resulting in a peak in the absorption cross-section. At higher photon energies, the absorbing photoelectron is liberated and propagates in a lattice as a spherical wave, which can be back scattered by neighboring atoms to produce oscillations in the absorption cross-section. At 10 eV to 50 eV within the absorption edge, known as the near edge x-ray absorption fine structure (NEXAFS) region, the liberated photoelectron may undergo multiple scattering events. For photon energies from 50 eV to 1000 eV above the absorption edge, the photoelectron has ample energy where single scattering events dominate. This regime is known as the extended x-ray absorption fine structure (EXAFS) and has found widespread use in the determination of material local structure.

EXAFS signals in x-ray absorption spectra are extracted using the dimensionless quantity $\chi(\mathrm{k})(E)$.[67,77] It is define as,

$$\chi(\mathrm{k}(E)) = \frac{\mu_\chi(E) - \mu_0(E)}{\mu_0(E)}, \tag{5.1}$$

where μ_χ is the absorption coefficient of the material being studied and μ_0 is the absorption coefficient of a single atom (where there is no fine structure) as a function of energy E. The quantity $\mathrm{k}(E)$ is the electron wave number, which has units in reciprocal length and is defined as

$$\mathrm{k}(E) = \frac{1}{\hbar}\sqrt{2m(E - \hbar\omega)}, \tag{5.2}$$

where ω is the angular frequency of the wave and m is the electron mass. Traditional representations of EXAFS signals are weighted by the cube of the electron wave number, or $\mathrm{k}(E)^3\chi(\mathrm{q})$. The Fourier transform of $[\mathrm{k}(E)]^3\chi(\mathrm{k})$ gives a radial distribution function that has peaks corresponding to the position of shells of the nearest neighbors of the atom which absorbed the incoming photon in the crystal lattice.

To illustrate how local structure can be probed via EXAFS, the absorption behavior of CdTe is discussed as an example.[67] Absorption spectra for photon energies in the vicinity of the Te K-edge (31.814 keV), $[\mathrm{k}(E)]^3\chi(\mathrm{k})$ versus k, and the Fourier transform of $[\mathrm{k}(E)]^3\chi(\mathrm{k})$ for bulk and nano-crystalline CdTe is shown in Figures 5.3a-c. Based on the EXAFS oscillations observed in Figures 5.3a-b, the difference in the local structure of the bulk and nano material is evident. In the nano material, the EXAFS oscillations have one dominant frequency, which means that the local structure is dominated by the singular nearest neighbor atom around Te. The bulk EXAFS signal shows a superposition of multiple frequencies, indicative of multiple nearest neighbor shells contributing to the local structure. The Fourier

transform of the EXAFS signal gives a radial distribution function with peaks that correspond to the nearest neighbor shells of the absorbing Te atom. Here, the nano-crystal has one primary peak at 2.79 Å. Compared with the 2.806 Å Te-Cd atomic distance in bulk CdTe, the small contraction is attributed to epitaxial strain originating from the organic matrix that contains the nano crystal. The radial distribution function for the bulk, as one would expect, shows peaks corresponding to the positions of multiple shells of nearest neighboring atoms that contribute to the EXAFS signal.

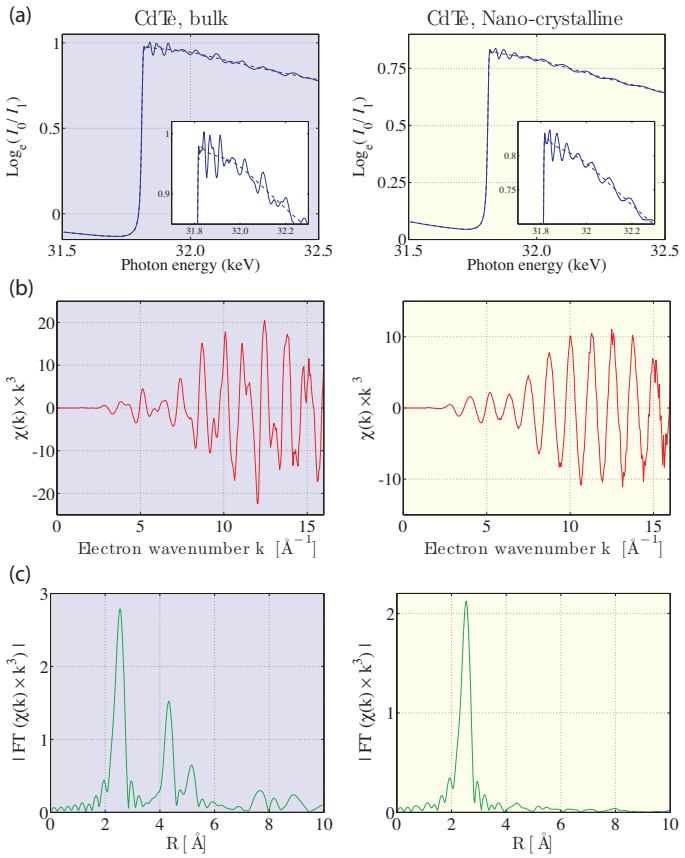

Figure 5.3: Comparison of bulk and nano-crystalline CdTe EXAFS spectra as reproduced from Als-Nielsen and McMorrow.[67] (a) absorption spectra where the dotted lines in the inset indicates the absorption behavior of a single Te atom, (b) $[\mathrm{k}(E)]^3\chi(\mathrm{k})$ as a function of wave number k, and (c) Fourier transform of the data plotted in (b), which results in radial distribution functions with peaks corresponding to the atomic shells of the nearest neighbor atoms of Te.

5.2 Experimental Setup

XAFS experiments require one to utilize an x-ray beam corresponding to the binding energies of atomic electrons in the material being studied. This requires a highly tunable x-ray source, which means that XAFS experiments can only be carried out at synchrotrons. XAFS measurements on Ga_2SeTe_2 specimens were carried out at SSRL (beam line 4-1) and at APS (beam line 05-BM). As-grown (short range vacancy ordering), 435 °C annealed (disordered vacancies), and 735 °C annealed (ordered vacancies) Ga_2SeTe_2 specimens in the form of 60 μm powders were prepared and were dispersed onto plastic tape. The samples were mounted at the beam line in a transmission geometry setup (shown in Figure 5.4) where absorption spectra were collected at x-ray energies corresponding to the Ga (10.367 keV), Se (12.658 keV), and Te (31.814 keV) K-edges, constituting nine total scans. X-ray energies were tuned via a Si (111) monochromator. Three reference standards were used to calibrate the x-ray beam at each K-edge energy: (1) elemental Ga for Ga K-edge, (2) HgCl L_{III}-edge for Se K-dege, and HgI I K-edge for the Te K-edge.To ensure statistically reliability, five scans were taken for each sample at each x-ray energy. Data analysis was done via the SIXPACK software package.[78]

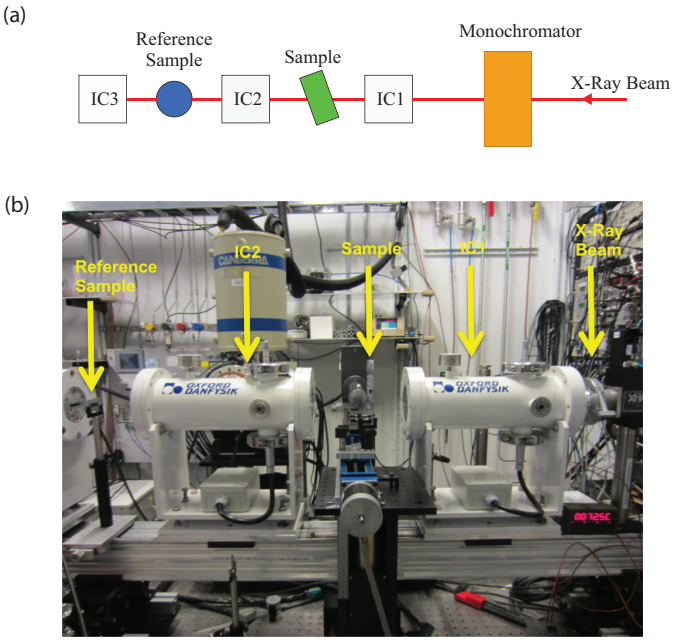

Figure 5.4: (a) Schematic of a transmission geometry setup where the incident and transmitted x-ray beam are collected by two ionization chambers. (b) XAFS experiment setup at the APS at beam line 05-BM.

5.3 Results and Discussion

Extracting the EXAFS signal at the Te-kedge and plotting against electron wave number reveals a similar oscillatory behavior across the as-grown, 435 °C annealed (disordered vacancies), and 735 °C annealed Ga_2SeTe_2 samples. However, at high q (≈ 10 Å^{-1}) the structure in the as-grown specimen begins to deviate. To see this the Fourier transform of the EXAFS data is examined, which gives the radial distribution function that characterizes the local environment around the central Te atom. Globally, Ga_2SeTe_2 is formed via Ga-Te and Ga-Se tetrahedra packed in the cubic zincblende structure. As result, the nearest neighbor shell around the Te atom should correspond to the cation-anion (Ga-Se or Ga-Te) distance, which is ≈ 2.50 Å . For all three samples, however, the dominant scattering shell occurs at 2.27 Å indicating that the two dimensional vacancy structures present in Ga_2SeTe_2 locally contract the Ga-Te dumbbells within the cubic structure. Another interesting feature is that there seems to be additional scattering shells around Te in the as-grown sample (located around ≈ 1.00 Å), which are relatively suppressed in the annealed samples. This suggests that there is a more complex local structure around Te in as-grown Ga_2SeTe_2 that may arise from extrinsic defects formed during crystallization that may be eliminated upon annealing.

EXAFS from the surrounding Se atoms shows analogous behavior, but more pronounced. Here, the common peak in the radial distribution function occurs at ≈ 2.14 Å, significantly shorter than the cation-anion nearest neighbor distance of ≈ 2.50 Å. Moreover, real scattering shells are observed around ≈ 1.80 Å for all Ga_2SeTe_2 samples. These ancillary peaks provide additional evidence that the embedded structures formed by vacancies cause local distortions in the Ga_2SeTe_2 cubic lattice. As was posited for Ga-Te atomic dumbbell, the Ga-Se dumbbell may undergoe a contraction (from ≈ 2.50 Å to 2.14 Å)–since the Se anion is lighter than Te the contraction is expected to be greater. The double peak features starting at ≈ 1.00 Å observed in the as-grown samples and 435 °C samples develop into a singular peak at ≈ 1.20 Å in the 735 °C annealed sample. Such an effect represents the formation of a fully developed superstructure that coexists with the cubic structure, which was observed in the reciprocal lattice maps (Chapter 4) of the 735 °C annealed Ga_2SeTe_2 sample (i.e. the prominent satellite peaks around the main Bragg reflection).

Finally, the local environment around the Ga atom in Ga_2SeTe_2 is explored. Across all three specimens, the common peak in the radial distribution function occurs at ≈ 2.43 Å, which is less than the nominal nearest neighbor distance of ≈ 2.50 Å, indicative of cation-anion dumbbell contraction. The most intriguing feature in the Ga radial distribution function, however, is that additional shells observed in the as-grown, 435 °C, and 735 °C annealed specimens are vastly different. For the as-grown sample, prominent scattering shells are located at 1.14 Å, 1.47 Å, and 1.81 Å. In the 435 °C annealed sample, such structures are still present but have a diminished scattering intensity. As structural vacancies fully order in the 735 °C annealed sample, the strength of these shells is further diminished. For this reason, the overall EXAFS data suggests that the the bulk of the local distortions caused by structural vacancies in Ga_2SeTe_2 occur in the anion (Se and Te) environments. This is no surprise as a Ga vacancy would leave dangling anion orbitals in the Ga-Se/Te tetrahedra.

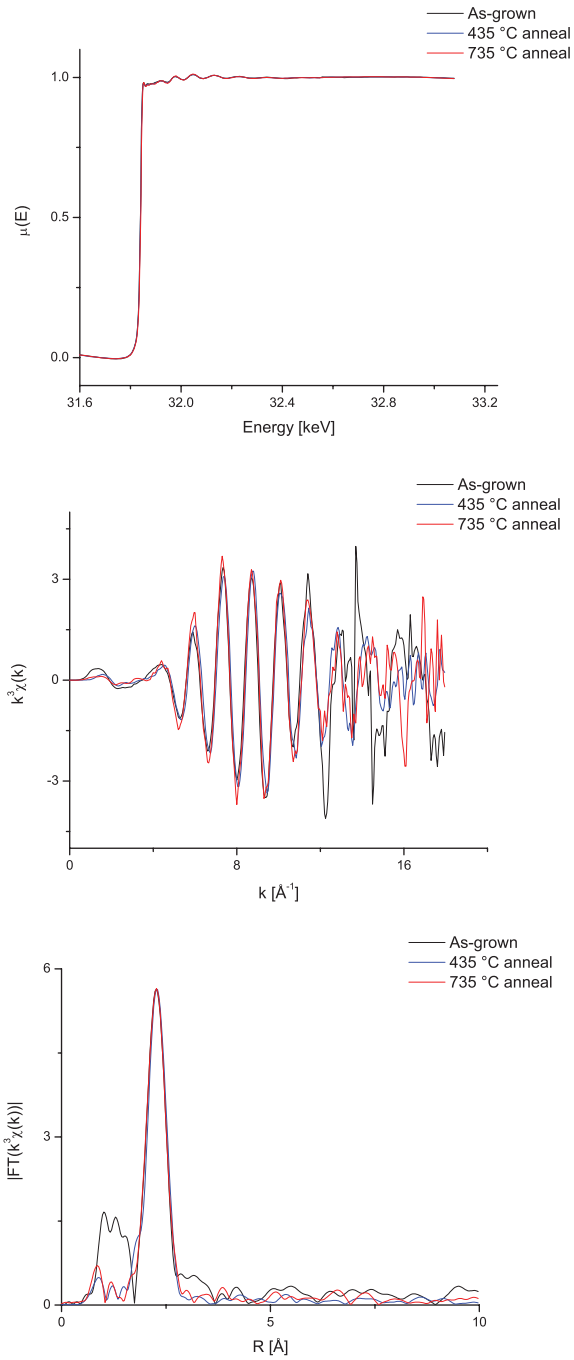

Figure 5.5: Top: Te K-edge x-ray absorption spectra. Middle: Extracted EXAFS signal plotted against k-space. Bottom: Fourier transform of EXAFS signal giving radial distribution of local structure around the absorbing Te atom in Ga_2SeTe_2.

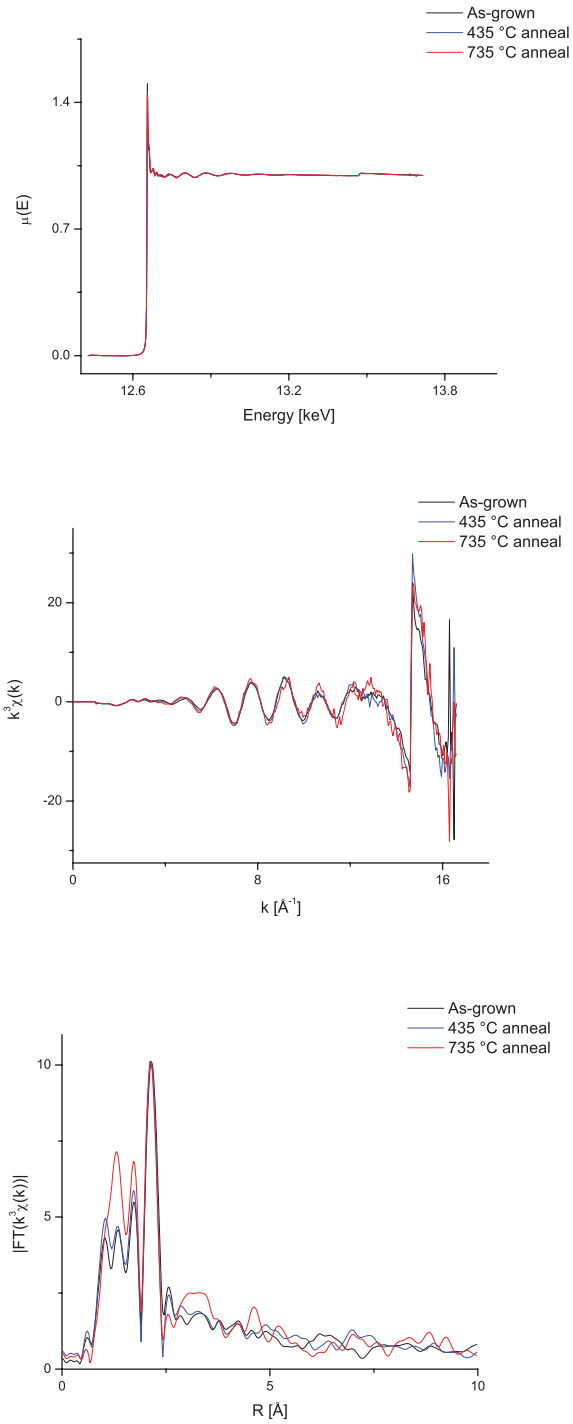

Figure 5.6: Top: Se K-edge x-ray absorption spectra. Middle: Extracted EXAFS signal plotted against k-space. Bottom: Fourier transform of EXAFS signal giving radial distribution of local structure around the absorbing Se atom in Ga_2SeTe_2.

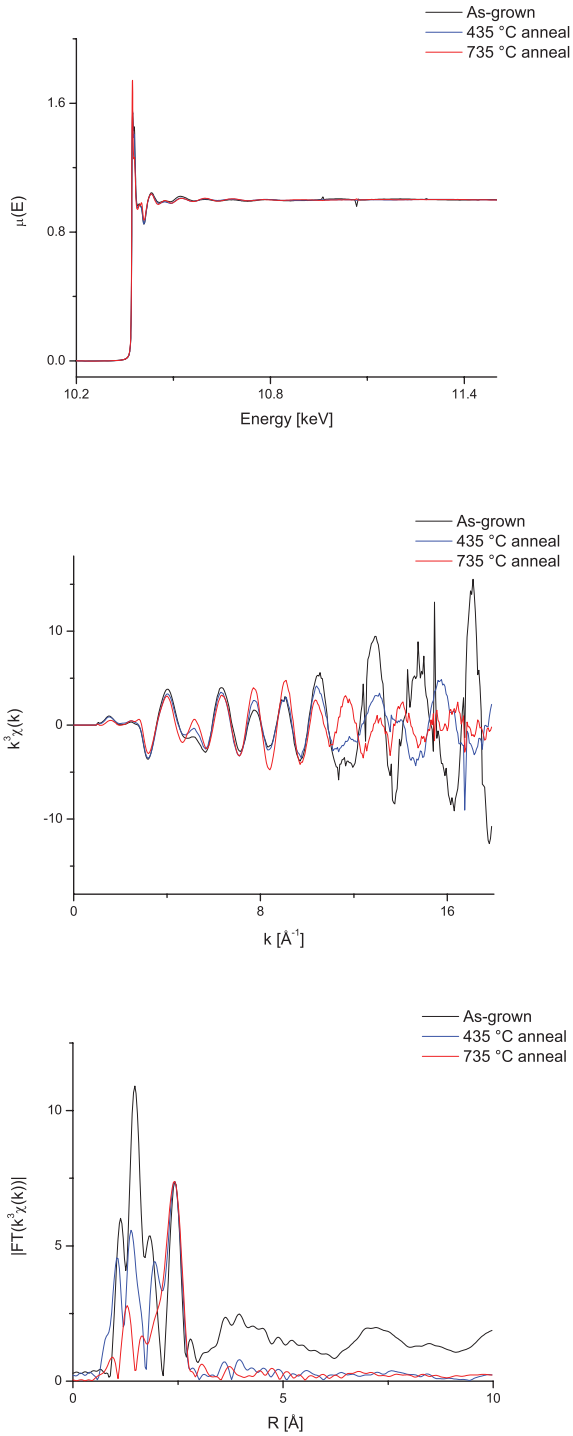

Figure 5.7: Top: Ga K-edge x-ray absorption spectra. Middle: Extracted EXAFS signal plotted against k-space. Bottom: Fourier transform of EXAFS signal giving radial distribution of local structure around the absorbing Ga atom in Ga_2SeTe_2.

5.4 Conclusions

X-ray absorption fine structure spectroscopy on as-grown and annealed Ga_2SeTe_2 reveals a rich local structure analogous to the complex global structure discovered through x-ray diffraction measurements. The local environment around Te, Se, and Ga suggests an atomic dumbbell contraction, likely caused by the presence of native vacancy structures in the Ga_2SeTe_2 crystal system. The information extracted from the EXAFS, nevertheless, only serves as an indirect probe. Therefore, it may be fruitful to make an attempt to directly observe the local structure of Ga_2SeTe_2 at the atomic level. This is the topic of the next chapter.

Chapter 6

Electron Microscopy

6.1 Introduction

In Chapters 4 and 5, the structure of Ga_2SeTe_2 was probed using x-rays; as x-ray wavelengths are on the Å length scale, information extracted from x-ray experiments is limited to its crystallographic symmetry and any inferences on local structure in Ga_2SeTe_2 from x-rays are only indirect observations (as was seen in XAFS experiments). As a result, direct observation of local structure requires a probe with length scales at the atomic level. Electrons, with wavelengths on the pm length-scale, serve as suitable probes. In this section, transmission electron microscopy on Ga_2SeTe_2 is presented in an effort to directly observe the local environment around the two-dimensional vacancy structures observed via x-rays.

From a fundamental standpoint the operation of a transmission electron microscope (TEM) is analogous to that of conventional light microscopes. In a light microscope, light is focused by a series of lenses in a column that transmits through the sample and is focused onto an imaging plate where the operator can view it at a variety of different applications. The operation of a TEM is similar, but electrons are utilized instead of light. Since electrons wavelengths are small, electron microscopes have the advantage of spatial resolutions at atom length scales. The basic elements of a TEM are shown in Figure 6.1. A TEM optical

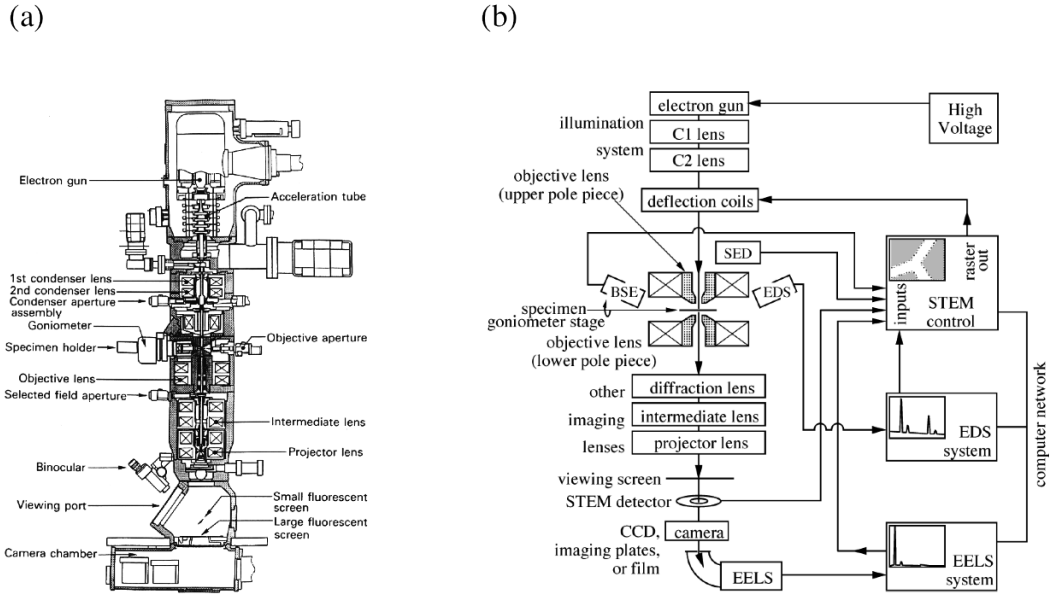

Figure 6.1: (a)Basic elements of a standard TEM. (b) Schematic of a TEM with scanning transmission electron microscopy (STEM) capability as reproduced from Fultz and Howe.[68]

column starts with an electron source (also known as the electron gun), which consists of a cathode (i.e. filament) that is heated to create an electron beam via thermionic emission. The beam is further focused by the presence of anode electrodes. The electron beam (also called the probe) then passes through TEM optical column that is composed of lenses and

apertures (analogous to a light microscope), where electron lenses consist of magnetic materials that are capable of manipulating the trajectory of the electron beam. In standard TEM instruments, the electron beam originating from the gun, with significant crossover, first passes through a condenser lens system where it can be demagnified to a concentrated spot with a size on the μm length scale. The condenser lens system also contains apertures of variable sizes that can be inserted to increase the velocity stability of the beam or protect the sample from radiation damage. The condenser apertures may also be inserted to improve the spatial coherence of electrons arriving at the sample—in other words, electron waves incident on the sample are in phase. The next stage is the objective lens and aperture systems which allows for the selection of electron beams that transmit through the sample to form the image. Electrons that transmit through the sample pass through the imaging lens system (usually composed of two intermediate and two projector lenses) that are used to correct rotational effects arising from the spiral nature of the electron beam. Finally, the beam from the imaging lenses passes through a screen phosphor image display and recording. Additionally, images formed by the electron beam can be recorded using a solid-state charged-couple device (CCD).

The two basic operations in TEM are diffraction mode or imaging mode. These are illustrated via ray diagrams shown in Figure 6.2. In diffraction mode, the back focal plane of the objective lens (denoted by the red circle in Figure 6.2a) becomes the object plane for the imaging lenses. The final result is a diffraction pattern projected onto the viewing screen. In image mode, the imaging lenses are adjusted to make the object plane the image plane of the objective (denoted by the arrow in Figure 6.2b). This image is then projected onto the view screen. Imaging may be carried out in bright field or dark field modes. In bright field imaging, contrast is created by electron absorption or scattering in the sample. Thus, thick sample regions or a samples with high atomic numbers (i.e. Z numbers) will appear dark, while regions that don't contain the sample will appear as bright. In a TEM, bright field images are formed by the direct beam of electrons transmitting through the sample by removing the the selected area diffraction aperture. Conversely, dark field images contrast is created via an electron beam that diffracts of the sample in a certain direction to form the image. Here, sample regions appear bright and regions without the sample appear as dark.

An electron beam can be focused into a narrow spot that raster scans a specimen to form an image. This is known as scanning transmission electron microscopy (STEM). The advantage here is that images are formed without the use of imaging lenses, which means that aberrations introduced from using these lenses are eliminated in STEM images. Hence, STEM imaging is more forgiving when one is trying to image thick specimens (though one must keep in mind that STEM image quality is highly dependent on the quality of the probe). An annular dark field detector can be utilized in STEM for high-angle annular dark field (HAADF) imaging. HAADF-STEM allows for the observation of atomic columns by imaging only by very high-angle incoherently scattered electrons. This also makes HAADF images extremely sensitive to a material atomic number. One must keep in mind, however, that diffraction contrast in STEM is greatly reduced due to the convergent nature of the electron beam. Hence, when imaging specimen defects, TEM is the most viable option.

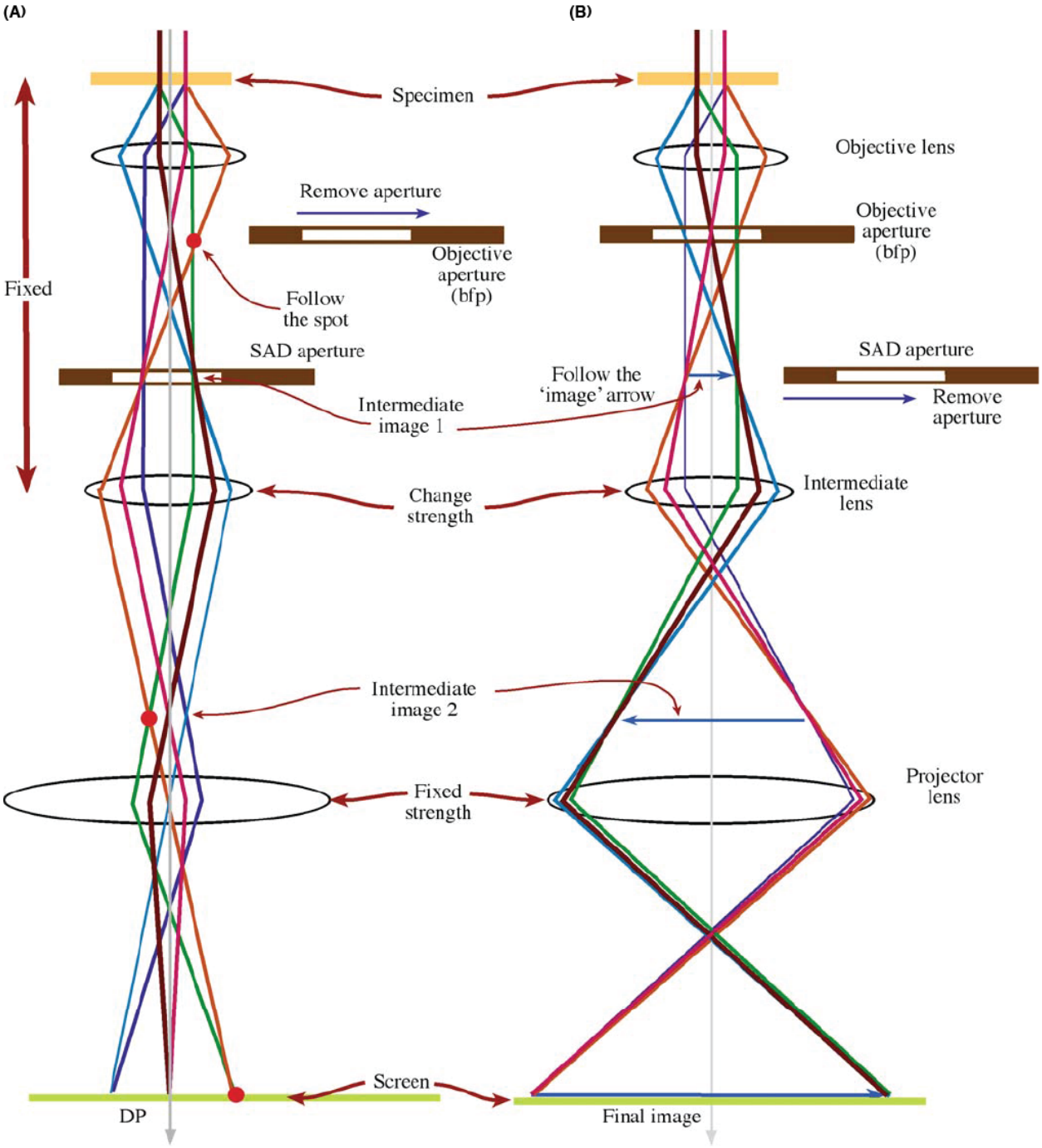

Figure 6.2: Ray diagrams showing reproduced from Williams and Carter.[79] (a)TEM in diffraction mode, where the diffraction pattern from a sample is projected onto the viewing screen and (b) TEM in imaging mode, where the sample image is projected onto the viewing screen.

6.2 Experimental Setup

Electron microscopy of Ga_2SeTe_2 was conducted at the National Center for Electron Microscopy (NCEM) at Lawrence Berkeley National Laboratory (LBNL). As-grown and annealed Ga_2SeTe_2 specimens (thermal treatments were discussed in Chapter 4) were prepared for electron microscopy by grinding single crystals in an agate mortar and pestle mixed into an isopropanol solution. The solution was dispersed on gold ultra-thin carbon TEM grids for electron microscopy characterization.Conventional TEM and STEM microscopy methods were employed to study the structure of Ga_2SeTe_2 at the atomic level. TEM imaging was performed using a modified Philips CM300FEG/UT (shown in Figure 6.3) electron microscope with a field-emission electron gun and an ultra twin objective lens system with low spherical aberration (C_s = 0.60 mm) capable of spatial resolution on the order of 1 Å. Specimens are loaded into the microscope using a Philips double-tilt low background holder capable of $\pm 30^\circ$ rotation around the x and y axes. Diffraction and imaging using the CM300 microscope was done at operating voltage of 300 kV.

STEM was carried out using a transmission electron aberration-corrected electron microscope (known at TEAM I). The instrument is a modified FEI Titan 80-300 equipped with a high-brightness Schottky-field emission electron gun, a gun monochromator, and a high-resolution GIF Tridiem energy-filter. Two CEOS hexapole-type spherical aberration correctors and chromatic a chromatic aberration corrector are also installed in the system. These auxiliary lenses correct for spherical and chromatic aberrations introduced from electron lenses.[80] Specimens are loaded onto the TEAM stage that consists of probes (similar to chopsticks) with axial tilts capable of $<\pm 180^\circ$ and has a movement precision of 0.014 nm. STEM experiments were conducting at operating voltage of 300 kV, where a spatial resolution of 0.078 nm is possible.

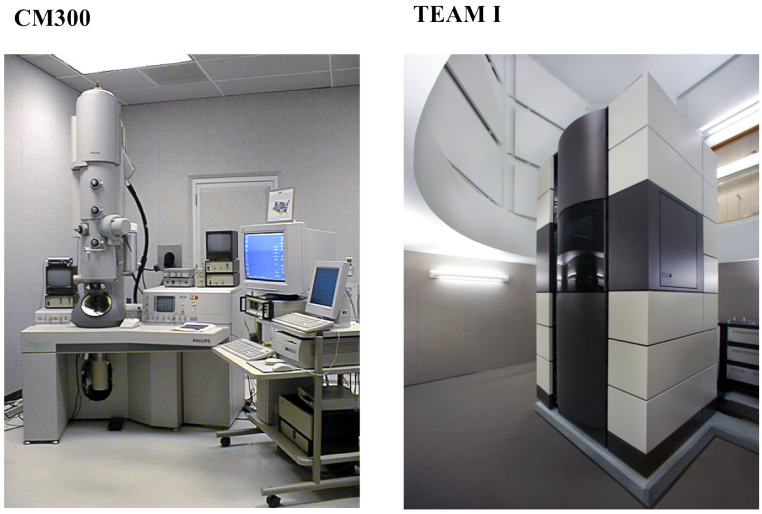

Figure 6.3: CM300 and TEAM I electron microscopes at NCEM.

6.3 Results and Discussion

The first electron microscopy images of Ga_2SeTe_2 with ordered vacancies were collected using the CM300 microscope. This was done by finding single crystalline regions on the TEM sample grid thin enough to give satisfactory images. A single crystalline region was tilted to a particular zone axis in order to view the crystal structure at that projection. This is accomplished by tilting the specimen while simultaneously observing the electron diffraction patterns until the desired symmetry for a particular zone axis is achieved. Figure 6.4 shows the diffraction patterns collected for that Ga_2SeTe_2 crystals viewed in the [110] and [111] zone axes. The symmetry observed in the diffraction patterns matches that of the face-centered cubic Bravias lattice associated with a zincblende crystal structure. In the [110] zone axis, additional super lattice reflections are observed that propagate in <111> directions in reciprocal space, where they occur at 1/8 the distance of the main {111} type Bragg reflections. No prominent superstructure was seen in the [111] zone axis, though very fine satellite spots were observed at {220} type reflections. To observe the superstructure, TEM images were collected in the [110] zone axis. These are shown in Figures 6.5 and 6.6. As expected from previous investigations on Ga_2Te_3, a two-dimensional vacancy superstructure is observed that propagates through the crystal in <111> directions. Here, rhomboid shaped crystal domains are bounded by the vacancy structures (arrowed in Figures 6.5 and 6.6). As indicated by the diffraction patterns, the vacancy structure periodicity is $\approx$ 2.7 nm, corresponding to 1/8 of the {111} lattice plane spacing.

[110] Zone Axis

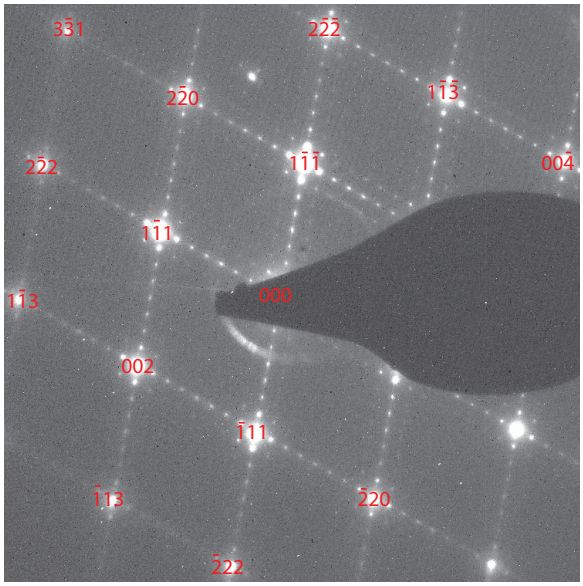

[111] Zone Axis

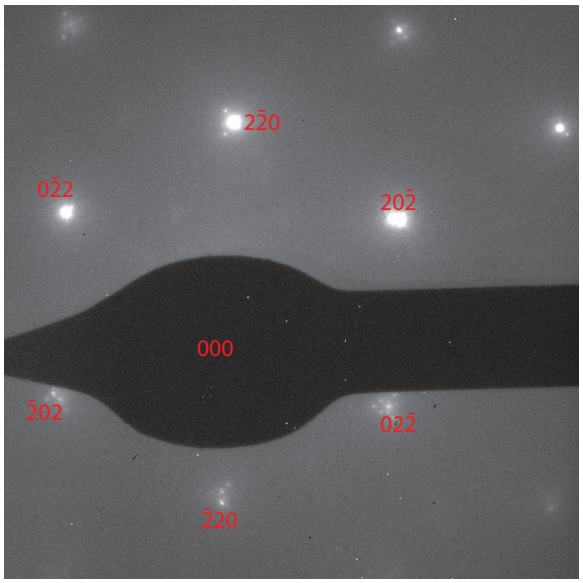

Figure 6.4: Electron diffraction patterns collected at the CM300 microscope of Ga_2SeTe_2 with ordered vacancies (i.e. 735 °C anneal) in the [110] and [111] zone axes.

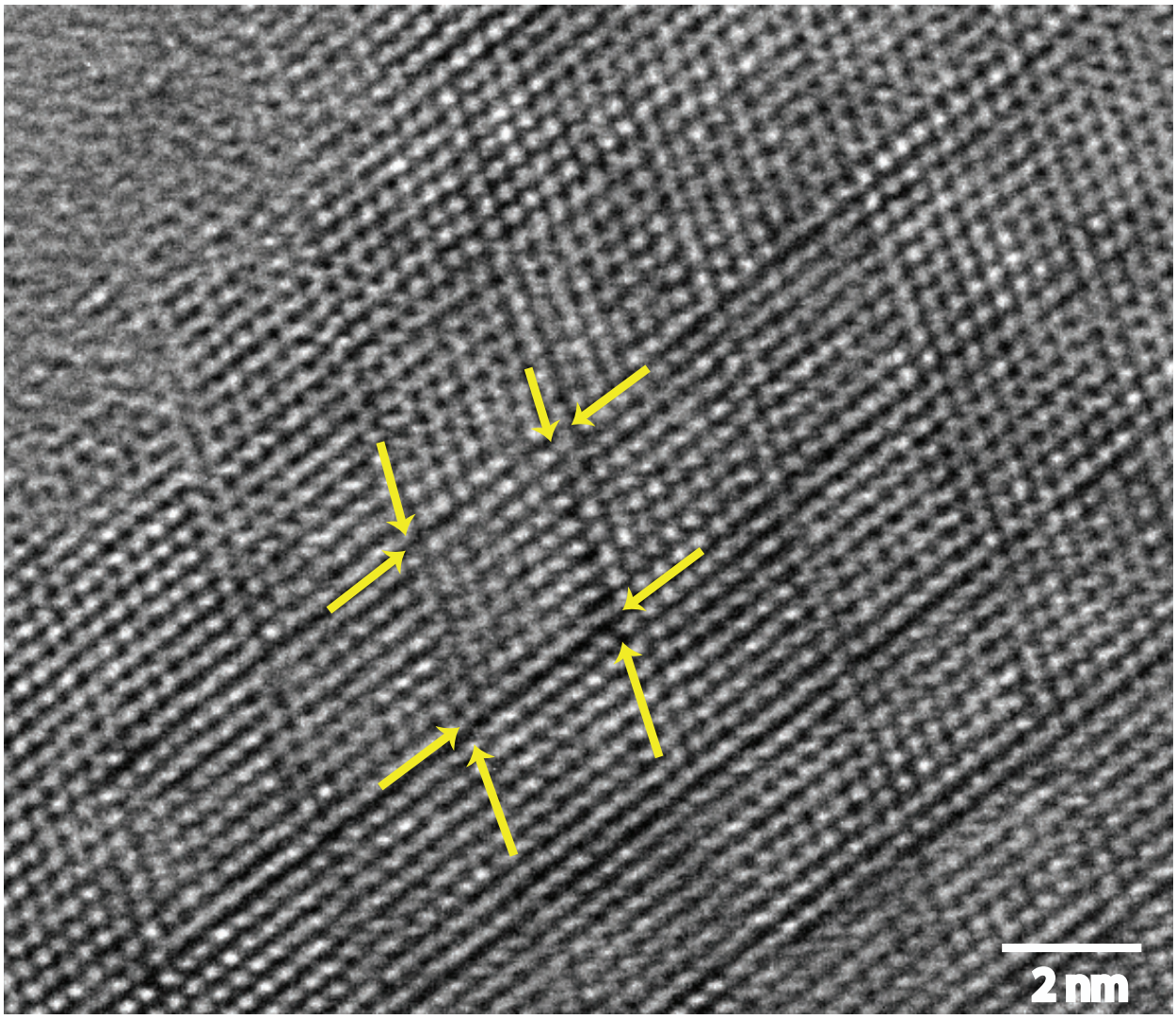

Figure 6.5: TEM dark field image in the [110] zone axis showing a two-dimensional vacancy superstructures represented by a periodic dark line contrast that propagates in <111> directions.

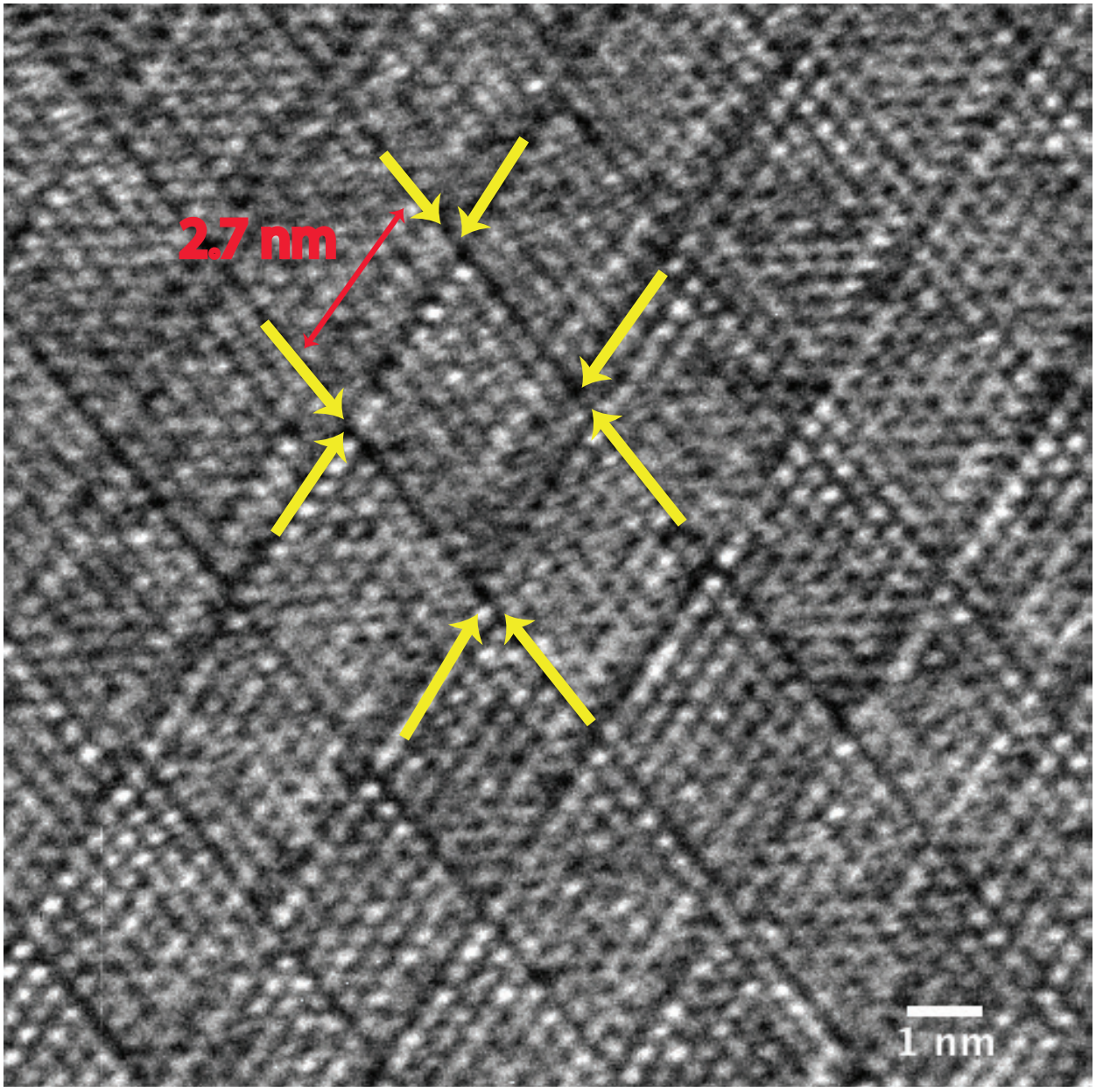

Figure 6.6: TEM image from Figure 6.5 at higher magnification. Here, the periodicity of the two-dimensional vacancy structures is measured to be ≈ 2.7 nm.

Information along the two-dimensional vacancy superstructures (i.e. the dark streaks observed in the TEM images) remains scarce. Consequentially, an attempt is made to probe the atomic environment in the vicinity of these superstructures by utilizing the HAADF-STEM capabilities of the TEAM I microscope. Preliminary bright field imaging in the [110] zone axis on an as-grown Ga_2SeTe_2 is shown in Figure 6.7. Here, the two-dimensional vacancy structures are observed as a bright line contrast that propagates in <111> directions. Unlike the 735 °C annealed sample, the vacancy structures occur randomly through the Ga_2SeTe_2 lattice. Closer examination around the vacancy structures reveal an apparent atomic dumbbell inversion. To observed this effect more directly, HAADF-STEM imaging is utilized.

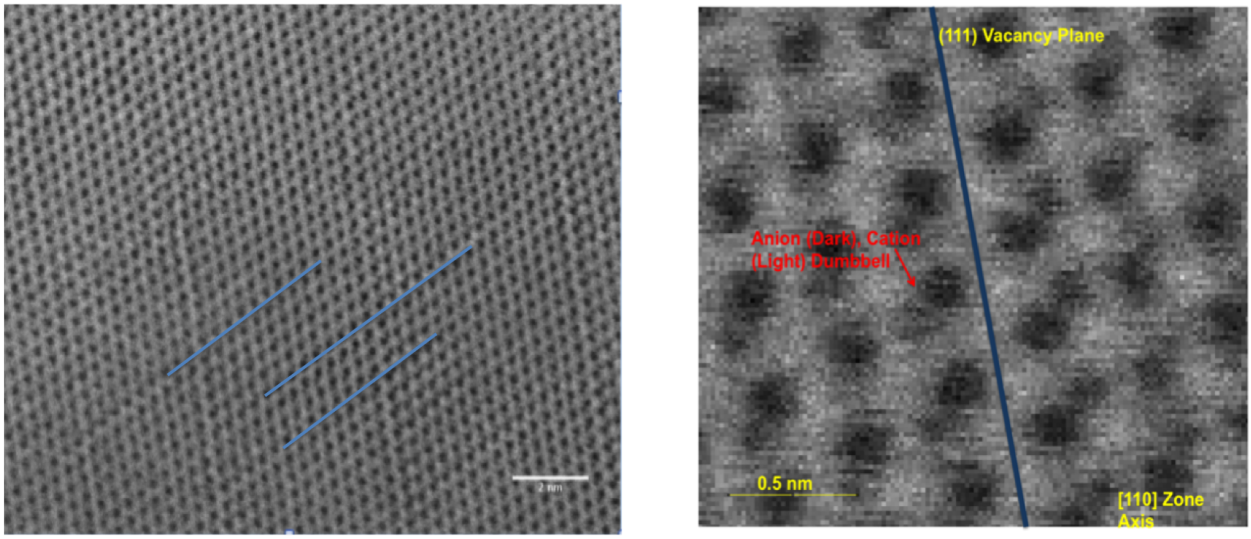

Figure 6.7: Bright field STEM images of as as-grown Ga2SeTe2 single crystal at 300 kV in the [110] zone axis, where the blue lines highlight the two-dimensional vacancy structures that lack a defined periodicity. The magnified image suggests an atomic dumbbell inversion across the two-dimensional vacancy structures.

Figure 6.8 shows the atomic columns of Ga_2SeTe_2 crystal with ordered two-dimensional vacancies (i.e. 735 °C annealed) along a [110] projection. As expected from earlier TEM images (Figures 6.5 and 6.6) and prior reports in the literature, a periodic contrast variation in the form of dark lines that are parallel to both sets of {111} planes visible in edge-on orientation along this zone axis is observed. The inset Fourier transform of this image confirms the symmetry of atomic column stacking consistent with the face-centered cubic Bravais lattice associated with a zincblende crystal structure (Figure 6.14) and the periodicity of the two-dimensional vacancy ordering. The latter is evidenced by the fine spots at 1/8 the spacing of the {111} planes ($\approx$ 2.7 nm) along both <111> reciprocal lattice directions in this projection.

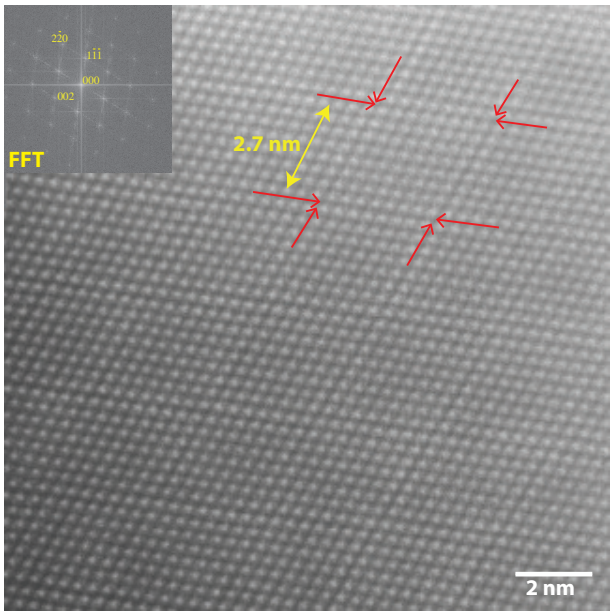

Figure 6.8: HAADF-STEM image of bulk single crystal Ga_2SeTe_2 in the [110] zone axis, which reveals a periodic dark line contrast every eight {111} planes (arrowed). These planes contain a high concentration of vacancies arrayed in the highly ordered and self-assembled configuration displayed here.

A magnified image of the Ga_2SeTe_2 crystal in the [101] zone axis is shown in Figure 6.9. Here, one is able to discern the cation-anion dumbbells that are expected in the zincblende lattice when viewed along the [101] projection; the dumbbells are also oriented perpendicular to the long axis created by the $20\bar{2}$ reflection in reciprocal space (Figure 6.9 inset), which is the expected cation-anion orientation along <110> projections. Based on the conventional mechanism of Z-contrast, the brighter spots represent the higher-Z anions (Te or Se) and the dimmer spots represent the lower-Z cation (Ga) sites. The dumbbell distance is ≈ 0.147 nm in agreement with the predicted value. Additionally, the pervasiveness of {111} vacancy ordering in the zincblende structure is confirmed by tilting the Ga_2SeTe_2 crystal to the [121] zone axis and collecting a dark field image (Figure 6.10). Consistent with their structural arrangement evident in <110> zone axes, the modulation of vacancy-ordered {111} planes is again repeated at 2.7 nm intervals. However, spatially resolving both cation and anion sites (≈ 0.085 nm) along <211> zone axes is difficult due to deleterious effects arising from specimen thickness—where it is $\approx 15\%$ greater than <110> zone axes thicknesses—and an amorphous layer that covers the crystal, which was difficult to remove.

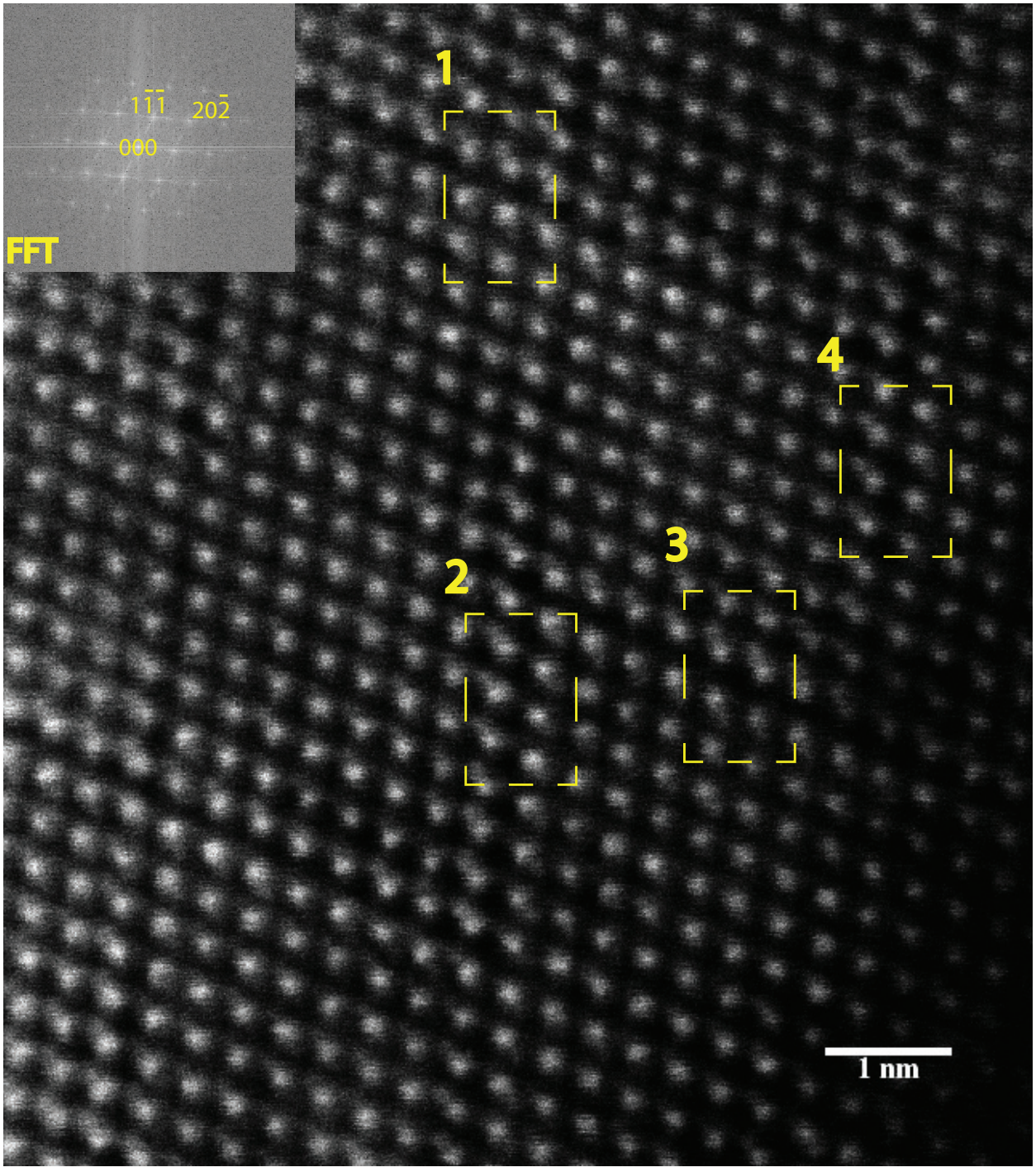

Figure 6.9: HAADF-STEM image of bulk single crystal Ga_2SeTe_2 in the [101] zone axis at atomic resolution. As highlighted by the four regions, we observed cation-anion dumbbell inversions at both orientations of {111} planes across the two-dimensional vacancy structures.

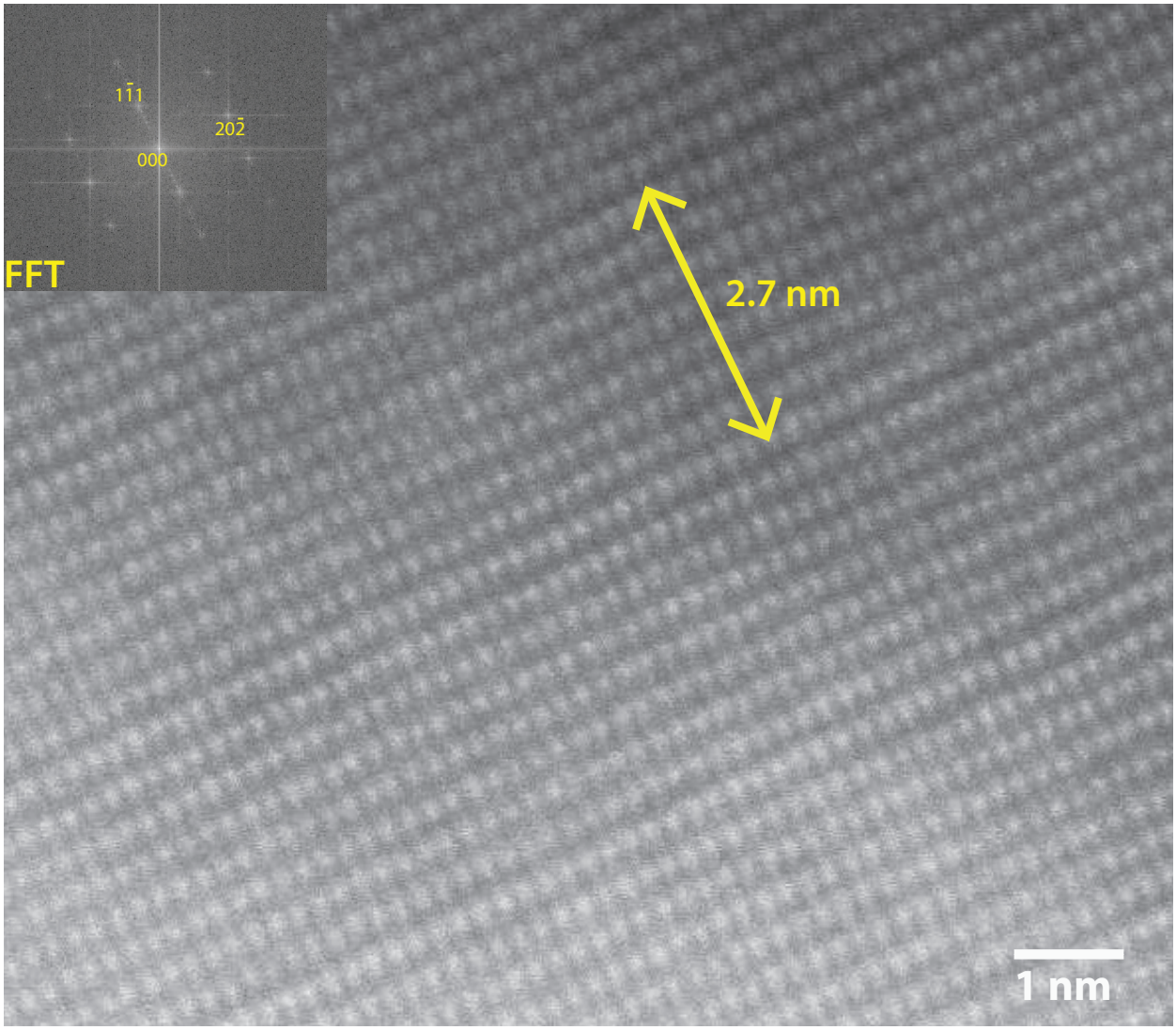

Figure 6.10: HAADF-STEM image of 735 °C annealed bulk single crystal Ga_2SeTe_2 oriented in the [121] zone axis and its corresponding reciprocal space (inset).

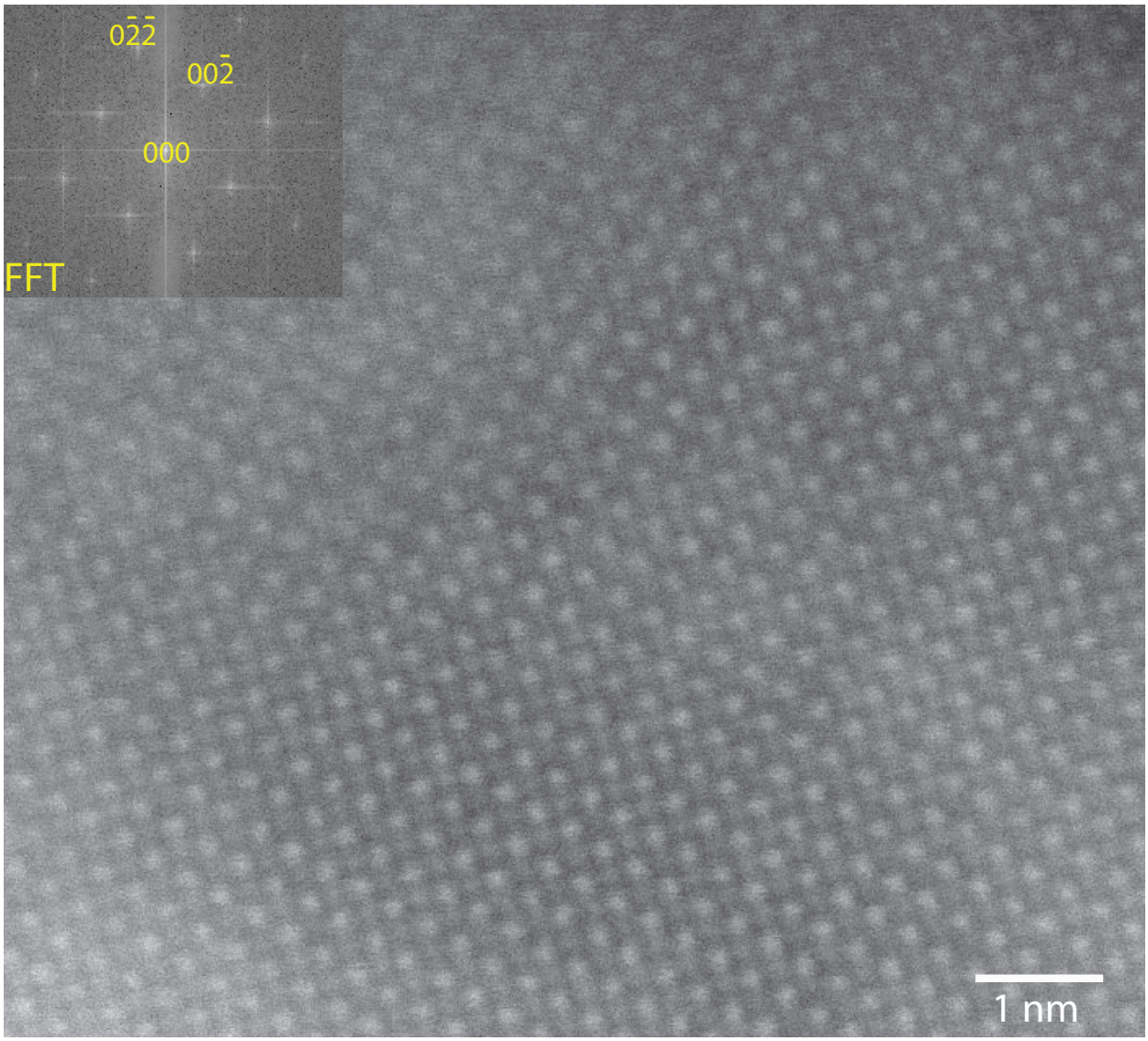

Figure 6.11: HAADF-STEM image of 735 °C annealed bulk single crystal Ga_2SeTe_2 oriented in the [100] zone axis and its corresponding reciprocal space (inset).

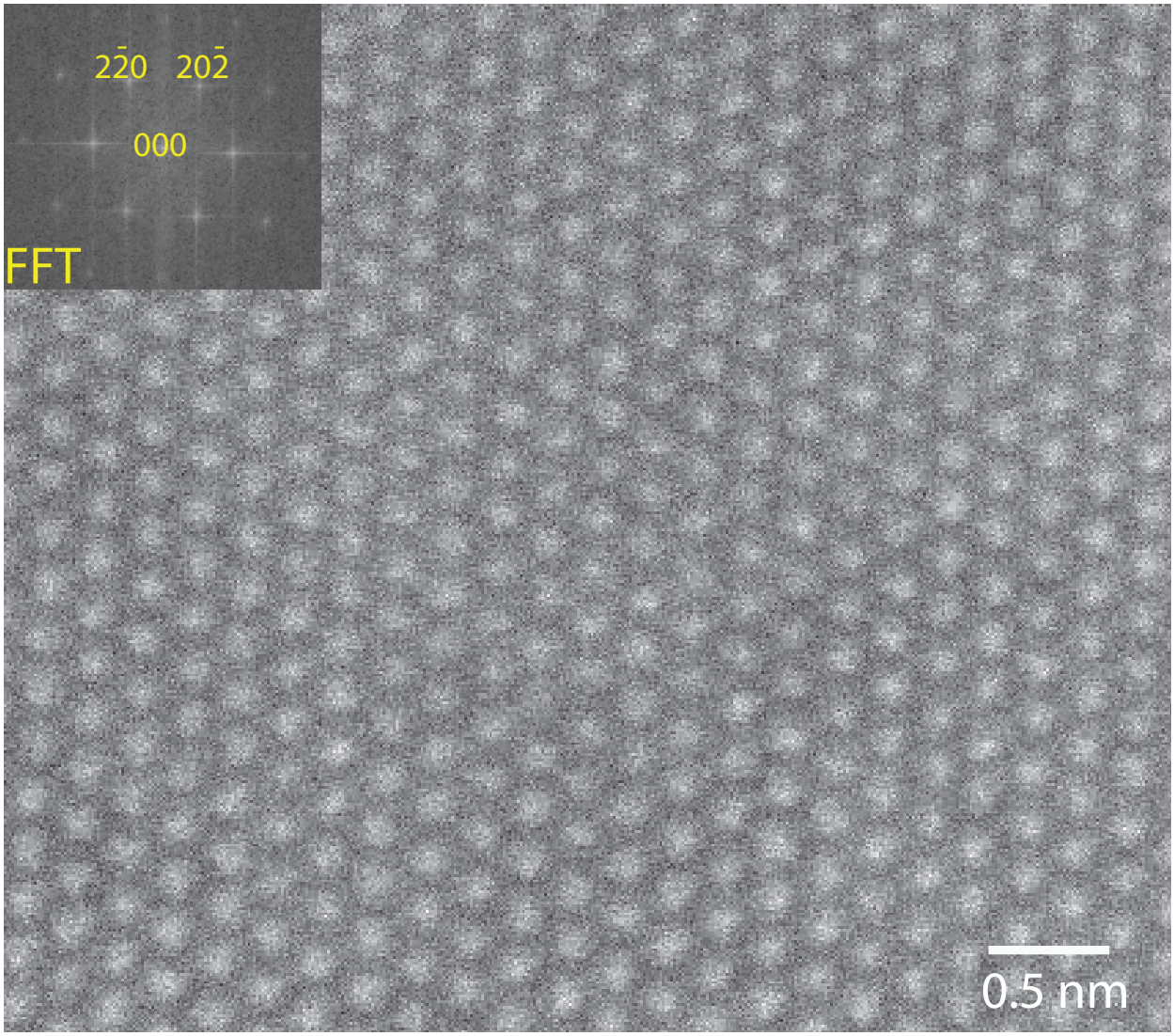

Figure 6.12: HAADF-STEM image of 735 °C annealed bulk single crystal Ga_2SeTe_2 oriented in the [111] zone axis and its corresponding reciprocal space (inset).

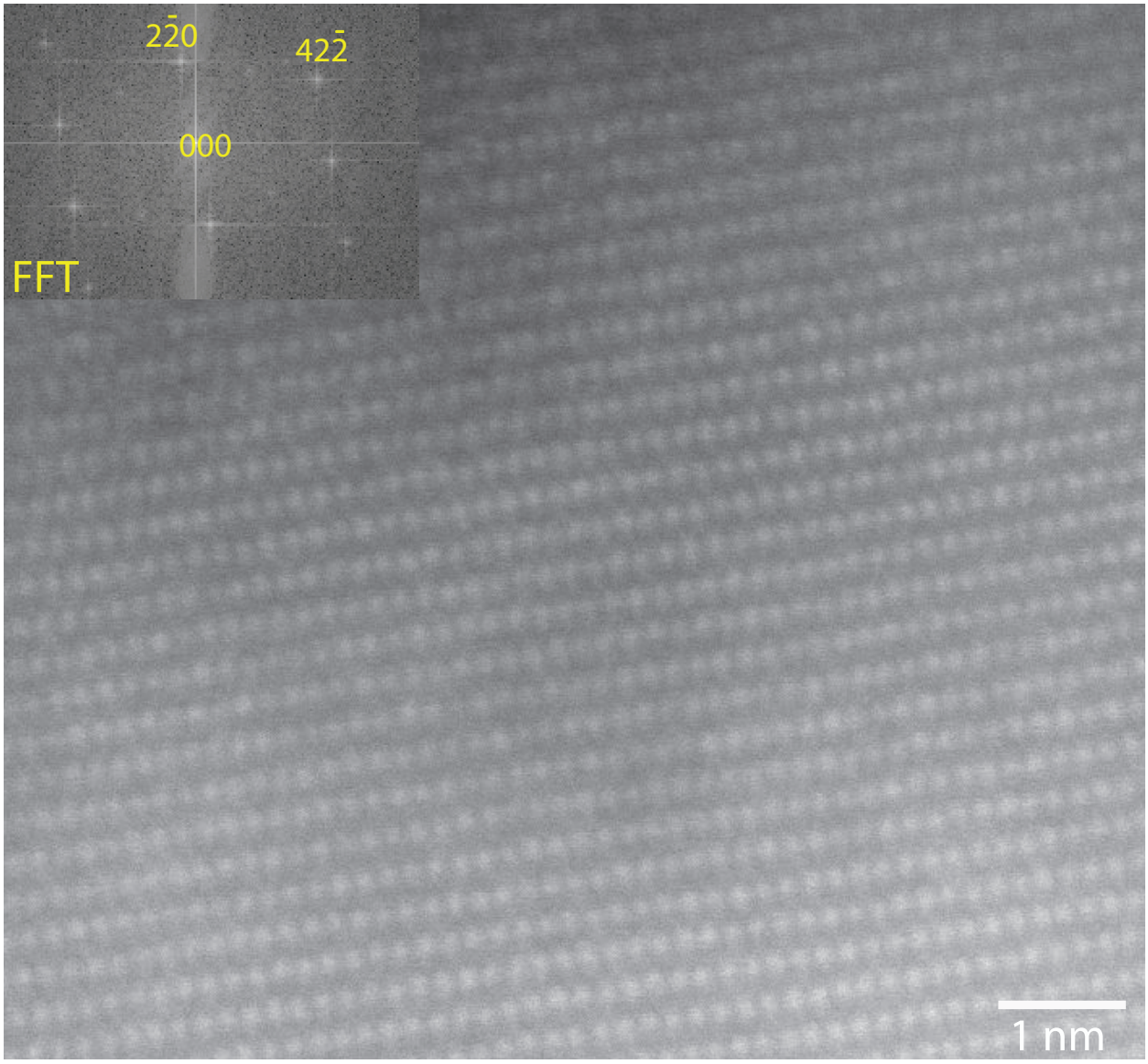

Figure 6.13: HAADF-STEM image of 735 °C annealed bulk single crystal Ga_2SeTe_2 oriented in the [113] zone axis and its corresponding reciprocal space (inset).

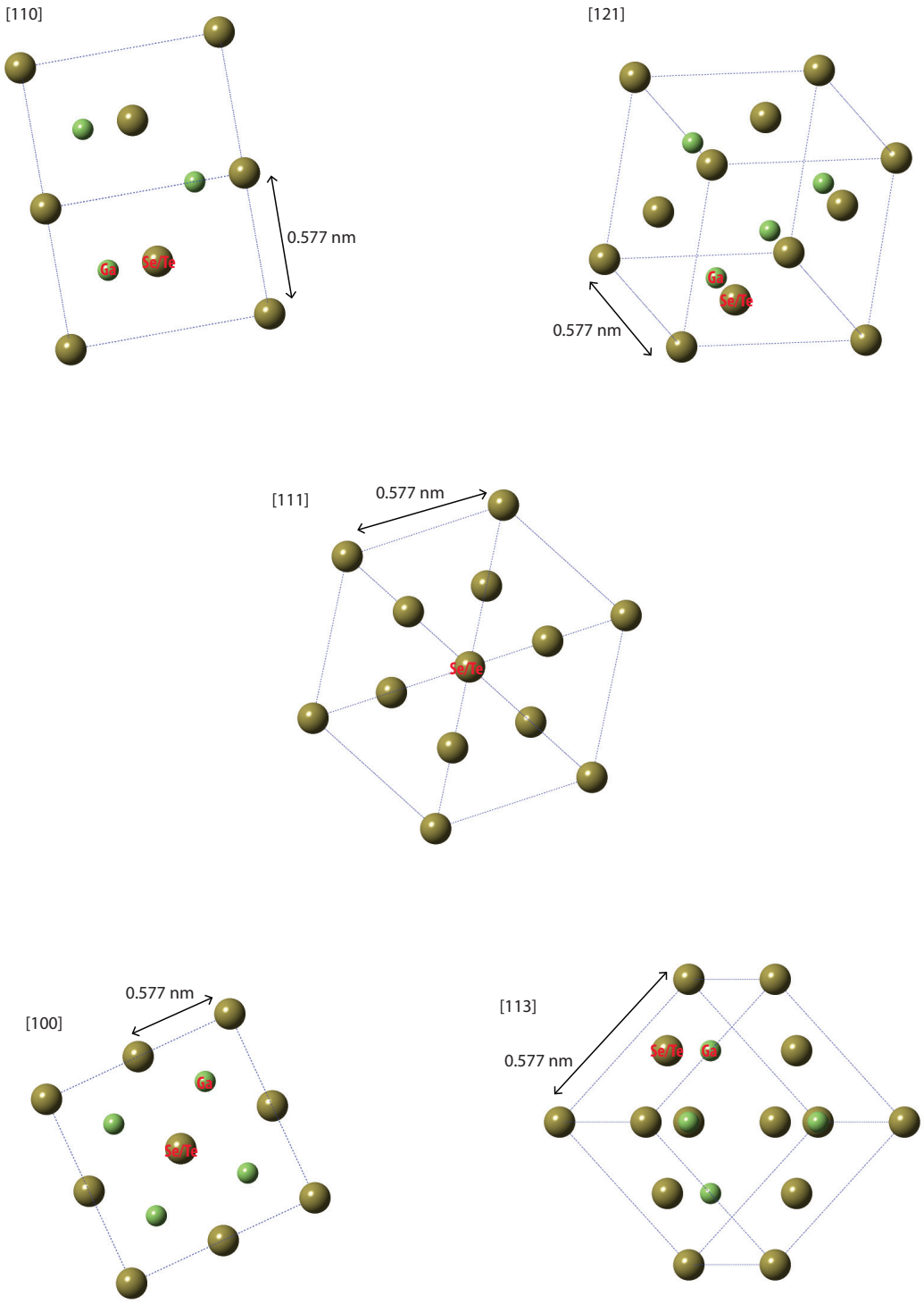

Figure 6.14: Schematic of the atomic column stacking in a Ga_2SeTe_2 crystal viewed in the [110], [121], [111], [100], and [113] zone axes.

The Ga_2SeTe_2 crystal was also tilted to <100>, <111>, and <113> zone axes orientations (Figures 6.11–6.13). At these orientations, the atomic column stacking remain consistent with the face-centered cubic Bravais lattice associated with a zincblende crystal structure (Figure 6.14). Thickness effects (similar to those discussed for the [121] zone axis) were encountered in <113> zone axes that hindered the ability to spatially resolve the atomic structure. Instead the symmetry was confirmed by its corresponding reciprocal space (shown in the inset of Figure 6.14). What is important to note here is that the vacancy based superstructure is absent at these orientations. This indicates the the two-dimensional vacancy structure in Ga_2SeTe_2 exists solely in {111} planar orientations.

Examining the image detail in Figure 6.9 more carefully, one notices that the dumbbell orientation in <110> zone axes projections is inverted across vacancy-ordered planes in a manner analogous to an inversion twin boundary (as was seen in the bright field image in Figure 6.9). Four yellow boxes in Figure 6.9 highlight such inversions. The dumbbell inversion is constant within each domain bounded by the ordered vacancy-rich {111} planes. This illustrates a key feature of Ga_2SeTe_2 and its related compounds: native defect structures in these materials distort the local symmetry of the motif assigned to each lattice point, but the global symmetry of the Bravais lattice is preserved. This is captured in the STEM images, and confirmed by their inset Fourier transforms.

The mechanism driving the cation-anion dumbbell inversion across the vacancy-rich planes Ga_2SeTe_2 remains uncertain. The regular periodicity of this effect, however, suggests that the observed symmetry inversions are electronic in nature. Earlier x-ray investigations on Ga_2Te_3 have proposed that Ga vacancies may induce Jahn-Teller crystal distortions, where it was argued that unattached Te orbitals initiate a tetragonal distortion from the original cubic arrangement.[31–33] The spatially-resolved structural microscopy presented here, cannot confirm the mechanism driving the observed local distortions.

6.4 Conclusions

The electron microscopy investigation of Ga_2SeTe_2 presented in this chapter serves as an example of a direct observation of the effect of native point defects on local structure. The results show no detectable distortion in the lattice spanning the regularly periodic {111} planes along which vacancy ordering is concentrated; however an inversion in the cation-anion orientation vector across those planes is observed, suggesting an electronic interaction at play. Nevertheless, the high spatial resolution methods discussed have revealed new information on the interplay between the two-dimensional vacancy structures in Ga_2SeTe_2 and its local structure. Such observations are important in developing further understanding of the technological potential of Ga_2SeTe_2 and its related compounds.

Chapter 7

Positron Annihilation Spectroscopy

7.1 Introduction

In this chapter, positron annihilation spectroscopy experiments on $Ga_2(Se_{1-x}Te_x)_3$ crystals is presented. Defects such as vacancies or precipitates may be identified in a sample by measuring the lifetimes and momenta of the injected positrons. As $Ga_2(Se_{1-x}Te_x)_3$ is a compound with a large concentration of intrinsic stoichiometric vacancies which have the possibility of redistribution via ordering, it may fruitful to investigate positron annihilation in these materials.

7.2 Experimental Setup

Positron lifetime and coincidence Doppler broadening (i.e. electron momentum) measurements were carried out on $Ga_2(Se_{1-x}Te_x)_3$ samples for x ranging from 0.7 to 1.0. Measuring positron lifetime and sample electron momentum allows one to identify defects and probe their sizes/concentrations. The specific details of carrying out such measurements have been previously reported.[81–83] A ^{22}Na source (decay scheme shown in Figure 7.1), in water solution form, is used to inject positrons into $Ga_2(Se_{1-x}Te_x)_3$ crystals with dimensions $\approx$ 2 mm $\times$ 2 mm $\times$ 1 mm. The ^{22}Na source solution is deposited on the crystal sample using a pipet. The total positron activity on the sample is $\approx$ 20 to 30 μCi. The sample was in a souce-sample sandwich geometry, where a second $Ga_2(Se_{1-x}Te_x)_3$ crystal is placed on the now radioactive sample, where the two samples are then wrapped in ultra thin aluminum foil. The addition of a second sample increases the intensity of collected annihilation photons. Positrons that annihilate in the sample have thermal energies, where thermalization in the sample is of the order of 100 μm.[81] Lifetime measurements involve a coincidence setup of two BaF_2 detectors (shown in Figure 7.2) to measure the time difference between the 1.27 MeV de-excitation gamma ray coming from the ^{22}Na source, and the 511 keV gamma ray originating from positron annihilation in the sample. Coincidence Doppler broadening measurements observe the red/blue shifts of the annihilation photons using Ge detectors; with this information the electron momentum can then be probed via energy and momentum conservation.

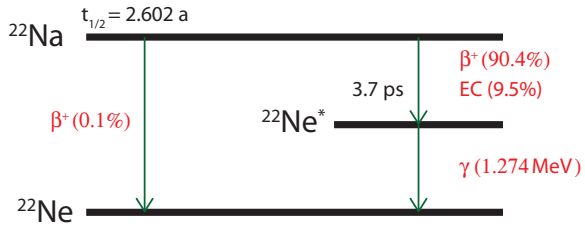

Figure 7.1: Decay scheme for ^{22}Na.

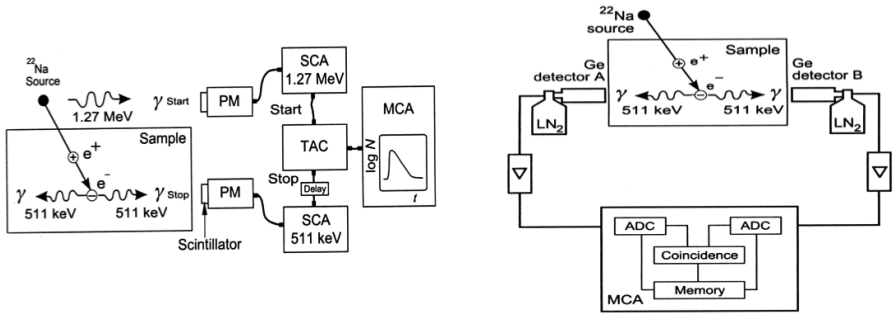

Figure 7.2: Basic setup of a positron annihilation spectroscopy experiment as reproduced from Krause-Rehberg and Leipner.[81] The left diagram depicts a coincidence positron lifetime measurement, while the right depicts a coincidence Doppler broadening measurements.

7.3 Results and Discussion

Positron lifetime values are extracted by convolving the theoretical time-dependent positron decay spectrum ($D(t)$) with a time resolution function $F_{\mathrm{t}}(t)$.[81] The convolved decay spectrum, ($D_{\mathrm{f}}(t)$) can be mathematically stated as

$$D_{\mathrm{f}}(t) = \int_{-\infty}^{\infty} D(t-t')F_{\mathrm{t}}(t')\mathrm{d}t'. \tag{7.1}$$

In common practice, the time resolution function $F_{\mathrm{t}}(t)$ is represented as a single Gaussian function. If that is the case, then the convolved decay spectrum has the form[81]

$$D_{\mathrm{f}}(t) = \sum_{i=1}^{k+1} \exp\left[-\frac{t-t_0-\sigma_{\mathrm{s}}^2/(4\tau_i)}{\tau_i}\right]\left[1-\mathrm{erf}\left(\frac{1}{2\sigma_{\mathrm{s}}\tau_i}-\frac{t-t_0}{\sigma_{\mathrm{s}}}\right)\right], \tag{7.2}$$

where t is the time, t_0 is the time shifted via delay cable, σ_{s} is the standard deviation of the time resolution function, I_i are the component intensities, and τ_i are the component lifetimes. An illustration of the fitting process is shown in Figure 7.3. Here a two component model is fitted to the decay spectra of Ga_2Te_3 (red circles) and Ga_2SeTe_2 (blue circles). For Ga_2Te_3 positron lifetimes of 277 ps (at 44.5% intensity) and 463 ps (at 55.4 % intensity) are extracted. For Ga_2SeTe_2, positron lifetimes of 347 ps (at 91.4% intensity) and 683 ps (at 8.6 % intensity) are extracted. Averaging these lifetime components gives a positron lifetime of $\approx$ 380 ps for both compounds.

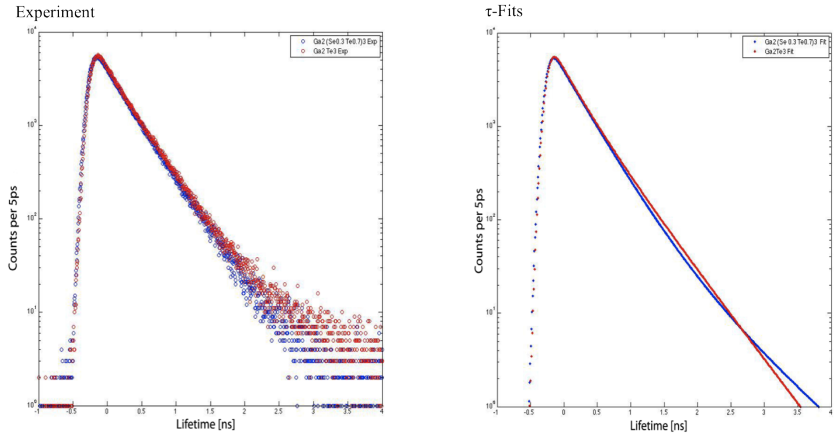

Figure 7.3: Experimental and fitted positron decay spectrums for Ga_2Te_3 (red) and Ga_2SeTe_2 (blue).

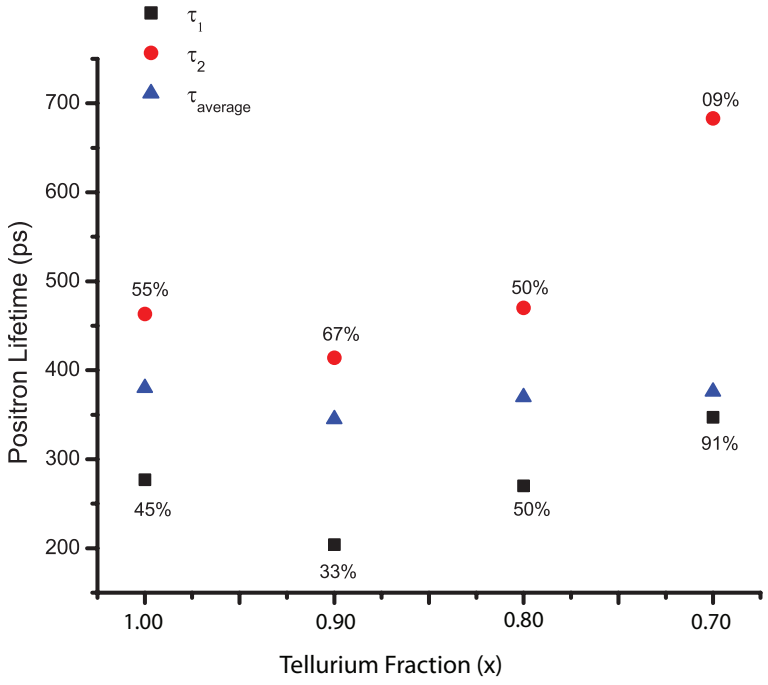

Figure 7.4: Positron lifetimes of $Ga_2(Se_{1-x}Te_x)_3$ (computed via a two-lifetime component model) as a function of tellurium atom fraction with the intensities of each lifetime component. The first lifetime component is denoted by τ_1, the second lifetime component by τ_2, and the average lifetime component by τ_{average}.

Figure 7.4 shows the average positron lifetime (computed by fitting a two component lifetime model to the experimental positron decay spectrum) as a function of tellurium atomic fraction for four $Ga_2(Se_{1-x}Te_x)_3$ samples. Positrons in all of the samples had an average lifetime of ≈350 to 400 ps, indicative of a strong presence of defects (bulk annihilation lifetime for common semiconductors is on the order of ≈200 ps[81]). This is also evidenced by the observation that all of the samples had a dominant second lifetime component (nominally associated with defects), with the exception of the sample with $x = 0.7$ which had a fairly large 347 ps first lifetime component (possibly related to a highly prominent defect).

Figure 7.5 shows the results from coincidence Doppler broadening experiments measuring electron momentum in $Ga_2(Se_{1-x}Te_x)_3$, with tellurium atom fractions ranging from 0.7 to 1.0. Analyzing electron momenta in bulk $Ga_2(Se_{1-x}Te_x)_3$ relative to the electron momentum distribution measured for elemental tellurium can give insight on the type of defect that is dominant in each specimen. Large intensities of low electron momenta (0 to $\approx 0.03 m_e c$) are observed (m_e is the electron rest mass and c is the speed of light); after $\approx 0.03 m_e c$ electron momentum intensities drop. A similar trend is observed when the data are normalized relative to elemental gallium and selenium. Such behavior suggests that positrons are not annihilating at single gallium, tellurium, or selenium vacancies, but at larger open-volume defects such as vacancy clusters or voids where the overall electron density is low and low-momentum valence electrons dominate.

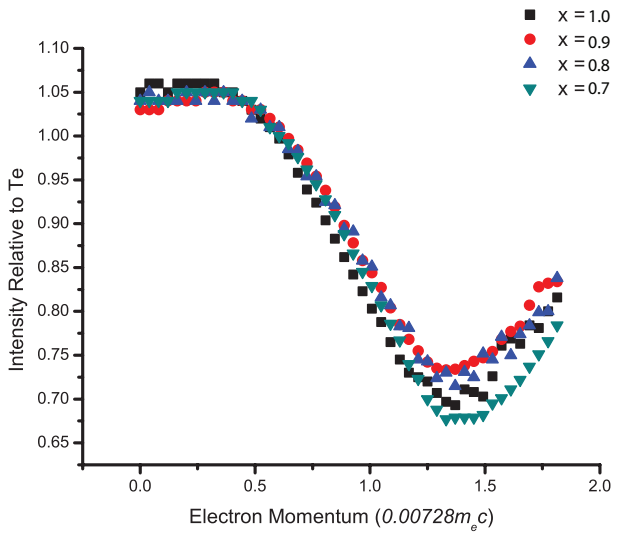

Figure 7.5: Electron momentum distributions for $Ga_2(Se_{1-x}Te_x)_3$ samples with tellurium atomic fraction ranging from 0.7 to 1.0.

Table 7.1: Positron lifetimes of $Ga_2(Se_{1-x}Te_x)_3$ semiconductors. Intensities for each component is shown in parentheses.

Sample	τ_1 [ps] (Intensity [%])	τ_2 [ps] (Intensity [%])	τ_{average} [ps]
Ga_2Te_3	277 (44.5)	463 (55.5)	380.2
$Ga_2(Se_{0.1}Te_{0.9})_3$	204 (33.0)	414 (67.0)	344.7
$Ga_2(Se_{0.2}Te_{0.8})_3$	270 (50.0)	470 (50.0)	370.0
$Ga_2(Se_{0.3}Te_{0.7})_3$	200 (32.8)	431 (67.2)	355.2
$Ga_2(Se_{0.3}Te_{0.7})_3$ (ordered vacancy)	274.4 (74.5)	672.8 (25.5)	378.0

Positron lifetime measurements have been carried out on an annealed (735 °C for two weeks then quenched to 0 °C) polycrystalline Ga_2SeTe_2 sample. Looking at average lifetimes, the results are similar to previous as-grown $Ga_2(Se_{1-x}Te_x)_3$ samples (see Table 7.1). The main difference in the annealed sample is that the first lifetime component (nominally associated with bulk lifetime) is the dominant component. A bulk lifetime of $\approx$ 270 ps is similar to that of HgTe (274 ps) and CdTe (280 ps).[81] These results indicate that when the structural vacancies in Ga_2SeTe_2 order, their role in positron trapping diminishes.

7.4 Conclusions

Positron annihilation investigations on as-grown $Ga_2(Se_{1-x}Te_x)_3$ for x ranging from 0.7 to 1.0 show long positron lifetimes that reveal a proclivity for vacancy cluster formations. This is not surprising, as two-dimensional vacancy structures in as-grown $Ga_2(Se_{1-x}Te_x)_3$ are randomly distributed in the structure. Hence, an injected positron would likely see the vacancy structures in a manner similar to large clusters or voids. This is further evidenced by coincidence Doppler broadening measurements, where large intensities of low electron momenta were observed. Measuring the positron lifetime on Ga_2SeTe_2 with ordered vacancies (via the 735 °C annealing treatment) shows that the average positron lifetime remains unchanged, however the majority of lifetime component appears to originate from the bulk. This indicates that as the two-dimensional vacancy structures order, their tendency for positron trapping diminishes.

Chapter 8

Material Properties

8.1 Introduction

In this chapter, the effect of vacancy ordering observed in Ga_2SeTe_2 on material properties is investigated. First, the relationship between vacancy ordering and material electronic structure is investigate by measuring the band gaps of as-grown and annealed Ga_2SeTe_2 single crystals via optical absorption methods. Second, Hall effect measurements are used to to probe the effects of vacancy ordering on the electrical transport properties of as-grown and annealed Ga_2SeTe_2 crystals.

8.2 Band Gap Measurements

The band gap of a material may be measured through optical means. Generally, this involves an experimental setup where light is incident on a slab of material and the transmitted and reflected light is collected (as depicted in Figure 8.1a). As light propagates through a medium, phenomena such as scattering, refraction, and absorption may occur. If the incoming light has an energy greater than the band gap of the medium it will be fully absorbed into the material via an excitation from the valence band to the conduction band (Figure 8.1b). Hence, the band gap of any given material may be measured by observing the rise in absorption in the light spectrum. Additionally, impurities in the medium that create energy levels between the conduction and valence bands can be identified by their respective emission lines in absorption spectra.

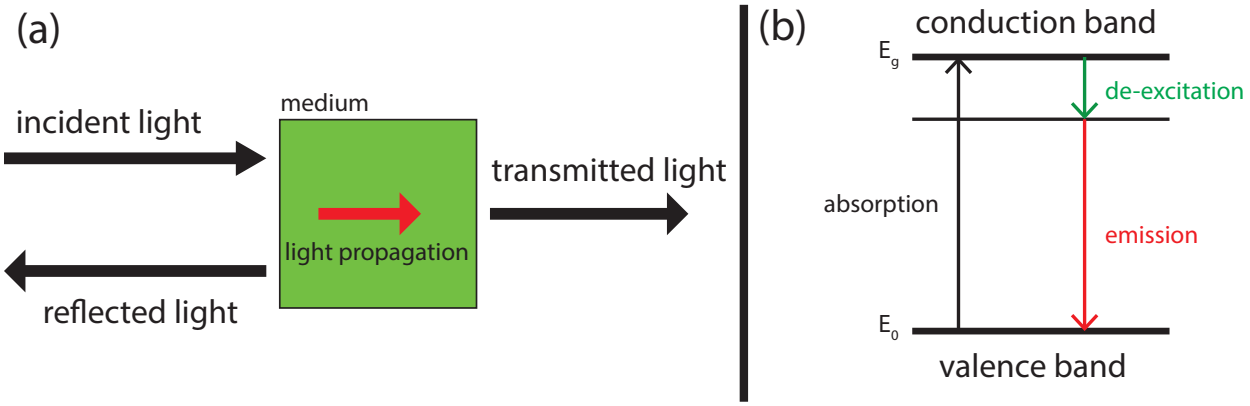

Figure 8.1: (a) Representation of light incident on a material. The light can reflect, propagate, or transmit through the medium. As light propagates in the medium, various phenomena can occur that include scattering, absorption, absorption-luminescence, and refraction. (b) Energy diagram depicting the absorption process in a material. Incident light with energies larger than the band gap may be absorbed into the conduction band. Relaxation from the conduction band my also occur which results in luminescence after absorption.

The absorption coefficient (α) of a material, which quantifies the absorption of light, can be computed by first determining its coefficients of reflection and transmission—otherwise known as reflectivity (R) and transmissivity (T). Generally, reflectivity is defined as the ratio of the reflected light intensity to the incident light intensity and transmissivity is defined as the ratio of transmitted light intensity to the incident light intensity. If absorption and scattering effects from the medium are neglected then the summation of reflectivity and transmissivity must be unity (i.e. R+T=1). The intensity gradient of light passing through a material with thickness t can be written as

$$\mathrm{d}I = -\alpha \mathrm{d}t I(t), \tag{8.1}$$

where $\mathrm{d}I$ is the incremental decrease in intensity as light propagates through an incremental distance $\mathrm{d}t$ in the material. Integrating this expression gives the Beer-Lambert law:

$$I(t) = I_0 \exp(-\alpha t), \tag{8.2}$$

where I_0 is the intensity of light incident on the material and $I(t)$ is the intensity of light in the material at t. In realistic experimental conditions, the coherence length of the incident light is larger than the material thickness. This gives rise to fringes caused by the interference of the incident light waves.[84] If one assumes that the material of interest has surfaces with equivalent reflectivity coefficients, then optical transmission can be written as

$$T = \frac{(1-R)^2 \exp(-\alpha t)}{1 - 2R\exp(-\alpha t)\cos(\Phi) + R^2 \exp(-2\alpha t)}, \tag{8.3}$$

where Φ represents the phase shift of light as it passes from one surface of the material to the other.[84] Most semiconductor materials are strongly absorbing media ($\alpha t \gg 1$), therefore, phenomena arising from multiple reflections can be neglected. Equation (8.3) then reduces to

$$T \approx (1-R^2)\exp(-\alpha t), \tag{8.4}$$

where the quantity (1-R^2) quantifies the transmission of the front and back surfaces of the material and the exponential term accounts for the decrease in light intensity as predicted by the Beer-Lambert law.[84] From this, the absorption coefficient for a sample with thickness t is computed via the expression

$$\alpha = -\frac{1}{t}\ln\left[\frac{T}{(1-R)^2}\right]. \tag{8.5}$$

It then follows that to determin the absorption coefficient for any given sample, one must simply collect its reflectivity and transmissivity spectra. However, one must note that the derivations presented here ignore extraneous absorption and scattering in the sample. In a real sample, these effects are always present. To minimize such effects, samples are usually highly polished, to minimize surface scattering, and are relatively thin (100 μm to 500 μm) to minimize absorption effects.

8.2.1 Experimental Setup

Optical reflectivity and transmissivity measurements on $Ga_2(Se_xTe_{1-x})_3$ single crystals were preformed using a Perkin-Elmer 950 Lambda spectrophotometer. The instrument is equipped with halogen and deuterium lamps capable of light wavelengths ranging from 175 to 3300 nm. In the ultraviolet and visible spectra, which corresponds to 0.05 nm to 5.00 nm resolutions. In the near infrared, resolutions of 0.20 nm to 20 nm are possible. Single Ga_2SeTe_2 samples, ≈200 to 500 μm thick, were polished (polishing procedures described in Chapter 3)on both sides to ensure maximum optical transmission and reflection. Crystal were mounted onto the instrument sample holder using double sided plastic tape. The incident beam on the samples has a spot size of 1 mm. The majority of reflectivity measurements were carried out at wavelengths between 500 to 2600 nm, which corresponds to a light energy range from 0.5 to 2.5 eV. Light wavelength was toggled in 1 nm intervals with an integration time of 0.52 s. This gives a scan speed of 113.46 nm/m. Under these conditions, reflectivity and transmissivity spectra were collected. The absorption spectrum for each sample was then plotted using equation (8.5).

8.2.2 Results and Discussion

The first study to be carried out involves looking at the absorption coefficient of Ga_2SeTe_2 crystals as a function of vacancy ordering. This is done by plotting the absorption edges for as-grown, 435 °C annealed, and 735 °C annealed sample. First the as-grown crystal was measured.

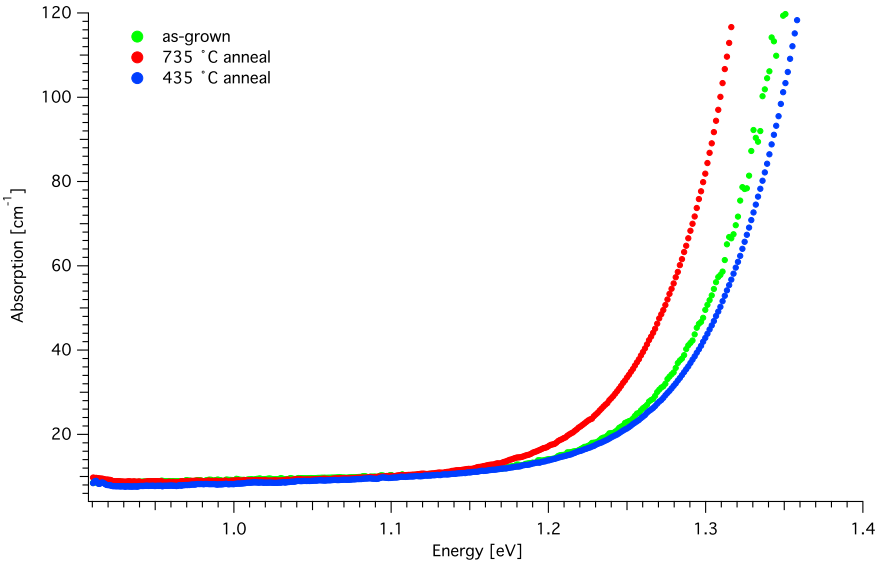

Figure 8.2: Absorption edges of as-grown, 435 °C annealed, and 735 °C annealed Ga_2SeTe_2 single crystals.

The same sample then underwent the 735°C annealing treatment to produce ordered two-dimensional vacancy structures and the absorption spectrum was then re-measured under identical conditions. Finally a Ga_2SeTe_2 single crystal under the 435 °C annealing treatment was measured. The results are shown in Figure 8.2, where the absorption coefficient is plotted on an energy scale.The as-grown and 435 °C sample have a band gap of 1.27 eV. As the vacancies in Ga_2SeTe_2 become fully ordered (via the 735 °C annealing treatment), the band gap of Ga_2SeTe_2 is driven down to 1.22 eV. The change of band gap gap is slight (0.05 eV) though reproducible, and is an adumbration of the local structural distortions observed via x-ray diffraction and electron microscopy. Nevertheless, it is a striking instance, where the electronic structure of a material is altered by intrinsic structural rearrangements (in this case vacancy ordering) as opposed to extrinsic means such as impurity doping.

Absorption edges for $Ga_2(Se_{1-x}Te_x)_3$ crystals with tellurium atom fractions ranging from 0.6 to 1.0 were also measured. The results are shown in Figure 8.3. Here, it is clear that as the concentration of selenium increases, the band gap of $Ga_2(Se_{1-x}Te_x)_3$ increases. This result is consistent with the common practice of alloying anions with higher electronegativity (like selenium) to increase the band gap of the material. In this case, the band gap rises from 1.08 eV at x=1.00 then to 1.15 eV at x=0.90 then to 1.20 eV at x=0.80 then to 1.27 eV at x=0.67, and finally to 1.30 eV at x=0.60. The resulting band gap curve in this stoichiometry region is nearly linear, with a slight tendency to be concave down. Crystals with lower tellurium concentrations were not measured (though this would help in determining the curvature of the band gap curve) as it is was difficult to synthesize their single phase compounds due to an immisciblity gap at high selenium concentrations (as fdiscussed in Chapter 3).

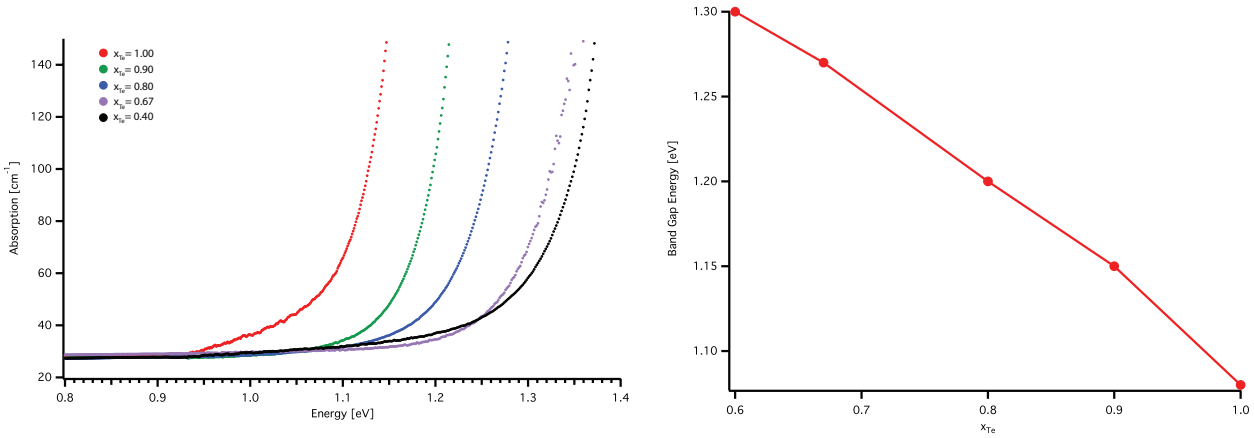

Figure 8.3: Absorption edges of as-grown $Ga_2(Se_{1-x}Te_x)_3$ for x=1.00, 0.90, 0.80, 0.67, and 0.60. The band gap curve as function of tellurium atom fraction is also shown.

8.3 Hall Effect Measurements

Hall effect measurements on as-grown and annealed Ga_2SeTe_2 single crystals can be carried out to probe the effects of vacancy ordering on charge carrier transport. In this measurement an electric field (E_x) is applied to a sample causing a current density (j_x) in the direction of the field to flow through it. A magnetic field (H) is then introduced that is perpendicular to the applied electric field. This magnetic field introduces a force (known as the Lorentz force) that deflects electron flow towards the -y direction (illustrated in Figure 8.4). This charge deflection causes an accumulation of charge in the $-y$ region of the sample and an electric field (E_y) is induced that counters the Lorentz force. The resulting force balance indicates that the charge current will only flow in the x direction. From this, two quantities may be directly measured.[2] The first is the Hall coefficient (R_H), which can be written as

$$R_H = \frac{E_y}{j_x H} = \frac{p\mu_h^2 - n\mu_e^2}{e(n\mu_e + p\mu_h)^2}, \tag{8.6}$$

where one can extract the material hole and electron carrier concentrations denoted by p and n respectively and e is the electron charge. The conductivity type of a material can be determined by the sign of the Hall coefficient: if R_H>0 the sample is p-type; if R_H<0 the sample is n-type. The resistivity (ρ) of the sample is simply defined as the ratio of the applied electric field and the current density, or

$$\rho = \frac{E_x}{j_x}. \tag{8.7}$$

With the Hall coefficient and resistivity known, the charge carrier mobility of the material (called the Hall mobility) is simply the ratio of the Hall coefficient and sample resistivity, or

$$\mu_H = \frac{|R_H|}{\rho}. \tag{8.8}$$

One must realize,however, that this treatment is purely theoretical; in most cases, sample geometry and the electrical contacts used to measure the sample play a crucial role in laboratory Hall effect experiments.

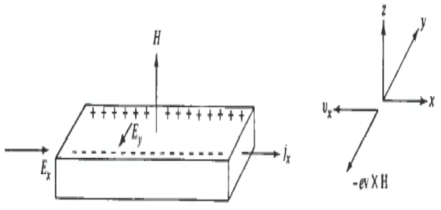

Figure 8.4: Representation of the Hall effect for sample with rectangular geometry as reproduced from Ashcroft and Mermin.[2]

The workhorse techniques to extract information of electrical properties of materials from Hall effect experiments were developed by van der Pauw.[85–87] The first requirement for successful van der Pauw Hall effect measurement require samples that adhere to van der Pauw geometries (examples are shown in Figure 8.5). The sample must have a symmetric geometry (e.g. circle or a square) with uniform thickness. It must also be singly connected, meaning there should not be any cracks present in the sample. Electric contacts to be deposited on the sample must be located at the circumference of the sample and should be as small as possible to prevent resistance effects from the contact material. Contacts must also be Ohmic, meaning charge can flow freely in the material from one direction to another. A general rule is that if an electric contact is 10% of the sample size, then the error introduced in the measurement will also correspond to 10%.

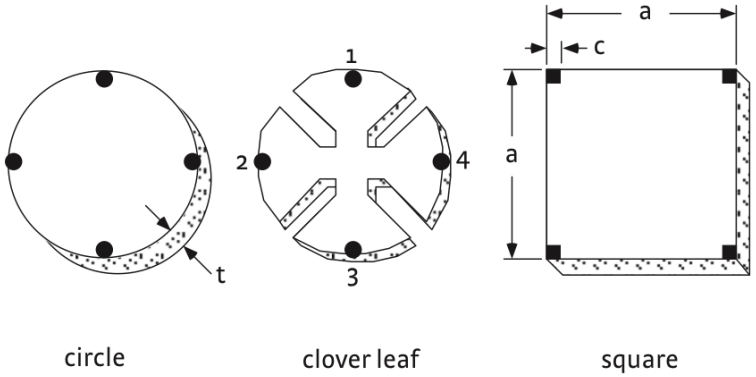

Figure 8.5: Common van der Pauw sample geometries as reproduced from van der Pauw.[85–87]

The most common van der Pauw geometries utilize a four-probe setup, where the current is read by two probes and voltage is measured by the other two. In this type of measurement, the resistances at the electrodes is first measured via Ohm's law:

$$R_{12,34} = \frac{V_{34}}{I_{12}}; R_{34,12} = \frac{V_{12}}{I_{34}}, \tag{8.9}$$

where, for example, $R_{12,34}$ is the resistance measured from the current originating from probes 1 and 2 (I_{12})and the voltage read from probes 3 and 4 (V_{34}). The resistances of the sample in the horizontal and vertical directions are then averaged,

$$R_{\text{vertical}} = \frac{R_{12,34} + R_{24,12} + R_{21,43} + R_{43,21}}{4} \tag{8.10}$$

$$R_{\text{horizontal}} = \frac{R_{23,41} + R_{41,23} + R_{32,14} + R_{14,32}}{4}. \tag{8.11}$$

The resistivity (ρ) of the sample is solved by substituting the vertical and horizontal resistance values into the van der Pauw formula:[85–87]

$$\exp\left(\frac{-\pi/R_{\text{vertical}}}{\rho}\right) + \exp\left(\frac{-\pi/R_{\text{horizontal}}}{\rho}\right) = 1. \tag{8.12}$$

If the sample is truly symmetric (i.e. R_{vertical}=$R_{\text{horizontal}}$), then the sample resistivity can be written as

$$\rho = \frac{\pi t R}{\ln(2)}, \tag{8.13}$$

where t is the sample thickness. The Hall voltage (V_H) is measured by averaging the voltage differences at the four probes measured at positive and negative magnetic fields, or

$$V_H = \frac{\Delta^{\text{P-N}} V_{13} + \Delta^{\text{P-N}} V_{24} + \Delta^{\text{P-N}} V_{31} + \Delta^{\text{P-N}} V_{42}}{8}, \tag{8.14}$$

where the quantity $\Delta^{\text{P-N}}$V denotes the difference of voltages measured at the magnetic field with positive and negative polarities. With this quantity now known, the sample charge carrier density (n_s) can be computed:

$$n_s = \frac{I_x H}{e|V_H|}, \tag{8.15}$$

where I_x is the applied current and e is the electron charge. Finally, the charge carrier mobility of the sample (in Hall effects this called the hall mobility denoted by μ_H) is given as

$$\mu_H = \frac{1}{e n_s \rho}. \tag{8.16}$$

Here, the Hall mobility denotes the mobility of the majority charge carrier. If the sample is n-type, then the measured Hall mobility would correspond to electrons and vice-versa.

8.3.1 Experimental Setup

Hall effect measurements on as-grown and annealed Ga_2SeTe_2 single crystals were carried out using a Lakeshore 7600 series Hall Effect Measurement System (shown in Figure 8.6). Naturally cleaved single crystal Ga_2SeTe_2 specimens had dimensions $\approx$ 2 mm $\times$ 2 mm $\times$ 1 mm. Samples were cut using a diamond wire saw to give sample shapes close to the van der Pauw geometries. A four-probe van der Pauw geometry (utilizing contacts made from silver paste) was implemented. The crystals were mounted onto circuit boards designed by lakeshore, where they were connected with gold wire to the Hall measurement system using Indium solder. Additionally circuit boards with tungsten probes were utilized to link the samples to the system. Measurements were done under a field of 1.0 T using excitations currents that ranged from 1 nA to 500 nA. The measurements were repeated on each crystals 10 to 250 times to ensure reproducibility. Sample resitivity and carrier mobility were computed from measured voltages and resistance in the method described in the previous sections.

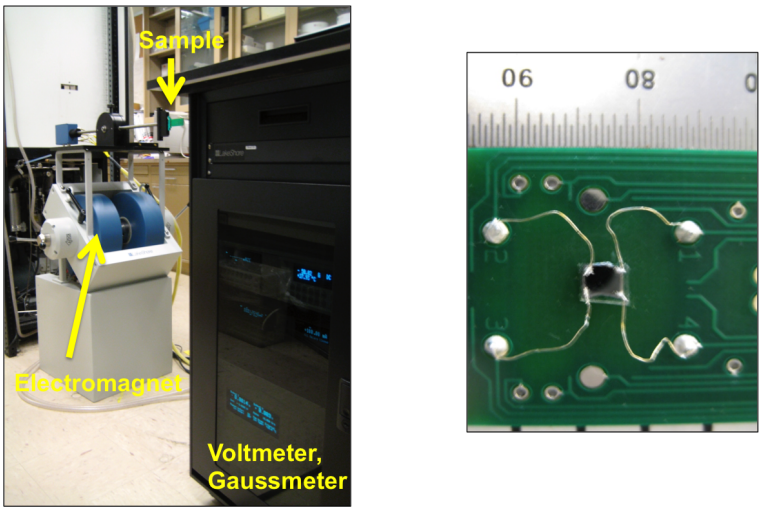

Figure 8.6: Lakeshore Hal effect measurement system is shown on the left. The right shows a Ga_2SeTe_2 crystal with contacts made from silver paster mounted on a circuit board for Hall effect experiments.

8.3.2 Results and Discussion

The initial experiments conducted involved measuring the relationship between applied current and measured voltage to ensure the contacts deposited on the Ga_2SeTe_2 single crystals were Ohmic. The results for a Ga_2SeTe_2 single crystal are shown in Figure 8.7. Here the measured voltages at probes 1 through 4 all showed nearly Ohmic behavior (i.e. $V{=}IR$) for an excitation current ranging from -500 nA to 500 nA. With this confirmed, one can move on and attempt to measure the resistivity and carrier mobilities of Ga_2SeTe_2 with different thermal histories. Subsequent measurements in the 1 nA range were also carried out and Ohmic behavior was also observed.

Electrical properties of Ga_2SeTe_2 obtained from Hall effect experiments are shown Table 8.1. Based on the optical absorption data, a decrease in resistivity for the 735 °C annealed (i.e. ordered vacancy) sample is expected as the band gap slightly decreases. However, the observed difference is quite drastic. The 435 °C sample had resistivity of 3.1 MΩcm, the as-grown had 0.71 MΩcm, and the 735 °C sample 0.028 MΩcm. Similarly, the 735 °C showed the highest carrier mobility (30 cm^2/Vs, n-type), when compared to the as-grown and 435 °C annealed samples. It would seem then that vacancy ordering improves electrical transport. If one remembers the discussion of Bloch electron waves from Chapter 1, the result would not be that surprising. As vacancies order, they cease to act as localized scattering centers and begin to cause constructive wave interference as the electron propagates through the crystal. If this is true, then it is a striking demonstration of drastically altering the material properties of a material through intrinsic structural transformations as opposed to extrinsic means. However, one must be cautious as there are other factors at play. Crystal

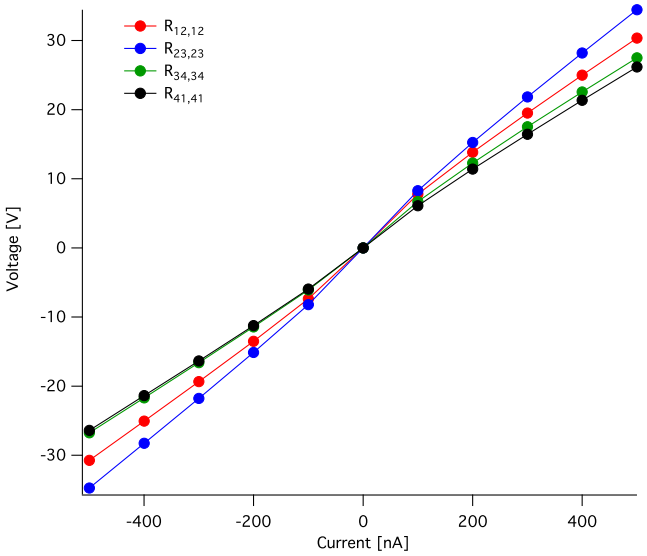

Figure 8.7: Applied current and voltage relationship for a Ga_2SeTe_2 single crystal with silver paste contacts.

quality can vary tremendously across a single ingot giving rise to varied electrical properties. Moreover, The large concentration of cation vacancies in Ga_2SeTe_2 causes it to be a highly compensated semiconductor, which makes Hall effect analysis difficult as there is not a clearly defined conductivity type.

Table 8.1: Electrical Properties of Ga_2SeTe_2

Thermal History	ρ [MΩcm]	Type	μ [cm^2/Vs]
As-grown	0.71	p	15
735 °C	0.028	n	30
435 °C	3.1	n	0.8

8.4 Conclusions

Optical absorption and Hall Effect experiments on Ga_2SeTe_2 single crystals suggest that vacancy ordering in this material is not just a structural transformation, but one that can alter the electronic structure of the material. As vacancies order in Ga_2SeTe_2, the band gap decrease by ≈ 0.05 eV. The change in charge transport behavior was even more drastic, where sample resistivity decreased by two orders of magnitude for a vacancy ordered sample. While there certainly may be other effects at play for this change, the result can serve as a starting point for further investigations on the relationship between vacancy ordering and charge transport.

Chapter 9

Conclusion

In this dissertation, experimental investigations have been presented on the growth and characterization of the quasi-binary Ga_2Te_3-Ga_2Se_3 semiconductor alloy. Using a modified Bridgman method, large single crystals were grown that were suitable for various materials characterization techniques. Structural characterization of Ga_2SeTe_2 utilizing x-ray diffraction and electron microscopy revealed the presence of ordered two-dimensional vacancy structures in a global cubic crystal, as evidenced by the formation of satellite reflections in reciprocal space. Additionally, elongation of the Bragg peaks in reciprocal space allude to distortion of the cubic system. Diffraction under high temperatures and pressures revealed that vacancy ordering can alter the pressure-induced amoprhization behavior of Ga_2SeTe_2. More specifically, ordered and semi-ordered vacancy samples amorphized around 10-11 GPa in contrast to disordered vacancy samples, which amorphized at 8-9 GPa.

X-ray absorption fine structure experiments suggest that the distortions observed in the reciprocal space (seen in the Bragg peak elongation from single diffraction experiments) arise from cation-anion dumbbell contractions around the Ga, Se, and Te atoms in the cubic crystal. Aberration-corrected scanning transmission electron microscopy was employed to directly observe local atomic distortions in the Ga_2SeTe_2 structure. These were seen as atomic dumbbell inversions at the boundaries of the extended two-dimensional vacancy structures.

To examine the interplay between the intrinsic vacancies and material properties of Ga_2SeTe_2, positron annihilation spectroscopy, optical absorption, and Hall effect measurements were performed. Positron annihilation lifetimes in Ga_2SeTe_2 were similar to that of large open-volume defects. Positron trapping diminished as the stoichiometric vacancy structures become periodic. Band gap measurements via optical absorption demonstrated that vacancy ordering in Ga_2SeTe_2 redshifts its band gap by ≈ 0.05 eV. Results from Hall effect experiments showed analogous results, where the resistivity of vacancy ordered samples decreased by around two orders of magnitude accompanied by large gains in Hall mobility from around 1 cm^2/Vs to 30 cm^2/Vs.

9.1 Future Work

The Hall effect measurements discussed in Chapter 8 are of a very basic nature. A more detailed analysis would include variable temperature Hall effect experiments. Here, one may be able to measure the sample at liquid nitrogen temperatures to isolate effects characteristic of defects. Such measurements would prove useful in understanding whether the decreased resistivity observed for vacancy ordered Ga_2SeTe_2 is real or a consequence of variations in crystal quality. Moreover, the science of electric contacts on Ga_2SeTe_2 should be investigated to improve the reliability of charge transport measurements.

Recall in Chapter 1, that the motivation for studying the quasi-binary Ga_2Te_3-Ga_2Se_3 semiconductor alloy was related to finding new semiconductors for room-temperature gamma-ray detectors. The early observation of interesting structural effects in this material, however, resulted in an investigation primarily concerned with understanding the physics of vacancy

ordering. Nevertheless, single crystal specimens were sent to Brookhaven National Laboratory to measure their radiation response. This measurement involves fabricating a Ga_2SeTe_2 specimen in a planar geometry connected with electrodes. The setup is irradiated with α particles from the cathode side, and the electron mobility (μ_e) can be extracted by measuring the rise time of the observed pulses via an oscilloscope. The electron lifetime (τ_e) can then be calculated via the Hecht relation (see Chapter 1) to obtain the electron mobility lifetime product, $\mu_e\tau_e$, which is the figure of merit for a semiconductor's potential as a radiation detector material. The hole-mobility lifetime product may also be determined in an analogous manner where the fabricated Ga_2SeTe_2 device is irradiated from the anode side. Unfortunately, the Brookhaven group was not able to see any radiation response for the Ga_2SeTe_2 crystals as extreme difficulty was encountered in contact deposition. This illustrates that Ga_2SeTe_2-contact heterostructures can serve as a separate expansive project.

One must also note that there is a scarcity of information on the Ga_2Te_3-Ga_2Se_3 semiconductor alloy when it comes to its physical properties. Hence, any additional future work should include further analysis of properties that include: thermal conductivity for thermoelectric applications (which may be characterized with the aid of phonon dispersion curves); phase-change behavior–more specifically, charge transport and optical properties at high pressure to probe whether metal-to-insulator phase transition could occur at high pressures; Raman spectroscopy to investigate the additional vibrational modes introduced via vacancy ordering; deep-level transient spectroscopy to explore energy states created by defects within the Ga_2SeTe_2 band gap; neutron diffraction studies to investigate the effects of vacancy ordering on magnetic structure. This list is certainly not exhaustive, but it illustrates the possibility for new scientific discovery based on the rich reciprocal space observed in Ga_2SeTe_2 and its related compounds.

9.2 Final Remarks

The overarching theme in this dissertation is that the Ga_2Te_3-Ga_2Se_3 semiconductor alloy investigated here served as a model system to explore a variety of materials characterization techniques in an effort to probe new physical phenomena arising from structural transformations at the mesoscopic scale. Based on extensive x-ray scattering experiments and high-resolution electron microscopy, this was clearly demonstrated. However, the results are far from comprehensive and interest in chalcogenide alloys with native vacancies in the semiconductor device community is steadily increasing. As was the case with silicon one hundred years ago, however, extensive research on the fundamental structure and physical properties of this class of chalcogenide alloys is paramount in developing a further understanding of its technological potential.

Bibliography

[1] L Solymar and D Walsh. *Lectures on the Electrical Properties of Materials*. 5^{th} Edition. Oxford University Press, 1993.

[2] N Ashcroft and N Mermin. *Solid State Physics*. Brooks/Cole, 1976.

[3] C Kittel. *Introduction to Solid State Physics*. 8^{th} Edition. Wiley, 2005.

[4] J Singleton. *Band Theory and Electronic Properties of Solids*. Oxford University Press, 2010.

[5] W D Callister. *Materials Science and Engineering: An Introduction*. 7^{th} Edition. Wiley, 2008.

[6] R M Martin. *Electronic Structure*. Cambridge University Press, 2010.

[7] M D McCluskey and E Haller. *Dopants and Defects in Semiconductors*. CRC Press, 2012.

[8] G F Knoll. *Radiation Detection and Measurement*. 3^{rd} Edition. Wiley, 1999.

[9] G Lutz. *Semiconductor Radiation Detectors*. Springer, 2007.

[10] D S McGregor and H Hermon. "Room-temperature compound semiconductor radiation detectors". In: *Nuclear Instruments and Methods in Physics Research-Section A* 395.1 (1997), pp. 101–124.

[11] Z He. "Review of the Shockley–Ramo theorem and its application in semiconductor gamma-ray detectors". In: *Nuclear Inst. and Methods in Physics Research, A* 463.1-2 (2001), pp. 250–267.

[12] W Shockley. "Currents to conductors induced by a moving point charge". In: *Journal of Applied Physics* 9.10 (1938), p. 635.

[13] S Ramo. "Currents induced by electron motion". In: *Proceedings of the IRE* 27.9 (1939), pp. 584–585.

[14] K Hecht. "Zum Mechanismus des lichtelektrischen Primärstromes in isolierenden Kristallen". In: *Zeitschrift für Physik* 77.3-4 (1932), pp. 235–245.

[15] G F Knoll and D S McGregor. "Fundamentals of Semiconductor Detectors for Ionizing Radiation". In: *MRS Proceedings* 302 (1993), p. 3.

[16] A Owens and A Peacock. "Compound semiconductor radiation detectors". In: *Nuclear Inst. and Methods in Physics Research, A* 531.1-2 (2004), pp. 18–37.

[17] G A Armantrout et al. "What can be expected from high-Z semiconductor detectors?" In: *IEEE Transactions on Nuclear Science* 24.1 (1977), pp. 121–125.

[18] A E Bolotnikov et al. "Effects of Te inclusions on the performance of CdZnTe radiation detectors". In: *IEEE Transactions on Nuclear Science* 55.5 (2008), pp. 2757–2764.

[19] A E Bolotnikov et al. "Extended Defects in CdZnTe Radiation Detectors". In: *IEEE Transactions on Nuclear Science* 56.4 (2009), pp. 1775–1783.

[20] T Onodera, K Hitomi, and T Shoji. "Spectroscopic performance and long-term stability of thallium bromide radiation detectors". In: *Nuclear Instruments & Methods In Physics Research Section A* 568.1 (2006), pp. 433–436.

[21] K Hitomi et al. "Polarization Phenomena in TlBr Detectors". In: *IEEE Transactions on Nuclear Science* 56.4 (2009), pp. 1859–1862.

[22] A E Bolotnikov et al. "Te Inclusions in CZT Detectors: New Method for Correcting Their Adverse Effects". In: *IEEE Transactions on Nuclear Science* 57.2 (2010), pp. 910–919.

[23] K Hitomi, T Shoji, and Y Niizeki. "A method for suppressing polarization phenomena in TlBr detectors". In: *Nuclear Instruments & Methods In Physics Research Section A* 585.1 (2008), pp. 102–104.

[24] H Hahn and W Klingler. "Über die Kristallstrukturen von Ga_2S_3, Ga_2Se_3 und Ga_2Te_3". In: *Zeitschrift für anorganische Chemie* 259.1-4 (1949), pp. 135–142.

[25] H Hahn and W Klingler. "Über die Kristallstrukturen des In_2S_3 und In_2Te_3". In: *Zeitschrift für anorganische Chemie* 260.1-3 (1949), pp. 97–109.

[26] H Hahn. "Zur Struktur der Galliumchalkogenide". In: *Angewandte Chemie* 64.7 (1952), pp. 203–203.

[27] J C Woolley and B R Pamplin. "The ordered crystal structure of In_2Te_3". In: *Journal of the Less Common Metals* 1 (1959), pp. 362–376.

[28] D Lübbers and V Leute. "The crystal structure of β–Ga_2Se_3". In: *Journal of Solid State Chemistry* 43.3 (1982), pp. 339–345.

[29] PC Newman. "Superlattice Structure in Ga_2Te_3". In: *Nature* 200 (1963), p. 876.

[30] D P Singh et al. "Hexagonal (Superlattice) Form of Ga_2Te_3". In: *Journal of Materials Science* 25.5 (1990), pp. 2362–2366.

[31] Yo Otaki et al. "X-ray study of the modulated structure in quenched Ga_2Te_3 with a defect zinc-blende lattice". In: *Acta Materialia* 57.5 (Mar. 2009), pp. 1392–1398.

[32] Y Otaki et al. "X-ray study of the modulated structure in as-grown Ga_2Te_3 crystals with the defect zinc-blende lattice". In: *Journal of Solid State Chemistry* 182.6 (2009), pp. 1556–1562.

[33] S Kashida et al. "Single crystal X-ray study of the modulated structure in Ga_2XTe_3 with the defect zinc-blende structure". In: *physica status solidi c* 6.5 (2009), pp. 1162–1165.

[34] M Guymont, A Tomas, and M Guittard. "The structure of Ga_2Te_3 an x-ray and high-resolution electron microscopy study". In: *Philosophical Magazine A* 66.1 (1992), pp. 133–139.

[35] L Kienle et al. "Realstrukturen von Defektvarianten des Zinkblendetyps". In: *Zeitschrift für anorganische und allgemeine Chemie* 629.78 (2003), pp. 1412–1420.

[36] K Kurosaki, S Yamanaka, and M Ishimaru. "Unexpectedly low thermal conductivity in natural nanostructured bulk Ga_2Te_3". In: *Applied Physics Letters* 93.1 (2008).

[37] C-E Kim et al. "Effect of Vacancy Distribution on the Thermal Conductivity of Ga_2Te_3 and Ga_2Se_3". In: *Journal of Electronic Materials* 40.5 (2011), pp. 999–1004.

[38] D Bose and S De Purkayastha. "Dielectric and photoconducting properties of Ga_2Te_3 and In_2Te_3 crystals". In: *Materials Research Bulletin* (1981).

[39] S Sen and D N Bose. "Electrical and optical properties of single crystal In_2Te_3 and Ga_2Te_3". In: *Solid State Communications* 50.1 (1984), pp. 39–42.

[40] C Julien, I Ivanov, and C Ecrepont. "Optical and Electrical Properties of Ga_2Te_3 Crystals". In: *physica status solidi C* (1994).

[41] G Gamal and H Elshaikh. "Investigation of thermoelectric power of Ga_2Se_3 monocrystals". In: *Crystal Research and Technology* 30.6 (1995), pp. 867–872.

[42] A E Belal, A Elshaikh, and I A Ashraf. "Temperature dependence of electrical conductivity and Hall effect of Ga_2Se_3 single crystals". In: *Crystal Research and Technology* 30.1 (1995), pp. 135–139.

[43] J C Woolley and B Ray. "Effects of solid solution of Ga_2Te_3 with $A^{II}B^{VI}$ tellurides". In: *Journal of Physics and Chemistry of Solids* 16 (1960).

[44] A E Bekheet. "Electrical and optical properties of amorphous Ga_2Te_3 films". In: *European Journal of Applied Physics* 16 (2001), pp. 187–193.

[45] G A Gamal et al. "Ferroelectric phase transition in Ga_2Te_3 single crystals". In: *Journal of Physics and Chemistry of Solids* 66.1 (2005), pp. 1–4.

[46] K-H Park et al. "Optical properties of Ga_2Se_3: Co^{2+} single crystals". In: *Solid State Communications* 70.10 (1989), pp. 971–974.

[47] I H Mutlu, M Z Zarbaliyev, and F Aslan. "Preparation of Ga_2Se_3 thin films by sol-gel technique". In: *Journal Of Sol-Gel Science And Technology* 50.3 (2009), pp. 271–274.

[48] M Rusu et al. "Deposition and characterization of Ga_2Se_3 thin films prepared by a novel chemical close-spaced vapour transport technique". In: *Journal Of Physics-Condensed Matter* 15 (2003), p. 8185.

[49] T Okamoto et al. "Optical anisotropy of vacancy-ordered Ga_2Se_3 grown by molecular beam epitaxy". In: *Japanese Journal of Applied Physics* 31 (1992), pp. 143–144.

[50] T Okamoto et al. "Anomalous anisotropy in the absorption coefficient of vacancy-ordered Ga_2Se_3". In: *Journal of Electronic Materials* 22.2 (1993), pp. 229–232.

[51] T Okamoto et al. "Polarized photoluminescence in vacancy-ordered Ga_2Se_3". In: *Journal of Crystal Growth* 138.1-4 (1994), pp. 204–207.

[52] Hao Zhu et al. "Ga_2Te_3 phase change material for low-power phase change memory application". In: *Applied Physics Letters* 97.8 (2010), p. 083504.

[53] T Siegrist et al. "Disorder-induced localization in crystalline phase-change materials". In: *Nature Materials* 10.3 (Jan. 2011), pp. 202–208.

[54] W Zhang et al. "Role of vacancies in metal–insulator transitions of crystalline phase-change materials". In: *Nature Materials* 11.11 (2012), pp. 952–956.

[55] V M Koshkin and Y N Dmitriev. "Chemistry and Physics of Compounds with Loose Crystal Structure". In: *Chemistry Reviews* 19 (1994), pp. 1–138.

[56] V M Koshkin et al. "Unstable equilibrium and radiation defects in solids". In: *Solid State Communications* 13.1 (1973), pp. 1–4.

[57] V M Koshkin et al. "Radiation stability of $A^{III}{}_2B^{VI}{}_3$ semiconductors". In: *Radiation Effects* 29.1 (1976), pp. 1–6.

[58] Yu G Gurevich, V M Koshkin, and I N Volovichev. "The heterocontact of two intrinsic semiconductors and radiation-stable electronics". In: *Solid-State Electronics* 38.1 (1995), pp. 235–242.

[59] M Luo and M Wuttig. "The Dependence of Crystal Structure of Te Based Phase Change Materials on the Number of Valence Electrons". In: *Advanced Materials* 16.5 (2004), pp. 439–443.

[60] "Alloy Phase Diagrams". In: *ASM Handbook* 3 (1992).

[61] W W Warren. "Solid immiscibility and liquid structure in the $Ga_2(Se_xTe_{1-x})_3$ alloy system". In: *Journal of Physics and Chemistry of Solids* 35.9 (1974), pp. 1153–1157.

[62] M Kerkhoff and V Leute. "The phase diagram of the quasibinary system Ga_2Te_3/Ga_2Se_3". In: *Journal of Alloys and Compounds* 381.1-2 (2004), pp. 124–129.

[63] R A Laudise. *The Growth of Single Crystals*. Prentice-Hall, 1970.

[64] M C Flemings. *Solidification Processing*. McGraw-Hill, 1974.

[65] J C Brice. *Crystal Growth Processes*. Wiley, 1986.

[66] B D Cullity. *Elements of X-Ray Diffraction*. 2^{nd} Edition. Addison-Wesley, 1978.

[67] J Als-Nielsen and D McMorrow. *Elements of Modern X-ray Physics*. 2^{nd} Edition. Wiley, 2011.

[68] B Fultz and J M Howe. *Transmission Electron Microscopy and Diffractometry of Materials*. 3^{rd} Edition. Springer, 2008.

[69] A P Hammersley et al. "Two-dimensional detector software: From real detector to idealised image or two-theta scan". In: *High Pressure Research* 14.235 (1996).

[70] P L Lee et al. "A twelve-analyzer detector system for high-resolution powder diffraction". In: *Journal of Synchrotron Radiation* 15.5 (2008), pp. 427–432.

[71] *FullProf Suite*. URL: `https://www.ill.eu/sites/fullprof/index.html`.

[72] D B Sirdeshmukh, L Sirdeshmukh, and K G Subhadra. *Atomistic Properties of Solids*. Springer, 2011.

[73] E Karapetrova et al. "Design and performance of the 33-BM beamline at the Advanced Photon Source". In: *Nuclear Instruments and Methods in Physics Research A* 649.1 (2011), pp. 52–54.

[74] M Kunz et al. "A beamline for high-pressure studies at the Advanced Light Source with a superconducting bending magnet as the source". In: *Journal of Synchrotron Radiation* 12.5 (2005), pp. 650–658.

[75] URL: `http://www.earth.northwestern.edu/research/jacobsen/pics/DAC-principle.jpg`.

[76] M Wuttig et al. "The role of vacancies and local distortions in the design of new phase-change materials". In: *Nature Materials* 6.2 (2006), pp. 122–128.

[77] G Bunker. *Introduction to XAFS: A Practical Guide to X-ray Absorption Fine Structure Spectroscopy*. 2^{nd} Edition. Cambridge University Press, 2009.

[78] URL: `http://home.comcast.net/~sam_webb/sixpack.html`.

[79] D B Williams and C B Carter. *Transmission Electron Microscopy: A Textbook for Materials Science*. 2^{nd} Edition. Springer, 2009.

[80] J C H Spence. *High-Resolution Electron Microscopy*. 3^{rd} Edition. Oxford University Press, 2003.

[81] R Krause-Rehberg and H S Leipner. *Positron Annihilation in Semiconductors*. Springer, 1998.

[82] K Lynn et al. "Positron-annihilation momentum profiles in aluminum: core contribution and the independent-particle model". In: *Physical Review Letters* 38.5 (1977).

[83] H Saito et al. "A new positron lifetime spectrometer using a fast digital oscilloscope and BaF_2 scintillators". In: *Nuclear Inst. and Methods in Physics Research, A* 487.3 (2002), pp. 612–617.

[84] M Fox. *Optical Properties of Solids*. 2^{nd} Edition. Oxford University Press, 2010.

[85] L J van der Pauw. "A method of measuring specific resistivity and Hall effect of discs of arbitrary shape". In: *Philips Research Reports* 13.1 (1958), pp. 1–9.

[86] L J van der Pauw. "A method of measuring the resistivity and Hall coefficient on lamellae of arbitrary shape". In: *Philips Technical Review* 20.8 (1958), pp. 220–224.

[87] L J van der Pauw. "Determination of resistivity tensor and Hall tensor of anisotropic conductors". In: *Philips Research Reports* 16 (1961), pp. 187–195.